2012

Numerical Studies Of Orographic Effects On Tropical Weather Systems

Yi-Chih Huang
North Carolina Agricultural and Technical State University

Numerical Studies of Orographic Effects on Tropical Weather Systems

Yi-Chih Huang

North Carolina A&T State University

A dissertation submitted to the graduate faculty

in partial fulfillment of the requirements for the degree of

DOCTOR OF PHILOSOPHY

Department: Energy and Environmental Systems

Major: Atmospheric Sciences

Major Professor: Dr. Yuh-Lang Lin

2012

School of Graduate Studies
North Carolina Agricultural and Technical State University

This is to certify the Doctoral Dissertation of

Yi-Chih Huang

has met the dissertation requirements of
North Carolina Agricultural and technical State University

Greensboro, North Carolina
2012

Approved by:

Yuh-Lang Lin, Ph.D.
Major Professor, Committee Chair

Jing Zhang, Ph.D.
Committee member

Ademe Mekonnen, Ph.D.
Committee Member

Liping Liu, Ph.D.
Committee Member

Bo-Wen Shen, Ph.D.
Committee Member

Keith A, Schimmel, PhD.
Department Chairperson

Sanjiv Sarin, Ph.D.
Associate Vice Chancellor for Research and
Dean of Graduate Studies

Biographical Sketch

Yi-Chih Huang was born on July 29, 1964, in Kaohsiung, Taiwan. He received the Bachelor of Science degree in Atmospheric Sciences from National Central University in 1993, a Master of Science degree in Atmospheric Physics from National Central University in 1995, and a Master of Science degree in Atmospheric Sciences from University of California, Los Angeles in 2005. He is a candidate for the Ph.D. in Energy and Environmental Systems with a concentration in Atmospheric Sciences.

Acknowledgments

There are several people who without their help this dissertation would not be possible. While I cannot mention all of the people who have influenced and assisted me throughout this process I hope they are all aware of their contributions and my gratitude. There are however, a few people who I would like to formally thank. Firstly, I would like to express my gratitude to my advisor and mentor, Dr. Yuh-Lang Lin, for his advice, support, help, and allowing me to explore my interest with this project. He has been a source of optimism whenever I have been doubtful. Secondly, I would like to thank Dr. Keith Schimmel for the financial support from the Department of Energy & Environmental Systems, and Dr. Solomon Bililign for his support in participating in NOAA ISET Center research activities which provide opportunities for interacting with NOAA scientists and other ISET students. Thirdly, my PhD Dissertation Committee members, Drs. Jing Zhang, Ademe Mekonnen, and Liping Liu, have provide valuable comments on the draft of the dissertation, which have greatly improved the quality of the dissertation. Furthermore, I would like to thank my family and friends for their support during this period.

Table of Contents

List of Figures

List of Tables

List of Symbols and Nomenclature

a	zonal half width
b	meridional half width
c_s	propagation speed of the convective system
f	Coriolis parameter ($= 2\,\Omega \sin\varphi,\ \varphi$ is latitude).
g	gravitational acceleration
h	mountain height function
h_0	maximum mountain height
k	zonal wave number
m	vertical wave number
$\hat{t}$	nondimensional time ($=Ut/a$)
x	eastward distance
y	northward distance
z	upward distance
C_{gx}	zonal group velocity
C_{gz}	vertical group velocity
E	precipitation efficiency
L	the dimension of the terrain
L_s	horizontal scale of a convective system
N	Brunt-Vaisala frequency
P	total precipitation
Q	specific humidity
Ri	Richardson number

Ro	Rossby number
U	basic wind speed
U_z	vertical wind shear of the basic wind
V_H	horizontal wind velocity
w	vertical velocity
w_{env}	environmentally induced vertical velocity
w_{oro}	orographically induced vertical velocity
β	the variation of the Coriolis parameter with latitude ($\equiv \frac{df}{dy}$)
$\hat{\beta}$	non-dimensional β ($\equiv \beta L^2/U$)
θ	potential temperature
θ_e	equivalent potential temperature
θ_e^*	saturated equivalent potential temperature
ω	angular frequency
AEJ	African easterly jet
AEW	African easterly wave
AMSU	Advanced Microwave Sounding Units
ARW	Advanced Research Weather and Research Forecast (WRF) model
CAPE	convective available potential energy
CWB	Central Weather Bureau of Taiwan
EH	Ethiopian Highland
Fr	Froude number
GFDM	Geophysical fluid dynamic model
ITCZ	Intertropical Convergence Zone

JMA	Japan Meteorological Agency
JTWC	Joint Typhoon Warning Center
LST	local standard time
MCS	mesoscale convective system
NCEP	National Centers for Environmental Prediction
NOAA	National Oceanic and Atmospheric Administration
Ri	Richardson numbers
Ro	Rossby numbers
SSM/I	Special Sensor Microwave Imagers
SST	sea surface temperature
UTC	Coordinated Universal Time
WAM	West African monsoon
WRF	Weather Research and Forecasting model

Abstract

With Geophysical Fluid Dynamic Model and Weather Research and Forecasting model, two tropical weather systems, African easterly wave (AEW) and Typhoon Morakot (2009), are studied, respectively. With regards to AEW, wave-like disturbances were generated on the lee side by vortex shedding for an easterly flow over an idealized mountain, with a wavelength of about 2000 km, a period of ~2-3 days, and a propagating speed of ~9.6 ms^{-1} which mimic an AEW. Thus an AEW may be generated by vortex shedding. Furthermore, these orographically generated hydrostatic, continuously stratified inertia-gravity waves on a β-plane are characterized as mixed Rossby-gravity waves based on the dispersion relationship. The dispersion relationship gives a phase speed of about 10 ms^{-1}, which is comparable to numerically simulated 9.6 ms^{-1} and the observed 8 ms^{-1}. Hence, the AEW-like disturbances are associated with orographically forced Rossby waves. As for Morakot, I found that in the ocean stage the upper outflow of the secondary circulation is not very clear. The eye disappears within two hours after landfall. The deep convection, secondary circulation and tilting maximum wind speeds disappear, and the eye wall corrupts within five hours after landfall. The wind speed, convergence, upward motion, and relative humidity close to the Morakot center are limited when it crossed northern Taiwan; whereas large wind speed, convergence, upward motion, and humid regions are away from the Morakot center to the south with heavy rainfall because of the interactions between Morakot circulation, the high and steep Central Mountain Range, and the prevailing southwesterly wind. In the comparison with five typhoons in recent years causing large accumulated rainfall in Taiwan, the abundant water vapor around Taiwan outweighs translation speed and orographic lifting in leading to the record-breaking precipitation.

CHAPTER 1

Introduction

Topography has strong impacts on atmospheric flow and weather systems. In fact, topography may also induce important weather systems, in addition to the modification of approaching atmospheric flow and systems. Many factors with various scales have interactive effects on the issues of atmospheric sciences. Data analysis could only reveal limited information. Numerical model is a powerful tool to conduct experiments on computers in order to understand the cause-effect relation of weather phenomena. This study investigates the orographic effects on tropical weather systems by numerical modeling. The topics in this study are idealized simulation of orographically generated African easterly waves (AEWs) and orographic effects on Typhoon Morakot (2009) (Morakot thereafter). The common specialties in these two cases are the blocking of mountains, nonlinearity, and westward movement. Because of the blocking of Ethiopian Highland, there are lee vorticity, meander streamlines, and negative pressure perturbations generated. Because of the blocking of Central Mountain Range, typhoon Morakot (2009) moved slowly when approaching Taiwan, then one low pressure generated at the lee side of Central Mountain Range. Also, weather systems move westward which is common in these two subjects. As for nonlinearity, in the control case of idealized simulation, Fr=0.29 indicates nonlinearity is not neglected. Central Mountain Range is so steep that nonlinearity is important.

AEWs are closely associated with the development and movement of weather systems and precipitation in Africa and the Atlantic Ocean. There are many mesoscale convective systems (MCSs) propagating with and through AEWs, with periods in which convection strengthens and vice versa (Payne and McGarry, 1977). Thus, the precipitation in the boreal tropical Africa is regulated by AEWs. On the other hand, it has been proposed that an AEW

system, along with African easterly jet (AEJ), is a critically consequential component of West African monsoon (WAM) rainfall variability (Redelsperger et al., 2002). Also, many studies have demonstrated positive correlation between AEWs and Atlantic tropical cyclones. Many tropical cyclones originated over eastern Atlantic Ocean in low latitudes were triggered by AEWs. (e.g., Piersig 1936; Riehl 1945; Gray 1968; Carlson 1969). AEWs are crucial to the weather systems and precipitation in Africa and the Atlantic Ocean. Although many studies have been given much attention to AEWs, the formation of AEWs is still not well-understood and thus deserves further study.

In spite of the important research about flow over large-scale mountains and its associated wave disturbances on the lee sides, the impacts of the Earth rotational effects and β effects on lee vortices have not been studied thoroughly. In addition, the relationship of these lee vortices to the AEW is not clear. Hence, there is a need to conduct systematic research to understand the basic dynamics of the Earth rotational effects and β effects on the lee vortex. In this study we chose to explore EH because it could serve as the source of African easterly waves, which are crucial to the weather systems and precipitation in Africa and the Atlantic Ocean. Ethiopian Highlands (EH) has a dimension of about 600 km $\times$1200 km with a mean height of 2000 m as shown in Figure 3.1. In this study, we plan to adopt a simple model, the Geophysical Fluid dynamic Model (GFDM) (Lin et al., 1999), to systematically study the effects of the Earth rotational effects, β effects, uniform zonal wind, vertical wind shear, and the geometry of EH on the waves generated by flow over an idealized EH and its implication to the generation of AEWs.

This study about orographically generated AEWs is organized as follows. In Section 3.2, the numerical model GFDM, numerical experiment design, both dimensional and nondimensional flows, and orographic parameters will be described. The results of idealized

simulations will be discussed in Section 3.3. The basic dynamics are discussed based on a series of systematic numerical experiments. A summary can be found in Section 3.4.

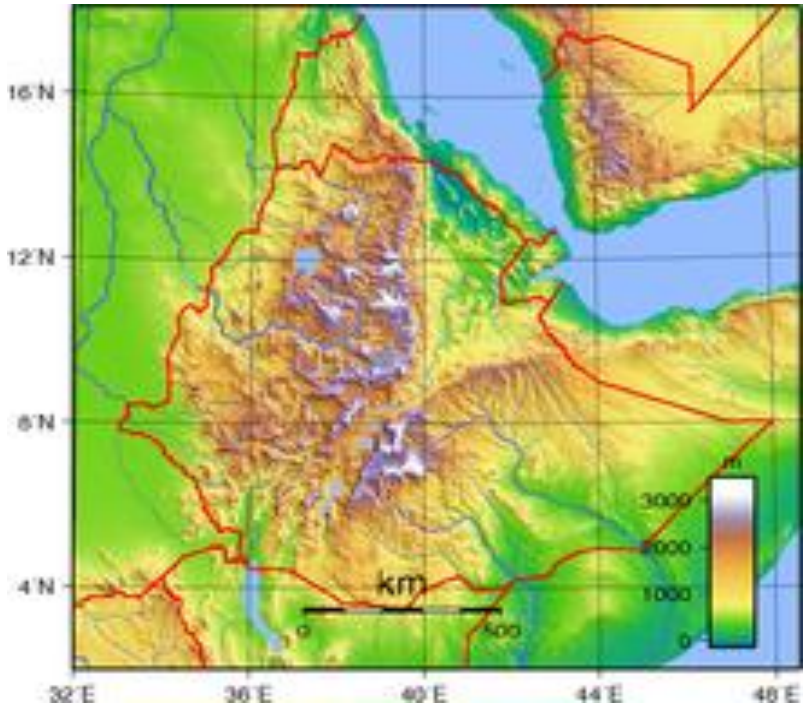

Figure 1.1. Topography of Ethiopian Highland

With respect to Typhoon Morakot (2009), the rainfall associated with the passage of typhoons is one of the major sources of precipitation in Taiwan. Morakot (2009) appeared as a tropical depression on August 3 2009. Then, it moved westward and made landfall in Taiwan on 7 August 2009. Typhoon Morakot (2009) is only category 1 intensity on the Saffir–Simpson hurricane scale (Simpson 1974) before it made landfall, but the rainfall of more than 1500 mm on 8 August in UTC connected to Morakot is astonishing. Morakot resulted in disasters such as landslide, mudslide, harsh flood, etc. and many casualties in the calamity. In the study, we would like to investigate the causes of extremely rainfall occurred during the passage of Typhoon Morakot (2009) over Taiwan's Central Mountain Range (CMR), in particular the three-dimensional structure, the factors resulting in the extremely heavy precipitation, and the

sensitivity of terrain to precipitation by conducting numerical experiments, as to be described below.

Generally there is heavy rainfall close to the typhoon center when a typhoon passes by. But there was limited precipitation close to the typhoon center as Morakot passed by. Originally the convective activity close to Morakot center develops well. The major precipitation regions are to the south of Morakot. The asymmetric rainfall patterns could be associated with the change of the three-dimensional structure of Morakot. Although there are a number of studies already done on Morakot, the time evolution of 3D structure, the asymmetric precipitation patterns, the major factors responsible for the extremely heavy precipitation, and the exact impacts of Taiwan topography on the extremely heavy rainfall under dominating large-scale circulations are still not clear. Thus, there is a need to conduct systematic approach to understand the interaction of Morakot outer circulation and its synoptic environment, the rainfall patterns in the vicinity of CMR, and the basic dynamics of the orographic effects on the extremely heavy rainfall. Numerical simulation is a good tool in revealing the detail of a typhoon. Because the intensity of Morakot is only category 1 on the Saffir–Simpson hurricane scale, it is difficult to obtain a good simulation even only in terms of the asymmetric rainfall patterns caused by Morakot. Wu et al. (2010) indicate the challenge of numerical study for Morakot such as the translation speed, underestimated water vapor, and so forth. In this study, we employ the Advanced Research WRF (Weather Research and Forecasting) model (ARW) Model (Skamarock et al. 2008) to examine the 3D structure of Morakot, precipitation patterns, and the effects of the terrain on precipitation. Additionally, the study applies storm relative 16 km microwave-based total precipitable water imagery to the analysis of water vapor.

This study about Morakot is organized as follows. In Section 4.2, the numerical model WRF, experiment design, radar reflectivity data, the total precipitable water data and best track data will be described. The results of simulations will be verified in Section 4.3. The analysis on time evolution of the 3D structure is conducted in Section 4. The analysis of factors, including upward motion, water vapor and slow translation speed, causing huge precipitation, will be given in Section 4.5. The basic dynamics revealed by the experiments are discussed based on the change of terrain and the presence of land in Section 4.6. A summary can be found in Section 4.7.

CHAPTER 2

Literature Review

With respects to AEWs, several mechanisms have been proposed in previous studies to explain the generation of AEWs. For instance, mixed barotropic-baroclinic instability (Burpee 1972), baroclinic instability connected to Saharan surface heating (Chang 1993), instability of AEJ (Simmons 1977; Thorncroft and Hoskins 1994a; Thorncroft and Hoskins 1994b), latent heat release of cumulus convection within the Intertropical Convergence Zone (ITCZ) (Berry and Thorncroft 2005; Mekonnen et al. 2006), and orographic generating or modifying by central or eastern African mountains (Zenhder 1996; Lin et al. 2005; Lin 2009; Lin 2012).

Concerning the lee vortex, for three-dimensional, nonlinear, stratified viscous flow over a symmetric terrain, the creation of two vortices with opposite signs near the surface at the lee side of an obstacle was ascribed to boundary layer friction (Batchelor 1967; Hunt and Snyder 1980). However, lee vortices could form in an inviscid, non-rotating fluid. There are two major ways to interpret vortex shedding in the absence of friction, tilting of baroclinically-generated vorticity (Smolarkiewicz and Rotunno 1989) and generation of internal potential vorticity (Smith 1989). It appears that the baroclinically-generated vorticity mechanism dominated in the early stage, while the generation of internal potential vorticity dominated in later stage of the vortex generation processes (e.g., see review in Lin 2007). In the study of large-scale terrain with the dimension of 1000 km, Coriolis effects cannot be ignored. Due to small Coriolis force in low latitudes, the above study cannot be applied to flow over large-scale mountains, such as the Ethiopian highlands (see Figure 1.1).

With regard to flow over a large-scale mountain, the conservation of potential vorticity is an important concept. Charney and Eliassen (1949) demonstrated that mid-latitude westerly

flows over topography may generate large-scale quasi-stationary disturbances by forced accent. Bolin (1950) extended the discussion and emphasized the importance of large mountains in producing planetary waves in upper flows over the northern hemisphere. Employing a general circulation model, Manabe and Terpstra (1974) showed that there was a stationary trough at the lee side of large mountain ranges. Mountains noticeably increased the kinetic energy of stationary disturbances in the troposphere and decreased the kinetic energy of transient disturbances. Janowitz (1975) studied the impact of a low mountain on a stratified westerly on a β-plane. A general solution was achieved to a linear, stratified uniform flow over an arbitrary mountain. Rooney and Janowitz (1979) investigated the impacts of vertical shear on steady westerly, compressible, stratified fluid over a shallow mountain on a β-plane. The vertical shear increased the wavelength and reduced the deflections connected with lee Rossby waves induced by mountains. Using linearized shallow-water equations on a sphere, Grose and Hoskins (1979) probed the steady response to simple isolated mountains.

For a jet stream hitting at different angles on a mountain resulting in different Rossby wavetrain patterns, Hsu (1987) displayed sea-level pressure patterns and 500 mb height patterns associated with low- and high-frequency fluctuations to see the effects of mountains on large-scale low-level atmospheric circulations. Most of the patterns are topographic Rossby waves; but some characteristics of Kelvin waves were also found to the north of the Tibetan Plateau. Doyle and Shapiro (1999) explored the dynamics of low-level jet streams downstream of large-scale topography such as Greenland. The conservation of the Bernoulli function regulated the jet stream dynamics when air moved downward following the descent orography. The jet strength was very susceptible to the changes in non-dimensional mountain height and Rossby number. Teixeira and Grisogono (2008) investigated the influence of the β effect on Rossby-gravity wave

drag on elliptical mountains in linear, constant wind, static stability on a β-plane. The drag strongly increases compared with where the Coriolis parameter is constant, especially at high latitudes for meridionally oriented mountains.

With regards to Morakot (2009), the common ingredients leading to extremely heavy rainfall related to orography have been pointed out like high precipitation efficiency, a low level jet, steep orography, favorable mountain geography and a confluent flow, strong synoptically forced upward vertical motion, a moist unstable low-level flow, a high moisture flow upstream, a large, preexisting convective system, and slow movement of the convective system (Lin 2007). In the case of Morakot several ingredients have been proposed resulting in extremely heavy precipitation such as the monsoonal influence on precipitation patterns, terrain lifting effects, slow moving of Morakot, and moisture supply corresponding to monsoon surges (Hong et al. 2010; Chien and Kuo 2011; Wu et al. 2011). In terms of water vapor, it is suggested that abundant water vapor was supplied by southwesterly inserted in multiple large-scale circulation (Hong et al. 2010) and strengthened by monsoon gyre (Ge et al. 2010). In addition, extra water vapor transporting from Typhoon Goni (2009) could be significant (Xu et al. 2011). With regards to the slow translation after Morakot made the landfall, it is proposed that the coalescence of Morakot first with the quasi-biweekly oscillation and then with Madden-Julian oscillation intensified large-scale southwesterly, resulting in turning the track northward and moving very slowly, and thus having extremely heavy rainfall in southern Taiwan (Wu et al. 2011). Also, it is shown that the strong northerly wind between Morakot and the anticyclone decrease the northward steering flow associated with low-frequency oscillation (Liang et al. 2011). The maximum accumulated precipitation is reduced dramatically in the simulation with nearly-doubled translation speed based on EnKF data assimilation although the rainfall patterns

in the control run of (Yen et al. 2011) are different from those in observation. In a composite study of 19 tropical storms, it is demonstrated that the rainfall associated with the passage of a typhoon was proportional to the reciprocal of the translation speed (Chien and Kuo, 2011) which is consistent with the expression of precipitation in Doswell et al. (1996), Lin et al. (2001), and Lin (2007). Furthermore, convergence and orographic lifting are emphasized in the mesoscale processes leading to the extremely heavy precipitation (Lin et al. 2011).

Originally the convective activity close to Morakot center develops well. The asymmetric rainfall patterns in Taiwan could be associated with the change of the three-dimensional structure of Morakot after landfall. Some studies demonstrate the impacts of land or orography on the development of a tropical cyclone. The orographically induced decrease of latent and kinetic energy causes a tropical cyclone filled quickly (Bender et al. 1985). Principally the reduction of evaporation is responsible for tropical disturbance failing to develop on land (Tuleya 1994). Asymmetric structure could stem from quasi-discontinuity of surface heating and latent heat in idealized simulations (Chen and Yau 2003). Orographic influence could lead to decoupling between Doppler velocities and reflectivity (Lee et al. 2000). The asymmetric orographic forcing leads to the asymmetric precipitation patterns of Nari (2001) after landfall (Yang et al. 2011). But, in the case of Morakot, the asymmetric pattern exists before it made landfall due to the convergence of Morakot circulation and the prevailing southwesterly.

CHAPTER 3

Idealized Simulations of Orographically Generated African Easterly Waves

3.1. Statement of the Problem and Significance

African easterly waves (AEWs) are closely associated with the development and movement of weather systems and precipitation in Africa and the Atlantic Ocean. There are many mesoscale convective systems (MCSs) propagating with and through AEWs, with periods in which convection strengthens and vice versa (Payne and McGarry, 1977). Thus, the precipitation in the boreal tropical Africa is regulated by AEWs. On the other hand, it has been proposed that an AEW system, along with African easterly jet (AEJ), is a critically consequential component of West African monsoon (WAM) rainfall variability (Redelsperger et al., 2002). Also, many studies have demonstrated positive correlation between AEWs and Atlantic tropical cyclones. Many tropical cyclones originated over eastern Atlantic Ocean in low latitudes were triggered by AEWs. (e.g., Piersig 1936; Riehl 1945; Gray 1968; Carlson 1969). AEWs are crucial to the weather systems and precipitation in Africa and over the Atlantic Ocean. Although many studies have given much attention to AEWs, the formation of AEWs is still not well-understood and thus deserves a further study.

3.2. Numerical Experiment Design for Idealized Flow over an Idealized Mountain

3.2.1. The Numerical Model. The numerical model GFDM used in this study is the model described in Lin et al. (1999) which is based on three-dimensional, primitive equations for a dry, stratified, hydrostatic, Boussinesq fluid. The equations of the models are on the terrain-following coordinate (Gal-Chen and Somerville, 1975).

The boundary layer friction is able to generate lee vortices near the surface as shown in Batchelor (1967) and Hunt and Snyder (1980). In the study, we are going to investigate the

impacts of Earth rotation and β effects on the generation of lee vortices. Therefore, the free-slip lower boundary condition and β-plane are applied to the model.

The characteristics of GFDM are as follows:

The atmospheric variables are arranged on an Arakawa C staggered grid.

- The third-order Adams-Bashforth scheme is used in time integration.
- The horizontal and vertical advection schemes are fourth-order and second-order centered different schemes, respectively.
- The lower boundary condition is free-slip.
- The upper-boundary condition is a radiation boundary condition (Klemp and Durran, 1983).
- Orlanski (1976) radiation condition is used as the lateral boundary condition.
- Subtracting off the horizontal average of pressure reduces truncation error due to topographic terms and diminishes the unrealistic pressure perturbation (Clark, 1977).
- A five-point numerical smoothing is employed in both horizontal and vertical directions (Shapiro, 1970).

The initial condition of potential temperature in GFDM depends on the conditions in discussion. In the condition of constant Brunt-Vaisala frequency (N) and uniform zonal wind velocity (U), the potential temperature θ is given based on the definition of N as $N^2 = \frac{g}{\bar{\theta}}\frac{\partial \bar{\theta}}{\partial z}$, where $\bar{\theta}$ is given as 273 K at the lowest level. Under constant Brunt-Vaisala frequency and linear vertical zonal wind shear, the potential temperature is given by the thermal wind balance $U_z = -\frac{g}{f\theta}\frac{\partial \bar{\theta}}{\partial y}$.

3.2.2. Flow and Orographic Control Parameters. In order to investigate the impacts of f-plane, β-plane, uniform wind (U), linear vertical wind shear (U_z), zonal half-width (a),

meridional half-width (b), and mountain height (h_0) on flow over a meso-α scale mountain, such as the Ethiopian Highlands, it is important to identify the relevant control parameters (see Tables 3.1 and 3.2). Based on the governing equations of the flow of interest, there are eight potential parameters: U, U_z, f, β, N, h_0, a, and b among which there are only two dimensional units. According to the Buckingham-π theorem, the governing equations are equivalent to the equations including six nondimensional parameters formed from the above six parameters. The six nondimensional parameters may be chosen to be Rossby number ($Ro=U/fL$, $L=4a$), Froude number ($Fr = U/Nh_0$), steepness of topography (h_0/a), mountain width-length aspect ratio (b/a), nondimensional $\hat{\beta}$ ($\beta L^2/U$), and Richardson number ($Ri = N^2/U_z^2$). For instance, whether the same nondimensional parameters such as Rossby number and/or Froude number, etc. would guarantee the same response in wave generation, will be discussed in the numerical experiments of sensitivity tests. Due to the large number of nondimensional control parameters, it would be unrealistic to make a thorough investigation of all these independent control parameters. Instead, we will make a series of experiments based on a limited subset of the dimensional control parameters. However, the nondimensional control parameters will be used to facilitate the discussion and to help the understanding of the basic dynamics.

3.2.3. Numerical Experiment Design. The numerical experiment design includes the control run and several sensitivity tests. The control run is designed for a uniform easterly flow (U = -10 ms^{-1}) with constant buoyancy frequency (N = 0.01 s^{-1}) over a bell-shaped topography of mountain height (h_0) 3500 m, zonal half-width (a) 150 km, and meridional half-width (b) 300 km on a β-plane ($\beta = 2.254\times10^{-11}$ $m^{-1}s^{-1}$) centered at 10°N.

$$h(x,y) = \frac{h_0}{\left[\left(\frac{x}{a}\right)^2 + \left(\frac{y}{b}\right)^2 + 1\right]^{3/2}}$$

The sensitivity tests are to investigate the effects of Coriolis parameter (f_0), planetary vorticity gradient (β), basic wind speed (U), vertical wind shear (U_z), nonlinearity (Fr), mountain steepness (h_0/a), and mountain width-length aspect ratio (b/a). The changes in the Coriolis parameter include the conditions of β-plane, f-plane and without Coriolis force. The β is carried out by varying the center latitude of the mountain to 0°N, 10°N, 20°N, and 30°N with the associated Rossby numbers (Ro) equal to ∞, 0.66, 0.33, and 0.23, respectively. The uniform easterly wind velocities comprise -20 ms^{-1} (Ro=1.3, Fr=0.57, $\hat{\beta}$=0.40), -10 ms^{-1} (Ro=0.66, Fr=0.29, $\hat{\beta}$=0.81), and -5 ms^{-1} (Ro=0.33, Fr=0.14, $\hat{\beta}$=1.6). The significance of inertial force, Coriolis force, flow nonlinearity, and β effects under uniform easterly flow will be discussed. In the sensitivity tests of vertical wind shear, nonlinearity, mountain steepness, and mountain width-length aspect ratio, only one nondimensional parameter is changed. The effects of vertical wind shear, nonlinearity, mountain steepness, and mountain width-length aspect ratio are measured by Richardson number, Froude number, h_0/a, and b/a, respectively. The nondimensional and dimensional parameters in the control case and sensitivity tests are listed in the Tables 3.1 and 3.2.

Table 3.1

Nondimensional control parameters

Cases	**Conditions**	***Ro***	***Fr***	$\hat{\beta}$	h_0/a	***b/a***	***Ri***
A*	control case	0.66	0.29	0.81	0.023	2	∞
B1	f-plane	0.66	0.29	0	0.023	2	∞
B2	no Coriolis force	∞	0.29	0	0.023	2	∞
C1	0°N	∞	0.29	0.82	0.023	2	∞
C2*	10°N	0.66	0.29	0.81	0.023	2	∞
C3	20°N	0.33	0.29	0.77	0.023	2	∞
C4	30°N	0.23	0.29	0.73	0.023	2	∞

Table 3.1 (cont.)

Cases	Conditions	*Ro*	*Fr*	$\hat{\beta}$	h_0/a	*b/a*	*Ri*
D1	U= -20 ms^{-1}	1.3	0.57	0.4	0.023	2	∞
D2*	U= -10 ms^{-1}	0.66	0.29	0.81	0.023	2	∞
D3	U= -5 ms^{-1}	0.33	0.14	1.6	0.023	2	∞
E1*	U_z= 0 s^{-1}	0.66	0.29	0.81	0.023	2	∞
E2	U_z= - 0.5×10^{-3} s^{-1}	0.66	0.29	0.81	0.023	2	400
E3	U_z= -1×10^{-3} s^{-1}	0.66	0.29	0.81	0.023	2	100
E4	U_z= -2×10^{-3} s^{-1}	0.66	0.29	0.81	0.023	2	25
F1	h_0=7000 m, a=300 km, b=600 km	0.33	0.14	3.2	0.023	2	∞
F2*	h_0=3500 m, a=150 km, b=300 km	0.66	0.29	0.81	0.023	2	∞
F3	h_0=1750 m, a=75 km, b=150 km	1.3	0.57	0.2	0.023	2	∞
G1	h_0=7000 m	0.66	0.14	0.81	0.047	2	∞
G2*	h_0=3500 m	0.66	0.29	0.81	0.023	2	∞
G3	h_0=1750 m	0.66	0.57	0.81	0.017	2	∞
H1	b=600 km	0.66	0.29	0.81	0.023	4	∞
H2*	b=300 km	0.66	0.29	0.81	0.023	2	∞
H3	b=150 km	0.66	0.29	0.81	0.023	1	∞
H4	b=75 km	0.66	0.29	0.81	0.023	0.5	∞

* (1) Dimensional parameters for the control case: on β-plane centered at 10°N, U= -10 ms^{-1}, U_z= 0 s^{-1}, h_0=3500 m, a=150 km, b=300 km.; (2) Cases with * are the same as the control case A*.

Table 3.2

Dimensional control parameters

Cases	U (ms^{-1})	f (s^{-1})	β (m^{-1} s^{-1})	h_0 (m)	a (km)	b (km)	U_z (s^{-1})	N (s^{-1})
A*	-10	2.532×10^{-5}	2.254×10^{-5}	3500	150	300	∞	0.01
B1	-10	2.532×10^{-5}	0	3500	150	300	∞	0.01
B2	-10	0	0	3500	150	300	∞	0.01
C1	-10	0	2.289×10^{-5}	3500	150	300	∞	0.01
C2*	-10	2.532×10^{-5}	2.254×10^{-5}	3500	150	300	∞	0.01
C3	-10	4.988×10^{-5}	2.151×10^{-5}	3500	150	300	∞	0.01
C4	-10	7.292×10^{-5}	2.028×10^{-5}	3500	150	300	∞	0.01

Table 3.2 (cont.)

Cases	U (ms^{-1})	f (s^{-1})	β ($m^{-1}\ s^{-1}$)	h_0 (m)	a (km)	b (km)	U_z (s^{-1})	N (s^{-1})
D1	-20	2.532×10^{-5}	2.254×10^{-5}	3500	150	300	∞	0.01
D2*	-10	2.532×10^{-5}	2.254×10^{-5}	3500	150	300	∞	0.01
D3	-5	2.532×10^{-5}	2.254×10^{-5}	3500	150	300	∞	0.01
E1*	-10	2.532×10^{-5}	2.254×10^{-5}	3500	150	300	0	0.01
E2	-10	2.532×10^{-5}	2.254×10^{-5}	3500	150	300	-0.5×10^{-3}	0.01
E3	-10	2.532×10^{-5}	2.254×10^{-5}	3500	150	300	-1×10^{-3}	0.01
E4	-10	2.532×10^{-5}	2.254×10^{-5}	3500	150	300	-2×10^{-3}	0.01
F1	-10	2.532×10^{-5}	2.254×10^{-5}	7000	300	600	∞	0.01
F2*	-10	2.532×10^{-5}	2.254×10^{-5}	3500	150	300	∞	0.01
F3	-10	2.532×10^{-5}	2.254×10^{-5}	1750	75	150	∞	0.01
G1	-10	2.532×10^{-5}	2.254×10^{-5}	7000	150	300	∞	0.01
G2*	-10	2.532×10^{-5}	2.254×10^{-5}	3500	150	300	∞	0.01
G3	-10	2.532×10^{-5}	2.254×10^{-5}	1750	150	300	∞	0.01
H1	-10	2.532×10^{-5}	2.254×10^{-5}	3500	150	600	∞	0.01
H2*	-10	2.532×10^{-5}	2.254×10^{-5}	3500	150	300	∞	0.01
H3	-10	2.532×10^{-5}	2.254×10^{-5}	3500	150	150	∞	0.01
H4	-10	2.532×10^{-5}	2.254×10^{-5}	3500	150	75	∞	0.01

* the same as the control case A*

3.3. Results

3.3.1. The Control Case. The control case is performed under a situation of uniform, stratified, easterly basic flow with U = -10 ms^{-1}, Brunt-Vaisala frequency (N) 0.01 s^{-1}, on a β-plane centered at 10°N over a bell-shaped mountain with h_0 = 3500 m, a = 150 km, and b = 300 km. The associated Rossby number (Ro = 0.66) and Froude number (Fr = 0.29) indicate that Earth rotational effects cannot be ignored and nonlinearity are essential, respectively. Figure 3.1 demonstrates the evolution of relative vorticity field and streamlines every day. The corresponding nondimensional time $\hat{t}$ (Ut/a) is 5.76 (1 day).

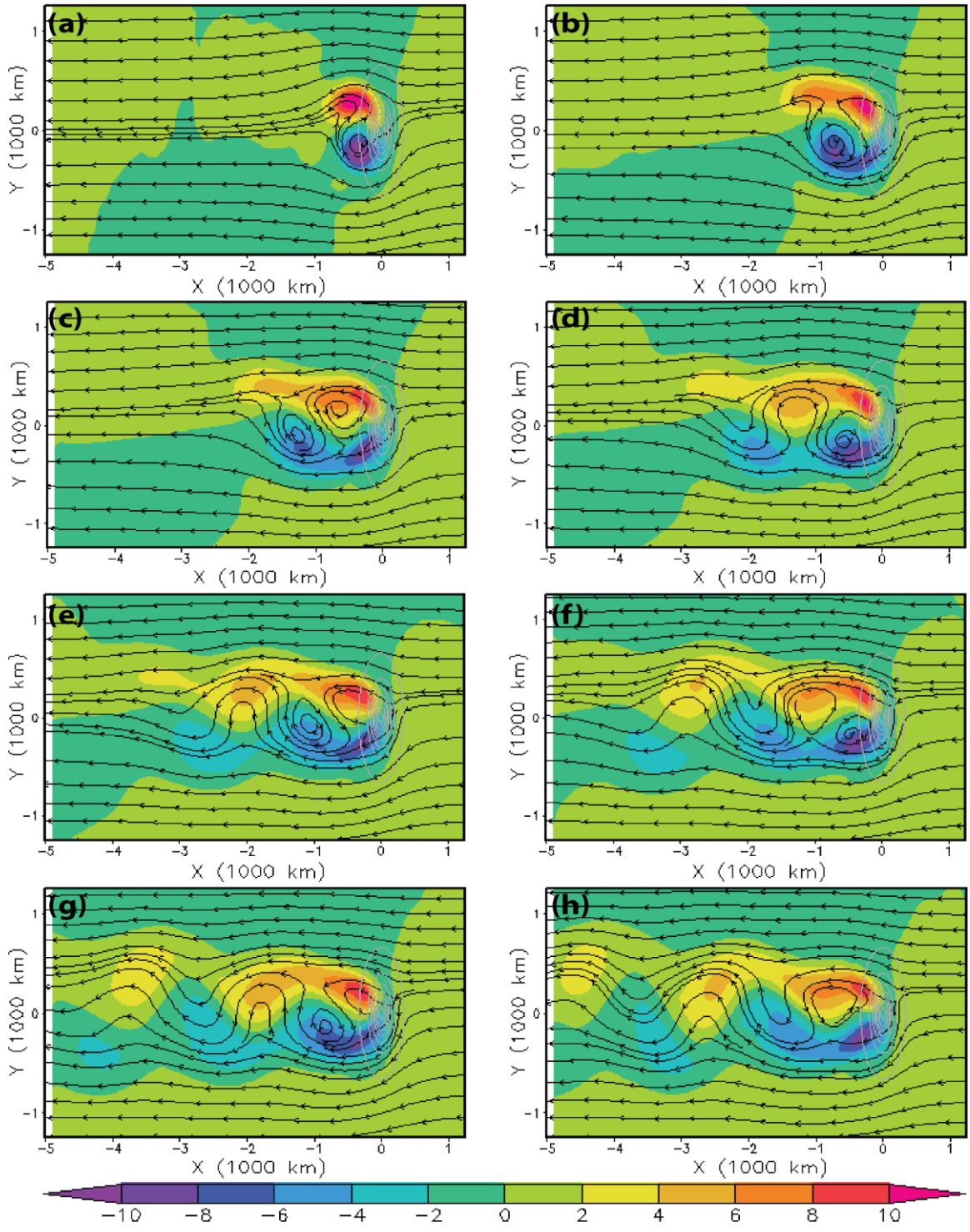

Figure 3.1. Simulated vorticity (10^{-5} s^{-1}) and streamlines on a β-plane centered at 10°N for control Case A* at nondimensional time $\hat{t}$ = (a) 5.76 (1 day) (b) 11.52 (c) 17.28 (d) 23.04 (e) 28.8 (f) 34.56 (g) 40.32 (h) 46.08 (8 days). The topography contour interval is 500 m.

Due to orographic blocking, the easterly flow split near the eastern part of the mountain and generates a stagnation point to the northeast of the mountain. Unlike the case without Coriolis force (to be discussed later), the stagnation point is shifted to the right (facing downstream) of the incoming flow. This shift of stagnation point can be explained by the basic dynamics, as explained in textbooks (e.g., Lin 2007). Briefly speaking, when the incoming flow is blocked by the mountain, its wind speed is reduced due to the high pressure built up over the mountain. This, in turn, reduces the Coriolis force; owing to the excessive pressure gradient force, most of the flow moves southward to go around the mountain. A flow imbalance is induced on the lee side, as part of the geostrophic adjustment process. Because of the Earth rotational effect in the Northern Hemisphere, the positive vorticity at the lee side develops more quickly than the negative vorticity in the simulation at nondimensional time $\hat{t}$ = 5.76 (1 day), as discussed in Lin et al. (1992). Accordingly, streamlines shift northward, and thus, there is a region of dense streamlines at the lee. Gradually a series of positive vorticity and negative vorticity form in the northern part and southern part of the lee, respectively. Hence, the streamlines at the lee side meander cyclonically around the positive vorticity region and wind anti-cyclonically around weaker negative vorticity region. Sometimes vortices, which are shown as closed streamlines, are formed around positive or negative vorticity regions. The wave-like disturbances have a wavelength about 2000 km and a period of 2~3 days. The associated wave disturbance propagating speed is about 9.6 ms^{-1}. The wavelength, period, and wave propagating speed are comparable to the characteristics of observed AEWs (wavelength 2500 km, period 3.5 days, and propagating speed 8 ms^{-1}) (Reed et al. 1977), those associated with pre-Alberto (2000) AEW (wavelength 2200 km, period 2~3 days, and propagating speed 11.6 ms^{-1}) (Lin et al. 2005) and those associated with pre-Debby (2006) AEW (wavelength 2000 km, and propagating speed

7.9 ms^{-1}) (Lin 2009). The surface vorticity downstream 3750~5000 km at the lee side is about -2×10^{-5} - 4×10^{-5} s^{-1}, which is close to -2×10^{-5} - 2×10^{-5} s^{-1} in Reed et al. (1977). Hence, EH may generate AEWs. The largest vorticity and zonal wind deviations are located at the surface in the present idealized simulations, which is consistent with the confinement to the lower troposphere in pre-Debby AEW (2006) (Lin 2009), rather than at 700 mb in Reed et al. (1977). The discrepancy is attributed to the lack of planetary boundary layer and baroclinicity in the current model simulation. In particular, the existence of baroclinicity would elevate the maximum wind to a higher altitude, such as 600 mb or so, where the African easterly jets are observed.

Figure 3.2 shows the surface vorticity, streamlines, surface potential vorticity, surface pressure perturbation, wind vectors, and vertical cross sections of vertical velocity and potential temperature fields of control case A* (Figure 3.1) after nondimensional time $\hat{t}$ = 46.08 (8 days). Note that the pattern of the surface potential vorticity field is similar to that of the surface vorticity field. Furthermore, three low pressure regions are co-located with three positive surface vorticity fields. Because of the compensation of adiabatic warming of the flow going over the mountain there is no positive surface pressure perturbation on the lee. Wind speeds at the top of mountain are larger than those upstream and downstream due to the Bernoulli effect. The wind speeds of the southerly wind and the northerly wind larger than 20 ms^{-1} may be associated with barrier winds (Parish, 1982), which are related to the convergences on the lee. The disturbances of vertical velocity and potential temperature propagate upward and tilt with decreasing amplitudes. The phase-tilt with decreasing wavelength with height of the vertical cross sections of vertical velocity and potential temperature indicate that the orographyically generated waves are a mixture of vertically propagating waves and evanescent waves. Since the wavenumbers for

flows going over such a bell-shaped mountain are continuous, the flow regime is continuous. The tilted vertically propagating gravity waves reach a quasi-steady state in a relatively short time period, $\hat{t}$ = 5.76 (t = 1 day). The amplitude of the vertically propagating gravity waves increases with time at low levels.

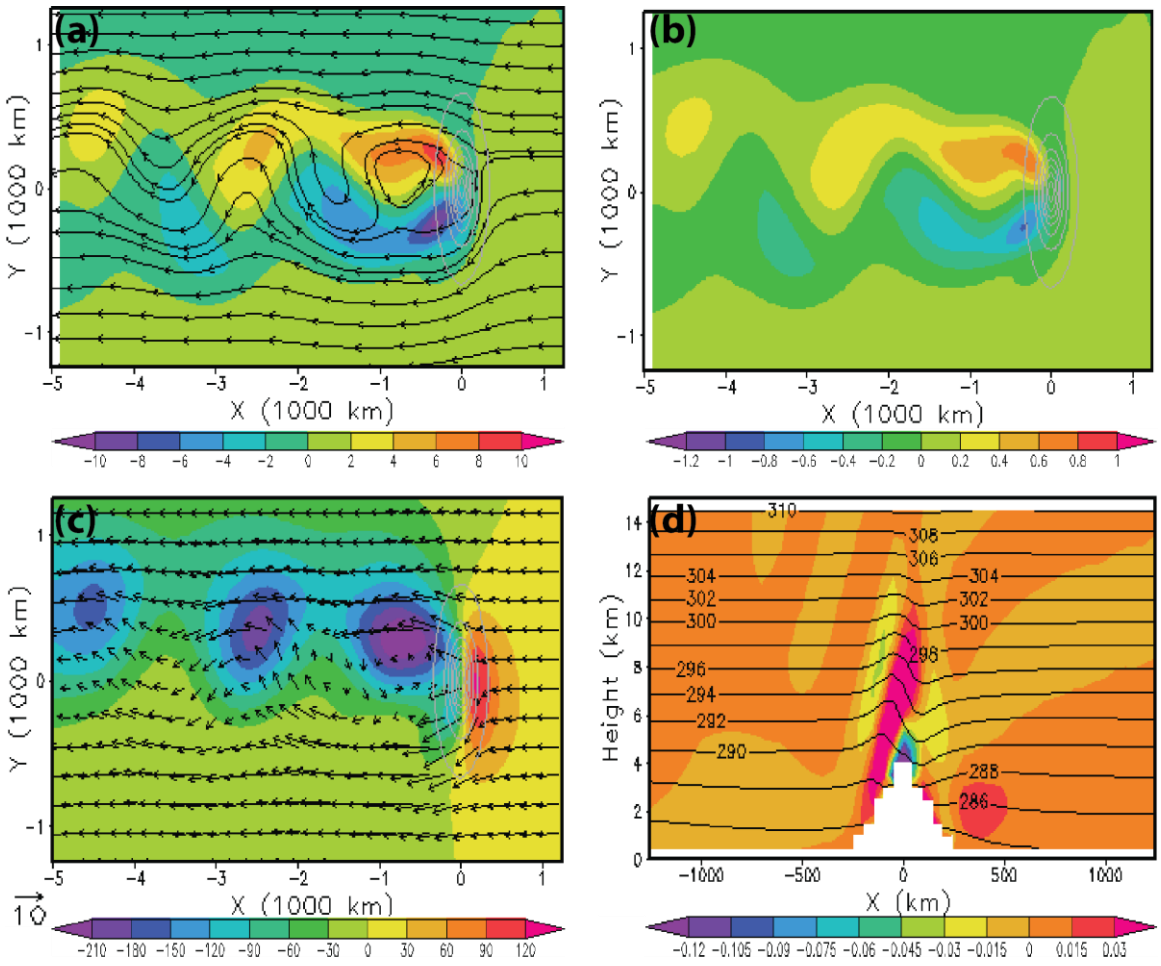

Figure 3.2. (a) Surface vorticity, and streamlines, (b) surface potential vorticity, (c) surface pressure perturbation, and wind vectors, and (d) vertical cross sections of vertical velocity and potential temperature on a β-plane centered at 10°N for Case A* at nondimensional time $\hat{t}$ = 46.08. The topography contour interval is 500 m.

The propagation speeds of the AEW-like waves may be estimated by the linear dispersion relationship. The dispersion relationship of linear, hydrostatic, continuously stratified inertia-gravity waves on a β plane is derived in the Appendix. Both the wave frequencies and phase speeds for $n = 0$ and for $n = 1$ are calculated in the Appendix as well. The three roots of the linear dispersion relationship correspond to an eastward propagating gravity wave, westward propagating mixed Rossby-gravity wave, and a westward propagating gravity wave with the phase speed 0.201 ms^{-1}, -10.20 ms^{-1}, and -20 ms^{-1}, respectively, when $n = 0$. Based on the propagating speed estimates, the westward propagating mixed Rossby-gravity wave fits with the observed AEW and the propagating speed 9.6 ms^{-1} in the idealized simulation. On the other hand, for flow pass a large-scale mountain, β effects are important. Hence, the waves in the simulations are forced topographic Rossby waves.

3.3.2. Effects of Earth's Rotation. In order to study the Earth rotational effects, we perform a simulation (Case B1) identical to the control case except on an *f*-plane centered at 10^{o}N, instead of on the β-plane. Figure 3.3 shows the surface vorticity, streamlines, surface potential vorticity, surface pressure perturbation, wind vectors, and vertical cross sections of vertical velocity and potential temperature of Case B1 in the simulation at nondimensional time $\hat{t}$ = 46.08 (8 days). These flow patterns on an *f*-plane are significantly different from those on a β-plane in Figure 3.3. The magnitudes of surface vorticity and surface pressure perturbation on an *f*-plane are much smaller than those on a β-plane. The vorticities on an *f*-plane decay after nondimensional time $\hat{t}$ = 17.28 (3 days) and move faster than those on a β-plane. Therefore, there is only one major wave present after day 8 (Figures 3.3a and 3.3c), instead of three waves (Figures 3.2a and 3.2c). The β effect appears to play an important role in maintaining the wave patterns and vorticity. This means that the mountain-induced waves are less dispersive on a β-

plane, and thus, are dominated by the Rossby waves. The surface pressure perturbations on an *f*-plane are weaker and move faster than those on a β plane from the beginning. The windward high pressure extends farther to the lee side. The vertical cross sections of vertical velocity and potential temperature demonstrate similar patterns to those on a β-plane, with smaller amplitudes and vertical wavelengths, propagating more perpendicularly on an *f*-plane than on a β-plane. Therefore, the vertically propagating disturbances are more dominated by the evanescent waves.

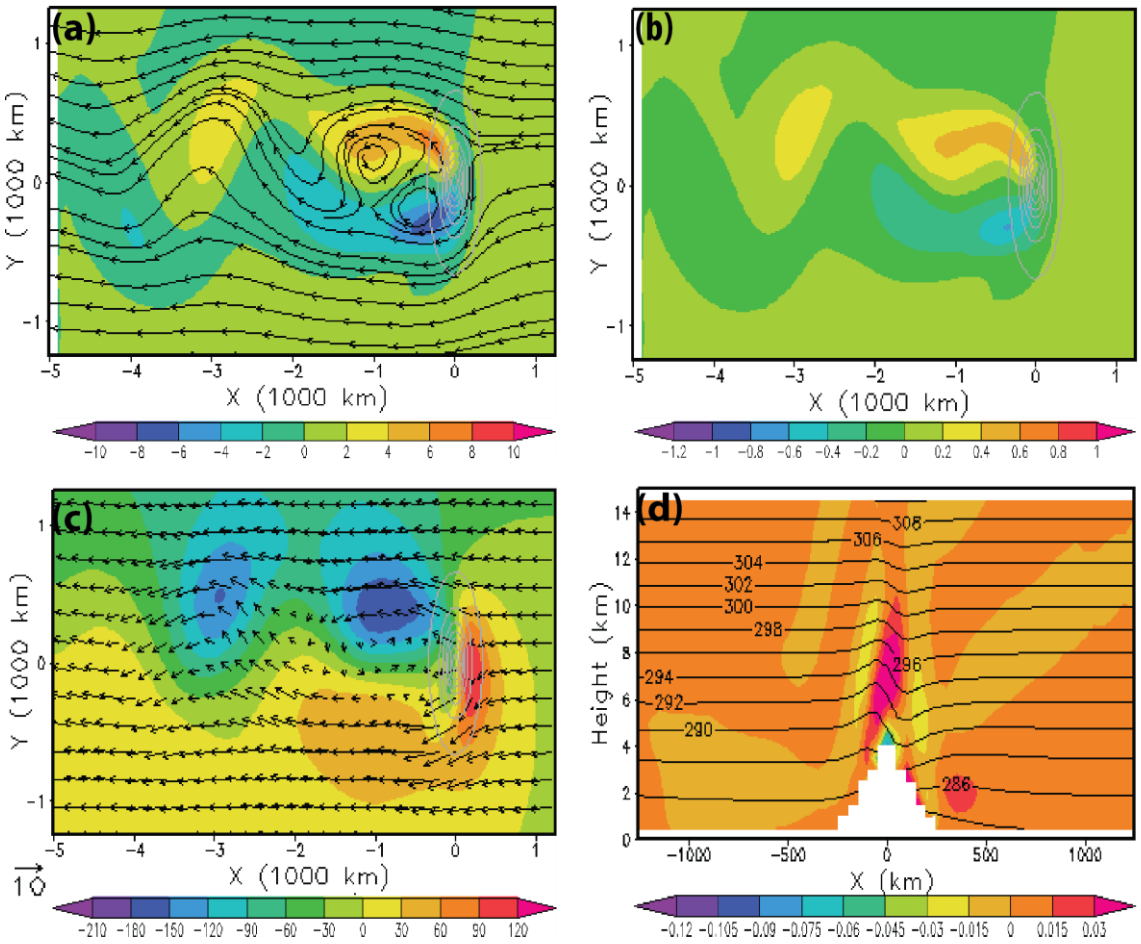

Figure 3.3. Same as Figure 3.2 except on an *f*-plane for Case B1

Figure 3.4 shows the flow fields for Case B2 similar to the control case but without Coriolis force in the simulation at nondimensional time $\hat{t}$ = 46.08 (8 days). The surface vorticity, streamlines, wind vectors, and surface pressure perturbation fields are symmetric with respect to

the south-north center line of the bell-shaped topography in a non-rotating flow. The surface vorticity and surface pressure perturbation fields are much weaker than those on a β-plane or an *f*-plane. This indicates that the importance of Coriolis force in the development of lee vorticity and pressure perturbation. In fact, the Coriolis force provides the asymmetric forcing which is needed for vortex shedding on the lee side of a symmetric mountain (e.g. Lin, 2007). Coriolis force strengthens surface vorticity and surface pressure perturbation at the lee side, results in dominating positive vorticity and negative pressure perturbation, and creates wave-like disturbances of streamlines (Figs. 3.3 and 3.4). Also, Coriolis force does not change much on the patterns of vertical cross sections of vertical velocity and potential temperature which have smaller amplitudes and propagate more perpendicularly than those on a β-plane and on an *f*-plane. Hence, the vertically propagating disturbances are dominated by the evanescent waves.

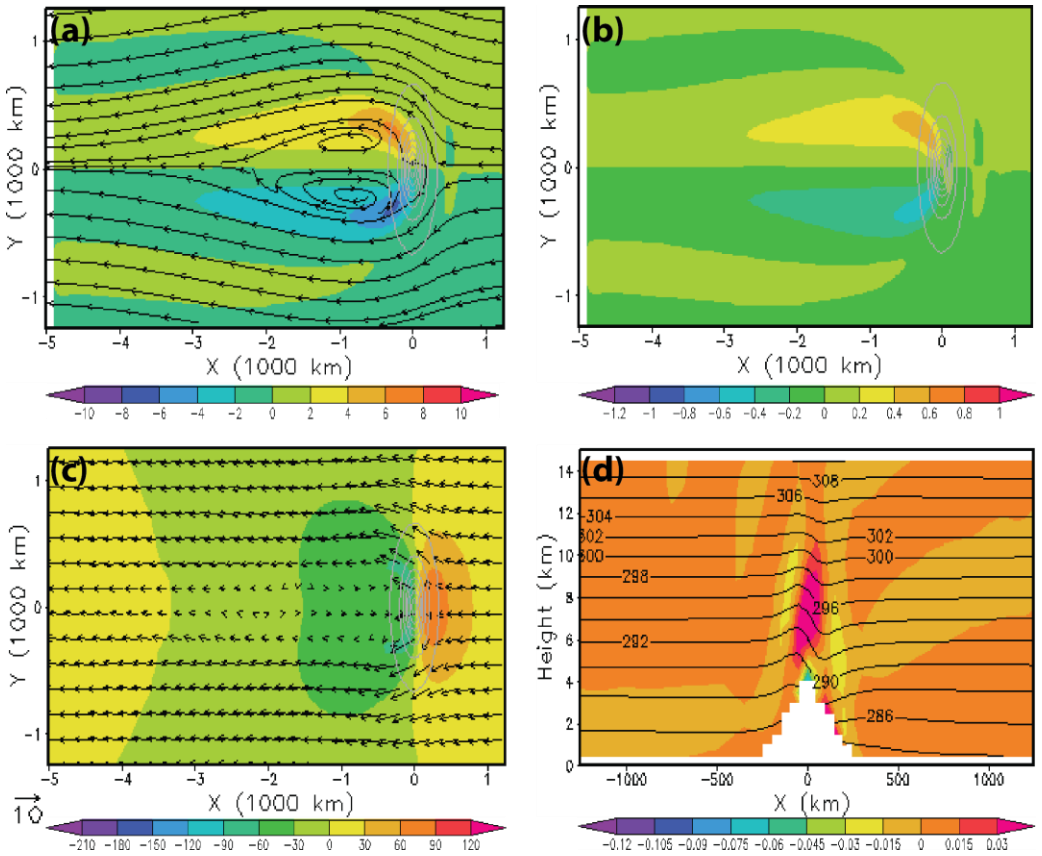

Figure 3.4. Same as Figure 3.2 except without Coriolis force for Case B2

That orographically generated waves propagate more slantwise on a β-plane and less tilting without Coriolis force is consistent with the hydrostatic inertia-gravity wave theory, such as in Lin (2007).

$$\left|\frac{C_{gz}}{C_{gx}}\right| = \left|\frac{k}{m}\right| = \frac{(\omega^2 - f^2)^{1/2}}{N}, \omega = kU \tag{1}$$

3.3.3. Effects of Varying Latitude. The latitudes under discussion are 0°N, 10°N, 20°N, and 30°N, and the associated Rossby numbers (*Ro*) are ∞, 0.66, 0.33, and 0.23, respectively. The simulation domain at the lee side is large enough (5000 km × 5000 km) that β effects can play a role in the development of vorticity and negative pressure perturbations. In terms of the evolution of vorticity and negative pressure perturbations, both *f* and β effects are essential. It is not that the larger the planetary vorticity, the larger magnitudes the vorticity and negative pressure perturbations, rather, as Figure 3.5 shows, the patterns and strengths of surface vorticities on a β-plane centered at 20°N (Case C3) and 30°N (Case C4) in the simulation at nondimensional time $\hat{t}$ = 46.08 (8 days) are similar to the vorticity on a β-plane centered at 10°N (Case C2). Generally, surface vorticity fields at 30°N are slightly weaker than those at 10°N and 20°N on both a β-plane and an *f*-plane because that planetary vorticity at 30°N is not large and that β effects at 30°N is weak. Therefore the streamlines at 30°N are not as meandering as those at 10°N and 20°N on both a β-plane and an *f*-plane.

Figure 3.6 demonstrates that the strengths of both positive and negative pressure perturbations at 20°N and 30°N are much stronger than those at 10°N on both β-plane and *f*-plane from the beginning. The β effects are the largest at 0°N. The β effects at 0°N do create surface vorticity and surface pressure perturbations sticking to the topography with larger magnitudes than those in the condition without Coriolis force on an *f*-plane. But the β effects at

0°N are not able to provide asymmetric forcing to produce vortex shedding at the lee of the mountain. Similar to the situation at 10°N, the surface vorticities at 0°N, 20°N or 30°N on a β-plane are stronger than those at 0°N, 20°N or 30°N on an f-plane correspondingly from the nondimensional time $\hat{t}$ = 11.52 or 17.28 (2 or 3 days).

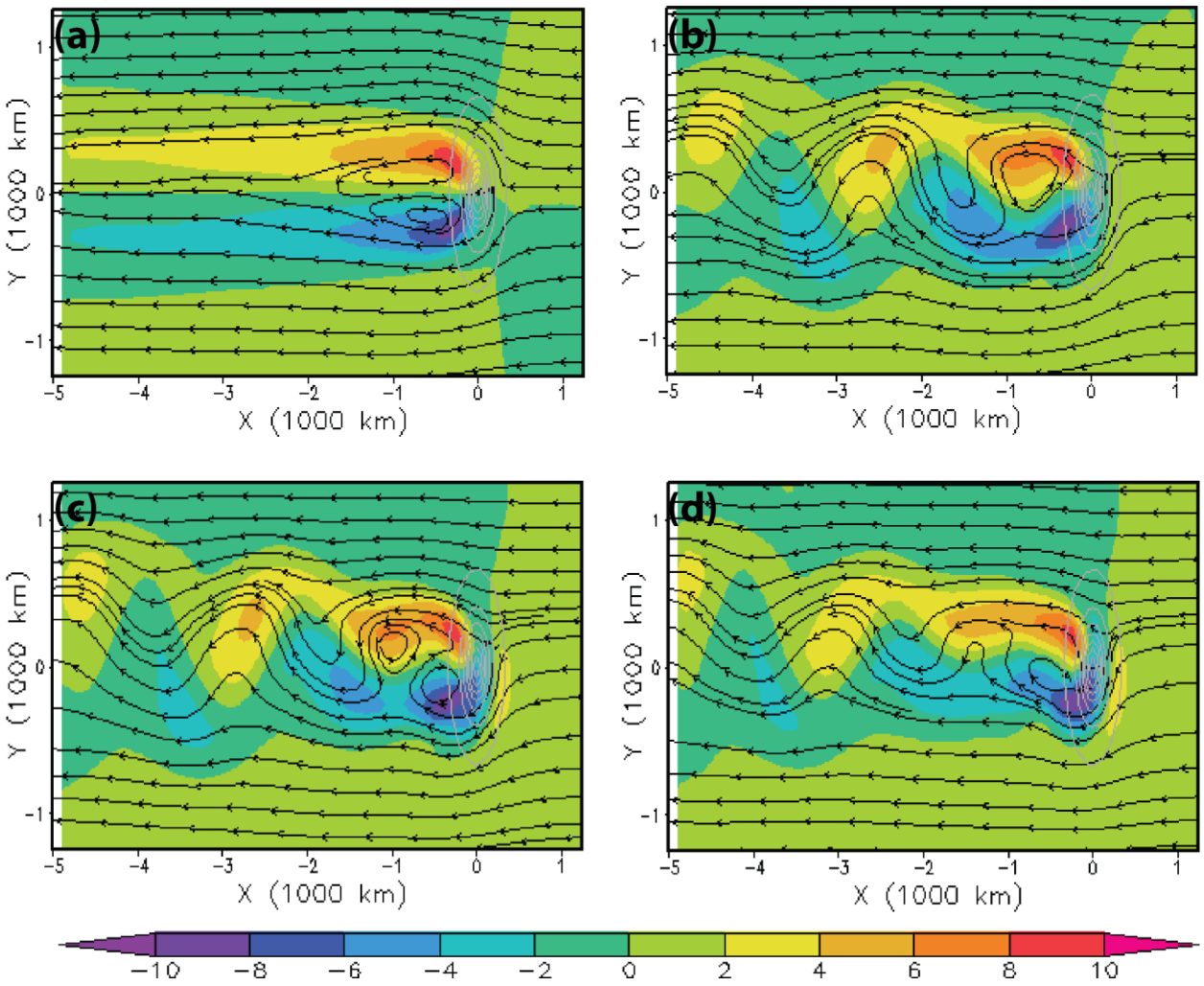

Figure 3.5. Simulated vorticity (10^{-5} s^{-1}) and streamlines at nondimensional time $\hat{t}$ = 46.08 on a β-plane centered at (a) 0°N (Case C1), (b) 10°N (Case C2), (c) 20°N (Case C3), and (d) 30°N (Case C4). The topography contour interval is 500 m.

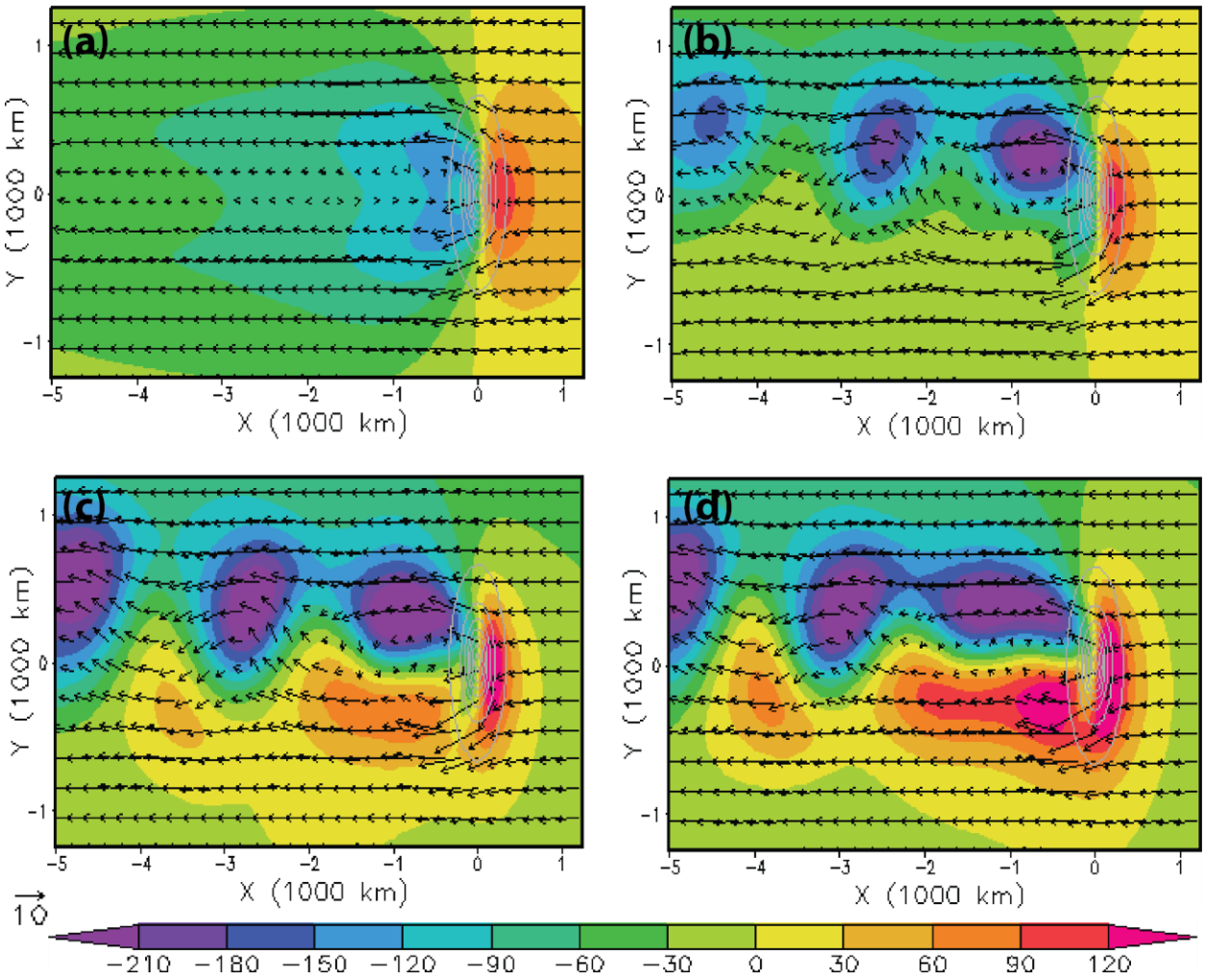

Figure 3.6. Same as Figure 3.5 (Cases C1-C4) except for surface pressure perturbation (Pa), and wind vectors fields

Again, β effects are important in making the forced waves less dispersive at 0°N, 20°N and 30°N. The pressure perturbations at 0°N, 20°N or 30°N on a β-plane are larger than those at 0°N, 20°N or 30°N on an *f*-plane, respectively from the beginning. The β effects do help develop negative pressure perturbations and weaken positive pressure perturbations. But the differences in strength between a β-plane and an *f*-plane at 20°N or 30°N are not as significant as those at 10°N or 0°N. This reveals that β effects are important in the development of pressure

perturbations at both 10°N and 0°N. The windward positive pressure perturbations at 20°N and 30°N on both a β-plane and an *f*-plane extends to the lee side. Furthermore, the tilting pattern and amplitudes of vertical velocity and potential temperature at 20°N and 30°N do not change much on both a β-plane and an *f*-plane. The amplitudes of vertical velocity and potential temperature on a β-plane are slightly larger than those on an *f*-plane at the latitudes discussed (not shown).

3.3.4. Effects of Uniform Basic Wind Speed. In studying the effects of uniform basic wind speed we vary U = -20 ms^{-1} (Case D1: Ro=1.3, Fr=0.57, $\hat{\beta}$=0.40), U = -10 ms^{-1} (Case D2: Ro=0.66, Fr=0.29, $\hat{\beta}$=0.81), to U = -5 ms^{-1} (Case D3: Ro=0.33, Fr=0.14, $\hat{\beta}$=1.6) with the same topography parameters and the same latitude 10°N on a β-plane. The case of uniform basic wind -20 ms^{-1} (Case D1) has the largest Ro and Fr, and the least $\hat{\beta}$ among three cases. Fr is a measure of nonlinearity. Namely, Case D1 has the largest ratio of inertial to Coriolis force, the least flow nonlinearity, and the least ratio of β effects to inertial force. Here, the inertial force is measured by wind speed. The surface vorticity and streamline fields demonstrate that the inertial force is more essential in the development of lee surface vorticity and wandering streamlines than flow nonlinearity, and β effects under the same blocking of topography and the same Earth rotational effects (at the same attitude) within the period from nondimensional time $\hat{t}$ = 0 to $\hat{t}$ = 28.8 (5 days) in terms of Ro, Fr, and $\hat{\beta}$. The surface vorticity and streamlines start to weaken after nondimensional time $\hat{t}$ = 28.8 (5 days) implying that flow nonlinearity and/or $\hat{\beta}$ effects are fundamental to sustain surface vorticity and streamlines for more than five days as shown in Figure 3.7.

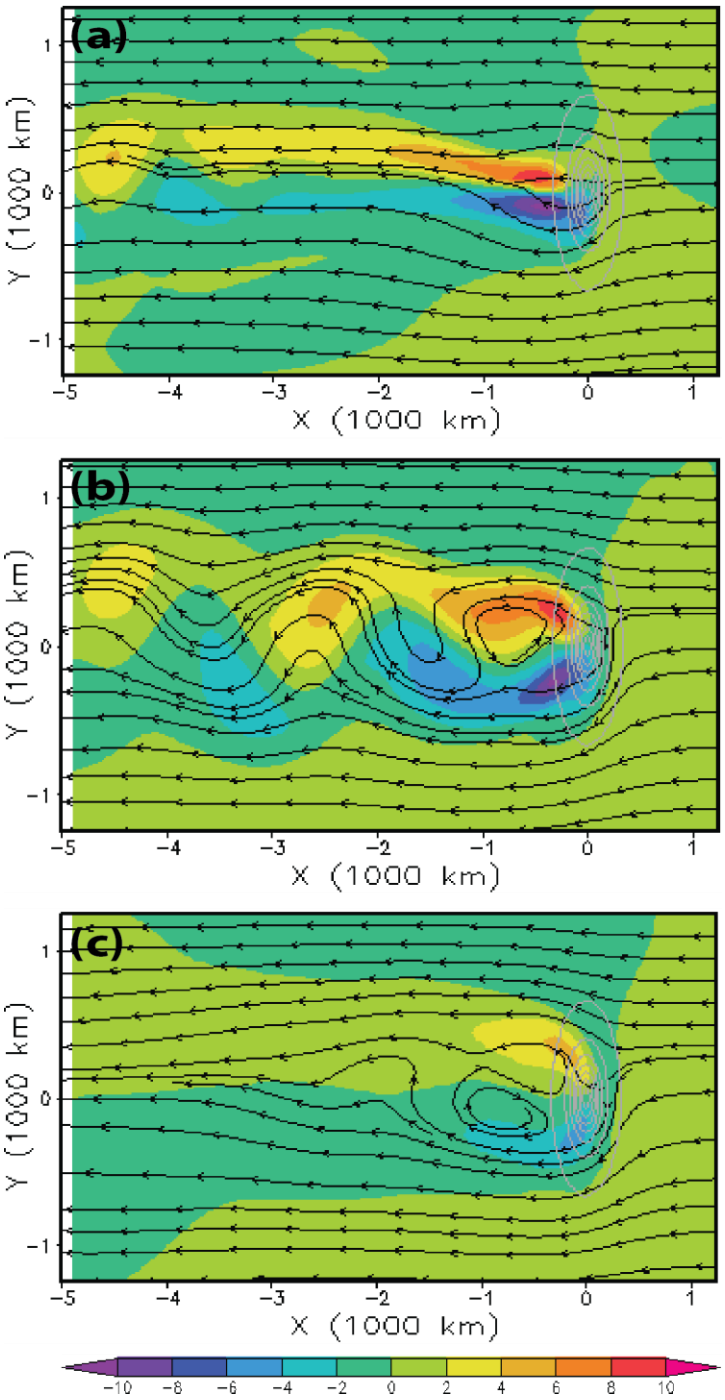

Figure 3.7. Simulated vorticity (10^{-5} s^{-1}) and streamlines after simulation on a β-plane centered at 10°N at nondimensional time $\hat{t}$ = 46.08 when uniform wind is (a) -20 ms^{-1} (Case D1), (b) -10 ms^{-1} (Case D2), (c) -5 ms^{-1} (Case D3). The topography contour interval is 500 m.

The result is consistent with those shown in the effects of the Earth's rotation and varying latitude, in which surface vorticity and streamlines weaken after nondimensional time $\hat{t}$ = 17.28 (3 days). The patterns of surface pressure perturbations support that inertial force outweighs flow nonlinearity and β effects. Especially in the case of uniform basic wind U = -5 ms^{-1} (Case D3), the wind is so weak that most of the air parcels cannot pass over the mountain, but rather, they go around the mountain. Namely, the case of uniform basic wind U = -5 ms^{-1} falls into the *flow-around regime*. Hence, there are not many gravity waves generated and thus Case D3 belongs to the evanescent flow regime as evidenced by the almost erect vertical velocity and potential temperature fields and significant decrease with height as displayed in Figure 3.8. Unlike the case of U = -5 ms^{-1}, the streamlines on the surface (Figure 3.7a), the wind vectors (not shown), and potential temperature and vertical velocity on the vertical cross section (Figure 3.8a) of U = -20 ms^{-1} indicate that Case D1 indeed falls into *the flow-over regime*.

Because the strong wind flows over a mountain of 3500 m is accompanied by adiabatic warming along the lee slope, the vertical cross sections of vertical velocity and potential temperature have much larger amplitudes and vertical wavelengths for the case of uniform basic wind U = -20 ms^{-1} (Case D1) than those in the other two cases (Cases D2 and D3). In Case D1, the result is consistent with the ratio of the vertical to horizontal component of group velocity for hydrostatic inertia-gravity waves in (1). As a matter of fact, it is different from the evolution of relative vorticity field when the amplitude of the vertically propagating gravity wave becomes larger with time and the vertical wavelength becomes larger during nondimensional time $\hat{t}$ = 46.08 (8 days). Buoyancy force produced by flow over the mountains is the source of vertical propagating waves. The larger Froude number results in more linear flow, which is able to climb over mountains and create vertical propagating waves.

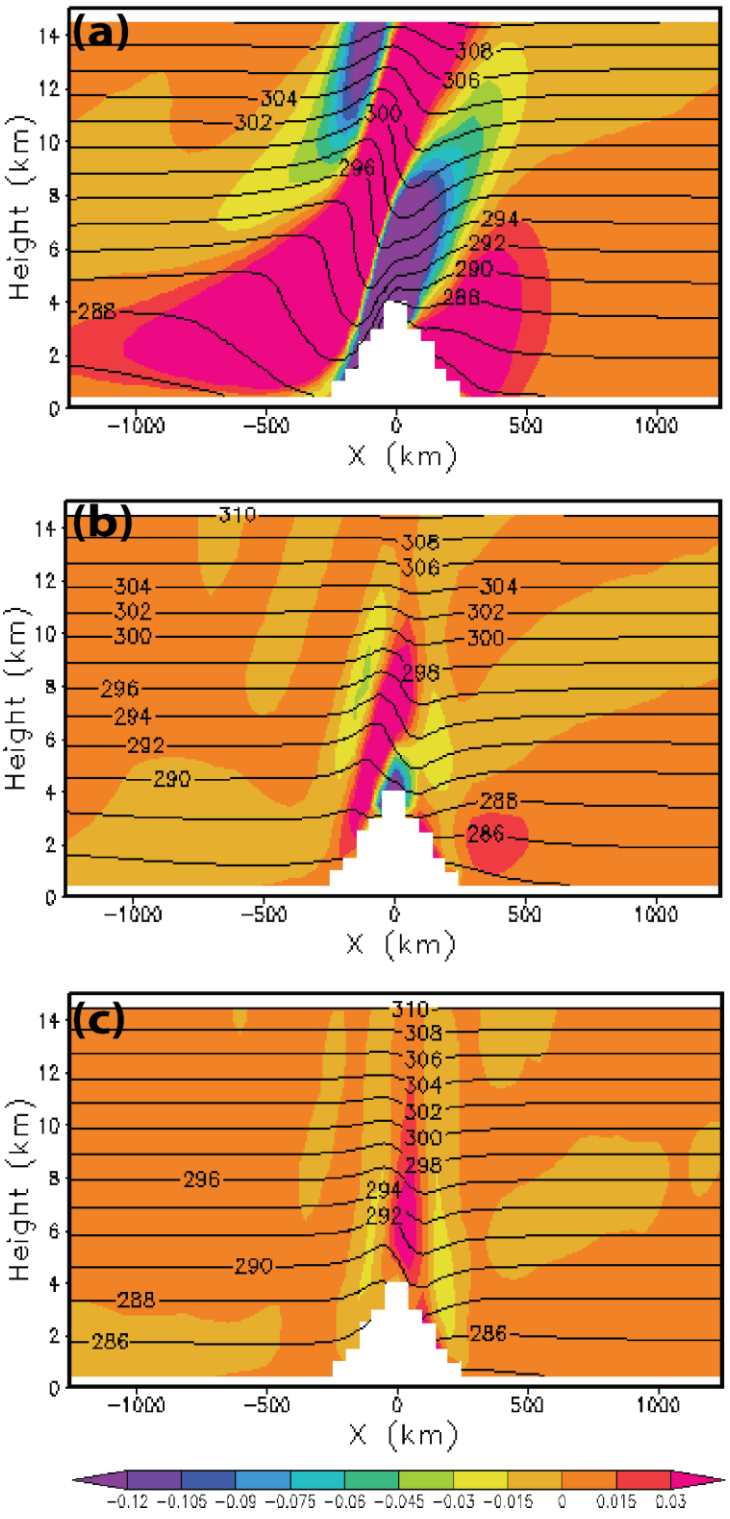

Figure 3.8. Same as Figure 3.7 (Cases D1-D3) except for the vertical cross sections of vertical velocity (ms^{-1}) and potential temperature (K) fields along 10°N latitude.

The β effects have large effects on vorticity development at the lee side, but it has little effects on flows over mountains. Therefore, the nonlinearity and β effects are negligible in the evolution of the vertically propagating gravity wave, and thus, the trends in the progression of amplitude, and vertical wavelength tilting of group velocity do not change after nondimensional time $\hat{t}$ = 28.8 (5 days). Still, the amplitudes at upper levels are much smaller than those at lower levels. Hence, the vertical disturbances are dominated by vertically propagating gravity waves in the vertical cross sections of vertical velocity and potential temperature.

3.3.5. Effects of Vertical Wind Shear. The effects of vertical wind shear are investigated by varying the Richardson number ($Ri = N^2/U_z^2$), when the other nondimensional parameters such as Ro, Fr, $\hat{\beta}$, h_0/a, and b/a are kept constant. In the following, we consider N = 0.01 and $Ri = \infty$ (U_z = 0 s^{-1}, Case E1), Ri = 400 (U_z = -0.5×10^{-3} s^{-1}, Case E2), Ri = 100 (U_z = -1×10^{-3} s^{-1}, Case E3), Ri = 25 (U_z = -2×10^{-3} s^{-1}, Case E4). The AEJ has a maximum of 14~15 ms^{-1} at 600 mb (~ 4km) (Shen et al. 2010), which leads to a wind shear of 0.001 s^{-1} if the surface wind is about 10 ms^{-1}. All cases are dynamically stable because Ri's are larger than 0.25. The basic wind speed at the surface is -10 ms^{-1} in all cases. Figures 3.9 and 3.10 indicate that when the vertical wind shear increases, the associated meridional temperature gradient and pressure gradient become larger, making negative pressure perturbations move and develop southward, and have less and less wandering streamlines at the nondimensional time $\hat{t}$ = 46.08 (8 days). The vertical cross sections of potential temperature show that warmer potential temperatures at both the top and the surface due to downslope adiabatic warming at the lee for nondimensional time $\hat{t}$ = 46.08 (8 days) given larger vertical wind shears. The magnitudes of vorticity fields in Cases E2 and E3 are larger than that in Case E1 (no vertical wind shear) because of the larger inertial forces in the shear layer.

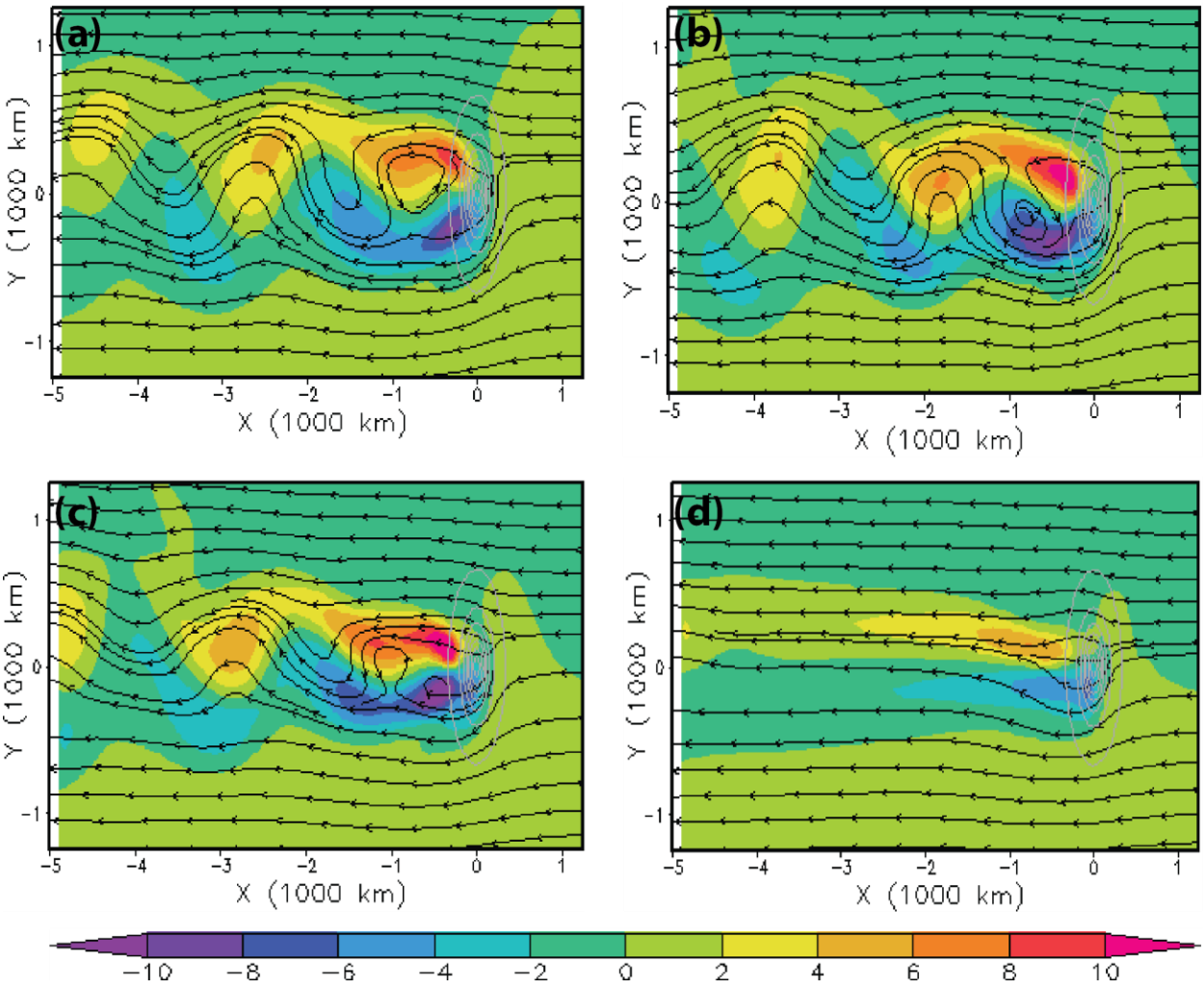

Figure 3.9. Simulated relative vorticity (10^{-5} s^{-1}) and streamlines for shear flow over a bell-shaped mountain on a β-plane centered at 10°N at nondimensional time $\hat{t}$ = 46.08 with U_z = (a) 0 s^{-1} (Case E1), (b) -0.5×10^{-3} s^{-1} (Case E2), (c) -1×10^{-3} s^{-1} (Case E3), (d) -2×10^{-3} s^{-1} (Case E4). The topography contour interval is 500 m.

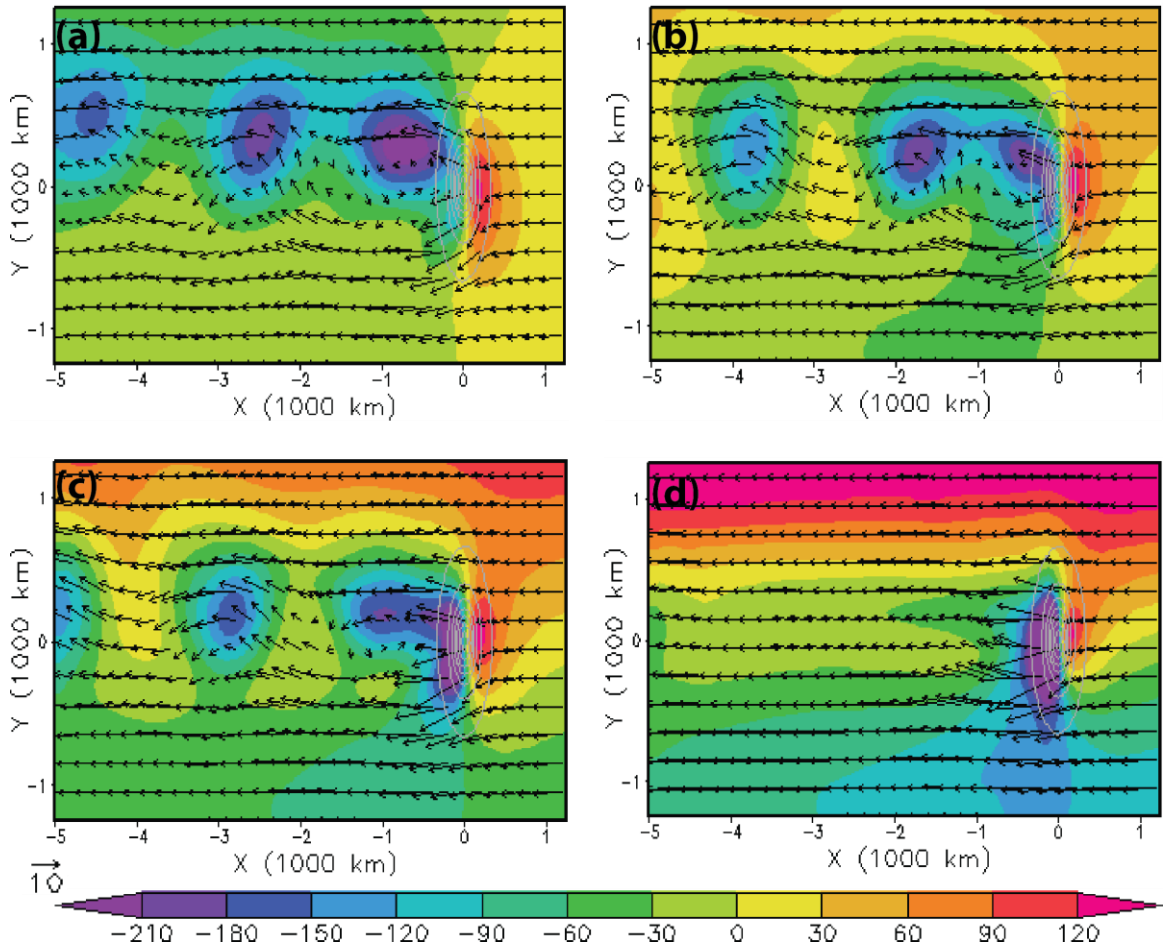

Figure 3.10. Same as Figure 3.9 (Cases E1-E4) except for pressure perturbation (Pa) and wind vector fields.

For the Case E4, the orographically induced meridional temperature gradient and pressure gradient gradually dominate. The associated large wind advects lee vorticities further downward. The surface vorticity and winding streamlines weaken after nondimensional time $\hat{t}$ = 11.52 (2 days). As the meridional pressure gradient gradually establishes, the wind field is nearly straight and becomes larger, resulting in weaker vorticity and more straight streamlines. Therefore, the vorticity and streamlines of Case E4 are very different from those of the other three cases (Cases E1, E2, and E3) at nondimensional time $\hat{t}$ = 46.08 (8 days). Case E4 infers that large vertical wind shear would gradually suppress the developments of surface vorticity and meandering

streamlines; i.e. the shedding vortices. Similar to Case D1 (U = -20 ms^{-1}) the progression of the vertically propagating gravity waves in Case E4 (Figure 3.11d) during nondimensional time $\hat{t}$ = 46.08 (8 days) is very different from that of vorticity in that the vertical wavelength becomes larger when the amplitude increases. The trends in the progression of amplitude, vertical wavelength, and tilting of group velocity do not change much after nondimensional time $\hat{t}$ = 28.8 (5 days). Thus, the vertical wind shear effects do not suppress the evolution of vertical propagating waves, but foster them with increasing amplitude and vertical wavelength (Figure 3.11). The impacts of the vertical wind shear effects on the evolution of vertical propagating waves are similar to increasing uniform basic wind speed. Effects of vertical wind shear make the vertically propagating gravity waves extend to higher level. The vertical disturbances in Case E4 are dominated by vertically propagating gravity waves (Figure 3.11d).

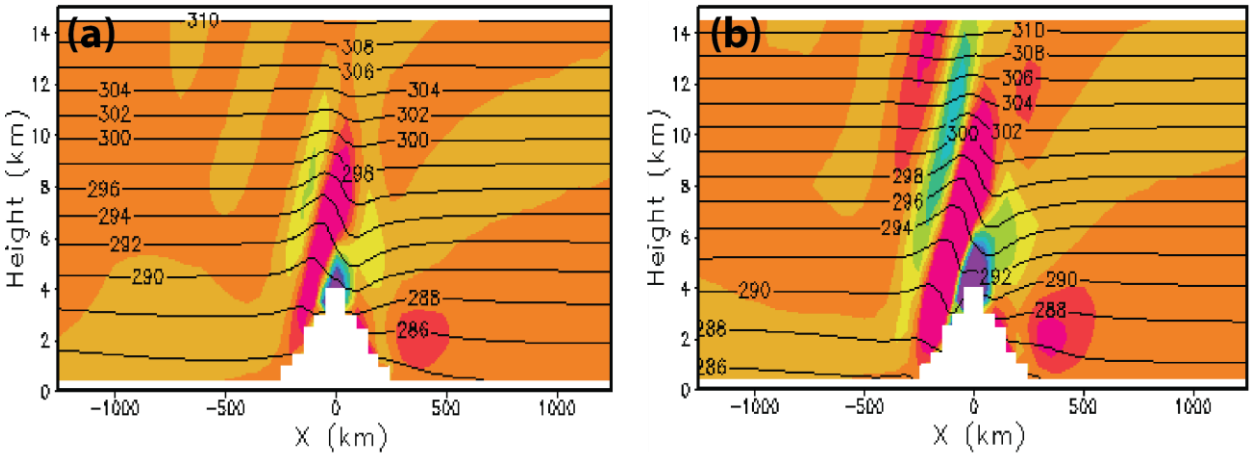

Figure 3.11. Same as Figure 3.9 (Cases E1-E4) except for the vertical cross sections of vertical velocity (ms^{-1}) and potential temperature (K) along 10°N

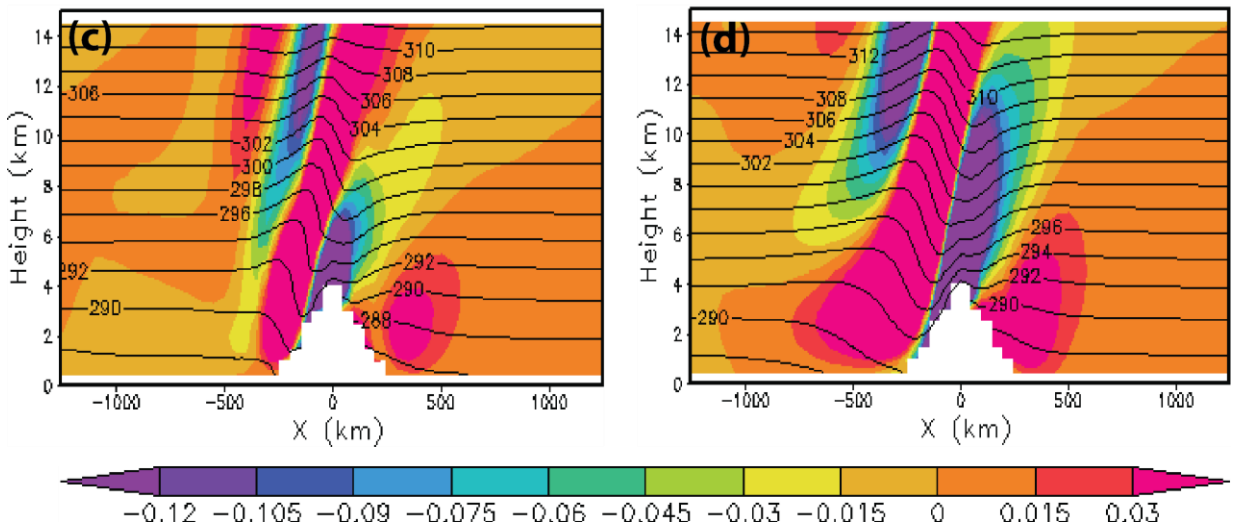

Figure 3.11. (Cont.)

In the Cases E2 and E3 (U_z = -0.5×10^{-3} s^{-1} and -1×10^{-3} s^{-1}, respectively) the orographically induced meridional temperature gradient and pressure gradient are not large enough to have dominating impacts on streamlines and vorticities during nondimensional time $\hat{t}$ = 46.08 (8 days) (Figures 3.9b and 3.9c), but only distort the patterns of negative pressure perturbations at the lee of topography. Moreover, as the vertical wind shear becomes larger, because of associated larger wind speed above the surface, the amplitude of the vertical disturbances in vertical cross section of vertical velocity and potential temperature are larger as in Figure 3.11. In fact, the fields in Cases E2 and E3 develop more slowly than those in Case E4. As the simulation time in the Cases E2 and E3 is extended much longer than nondimensional time $\hat{t}$ = 46.08 (8 days), gradually the meridional pressure gradient is established, and thus, the negative pressure perturbation at the lee side is weaken and confined to the mountain, the vorticity and streamlines are weaken and elongated, and the amplitudes and vertical wavelengths of the vertical propagating gravity waves enlarge (not shown). In short, the larger the vertical wind shear (i.e. the less the *Ri*), the less the lee vortices and the more vertically propagating

waves are generated, because more wave energy is propagated upward, instead of being advected downward in the long run.

3.3.6. Effects of Nonlinearity. The nonlinear effects are investigated by varying the Froude number (*Fr*). In order to keep all other nondimensional parameters (h_0/a, b/a, *Ro*, and $\hat{\beta}$) constant, the size of mountain (i.e. h_0, a, and b) is varied. In other words, the shapes of the mountains are kept the same; whereas the size of mountain changes. In this way, the only variable in nondimensional parameters is *Fr.* Therefore, zonal half-width (a) and meridional half-width (b) change with mountain height (h_0). In the following, we consider three cases: (1) Case F1: Fr=0.14 (h_0=7000 m, a=300 km, b=600 km); (2) Case F2: Fr=0.29 (h_0=3500 m, a=150 km, b=300 km); and (3) Case F3: Fr=0.57 (h_0=1750 m, a=75 km, b=150 km). In all the cases, U is kept constant as 10 ms^{-1}. Hence, the sizes of the mountains are significant. Note that blocking is the essential source of lee vorticity in an inviscid flow. When *Fr* is decreased, the zonal half-width and the meridional half-width are increased in order to keep the same nondimensional parameters h_0/a and b/a. Thus, blocking is increased, lee vorticity is strengthened, and streamlines meander. The effects of h_0/a and b/a will be discussed in the next two subsections. Figure 3.12 demonstrates that the smaller the *Fr*, the stronger the lee vortices and more wandering the streamlines become. In other words, in terms of mountains size, immense mountains create large vorticity (Figure 3.12a), whereas small hills only create very tiny vorticity (Figure 3.12c). The reason for this is that blocking has to be significant enough, i.e. *Fr* is small enough, to generate the vortex shedding. Surface pressure perturbation (not shown) has the same patterns as the vorticity. The negative pressure perturbation and barrier winds in the case of Fr=0.14 are very large; while in contrast, the negative pressure perturbation and barrier winds in the case of Fr=0.57 are negligible (not shown).

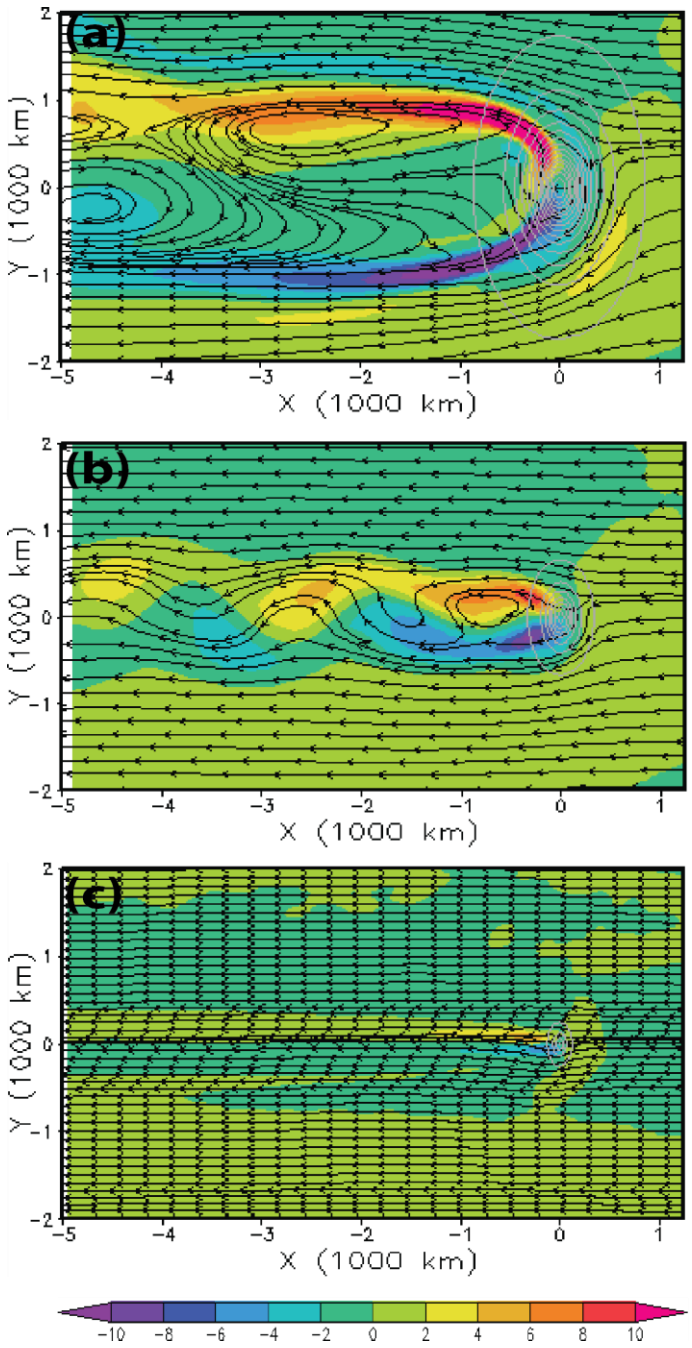

Figure 3.12. Simulated relative vorticity (10^{-5} s^{-1}) and streamlines for flow over a bell-shaped mountain with different geometry on a β-plane centered at 10°N at nondimensional time $\hat{t}$ = 46.08 for (a) Case F1: Fr=0.14 (h_0=7000 m, a=300 km, b=600 km), (b) Case F2: Fr=0.29 (h_0=3500 m, a=150 km, b=300 km), (c) Case F3: Fr=0.57 (h_0=1750 m, a=75 km, b=150 km). U = -10 ms^{-1} and N = 0.01 s^{-1} as in the control case. The topography contour interval is 500 m.

The very strong negative pressure perturbation in the case of Fr=0.14 is due to strong and large-scale downslope adiabatic warming at the lee from both a south wind and a north wind of a mountain with height 7000 m, whereas limited weak downslope adiabatic warming from a mountain with height 1750 m in the case of Fr=0.57 cannot produce strong negative pressure perturbation. The wind vectors (not shown) in all three cases display much larger wind speeds at the mountain peak than upstream and downstream slopes. Hence, the wind fields of all these three cases are caused by the Bernoulli effect.

The h_0/a of Cases F1 (Fr=0.14) and F2 (Fr=0.29) is 0.023. Note that the flow for the case of Fr=0.22 with h_0/a=0.12 kept constant in Smolakiewicz and Rotunno (1989; denoted as SR89 hereafter) is completely blocked. The obstacle in SR89 is much steeper, and thus, with much more blocking, than the mountains in the cases of F1 (Fr=0.14) and F2 (Fr=0.29), so that the responses in streamlines and wind vectors are very different between the two cases of F1 and F2 (Figures 3.12a and 3.12b), and those in SR89 in spite of similar Fr's. Note that the flow in SR89 is non-rotating which contributes to some major differences. The importance of mountain steepness will be discussed in next subsection. In addition, Figure 3.13 indicates that the amplitude of vertical velocity and potential temperature in Case F3 at low levels is much larger than those in Cases F1 and F2 because the mountain size of Case F3 is much smaller than those of Cases F1 and F2. Except the large amplitude of Case F3 at low levels, the tilting of the vertical disturbances in all three cases (F1, F2, and F3) are similar to each other; but the amplitudes decrease rapidly with height. The vertical wavelengths of the vertical disturbances in all three cases (F1, F2, and F3) are about 5 km estimating from vertical and horizontal cross sections of vertical velocity. The vertical wavelengths are smaller than 6.28 km estimated by linear hydrostatic mountain theory ($2\pi U/N$). The difference is due to nonlinearity.

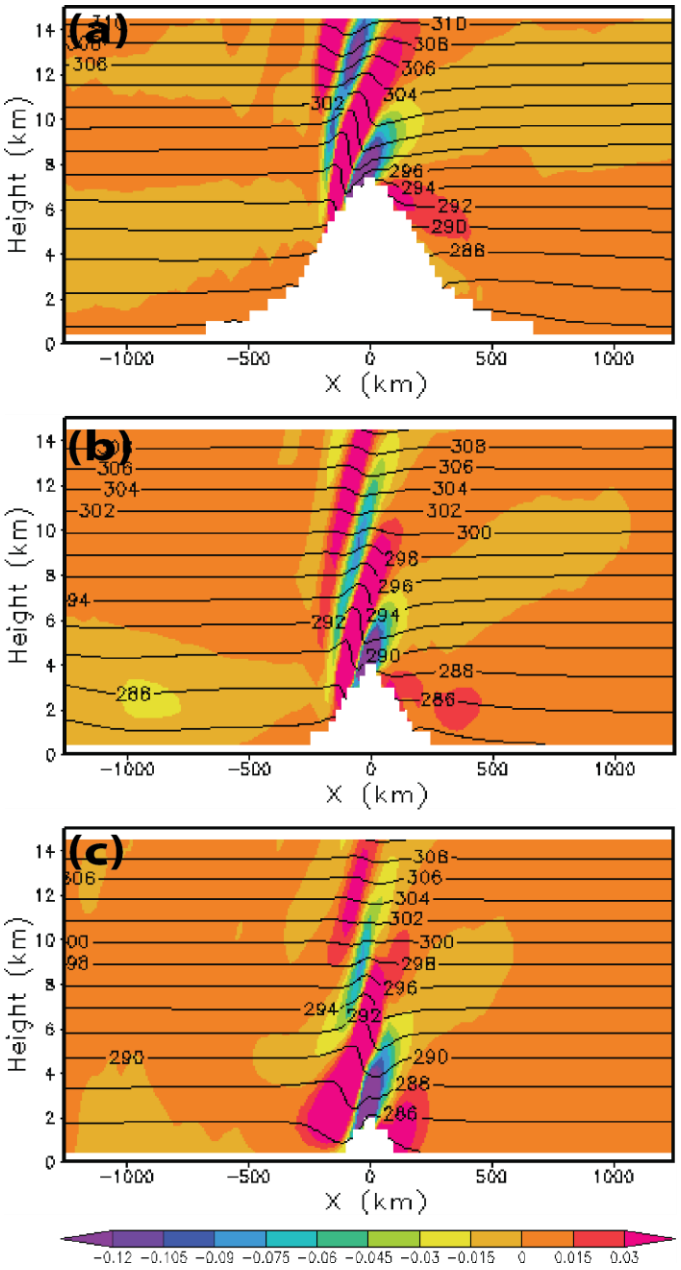

Figure 3.13. Same as Figure 3.12 (Cases F1-F3) except for the vertical cross sections of vertical velocity (ms^{-1}) and potential temperature (K) along 10°N.

3.3.7. Effects of Mountain Steepness. The effects of steepness are measured by the nondimensional parameter h_0/a with the nondimensional parameters *Ro*, *b/a*, and $\hat{\beta}$ kept constant. In particular, the zonal half-width (a) and meridional half-width (b) are kept constant. The mountain height (h_0) is the only parameter changed to give various cases of mountain

steepness. Three cases are considered: (1) Case G1: h_0/a=0.047 (h_0=7000 m, Fr= 0.14); (2) Case G2: h_0/a=0.023 (h_0=3500 m, Fr=0.29); and (3) Case G3: h_0/a=0.017 (h_0=1750 m, Fr=0.57). The increase in mountain steepness (h_0/a increased) makes the blocking stronger. Figure 3.14a shows that Case G1 gives the most significant surface vorticity and streamline perturbations at the lee side. In contrast, Case G3 demonstrates only very limited surface vorticity and streamline perturbations at the lee side. Similar to the effects of nonlinearity (subsection f), large blocking results in large scale downslope adiabatic warming at the lee from the topography with height 7000 m, and thus, well developed negative pressure perturbation at the lee, huge windward positive pressure perturbation and barrier winds in Case G1; whereas weak blocking only creates very weak downslope adiabatic warming at the lee, and thus very weak negative pressure perturbation without barrier winds.

The wind velocities at the mountain peak in Case G1 are very small (not shown), which is very different from those in Case F1 in the effects of nonlinearity. In other words, the topography in Case G1 is so steep that the air parcels cannot pass over it. Hence, the vertical disturbances are dominated by the evanescent waves as shown in Figure 3.15a. The topography in Case G1 is so high and steep that the flow belongs to the *flow-around regime*. The patterns of vertical velocity and the disturbances of potential temperature are similar to but slightly more slantwise than that in Case D3 (U = -5ms^{-1}, Fr = 0.33). Cases G2 and G3 belong to the *flow-over regime*. In fact, the vertical cross sections in these three cases imply that the steeper the topography, the more perpendicular the vertically propagating gravity waves.

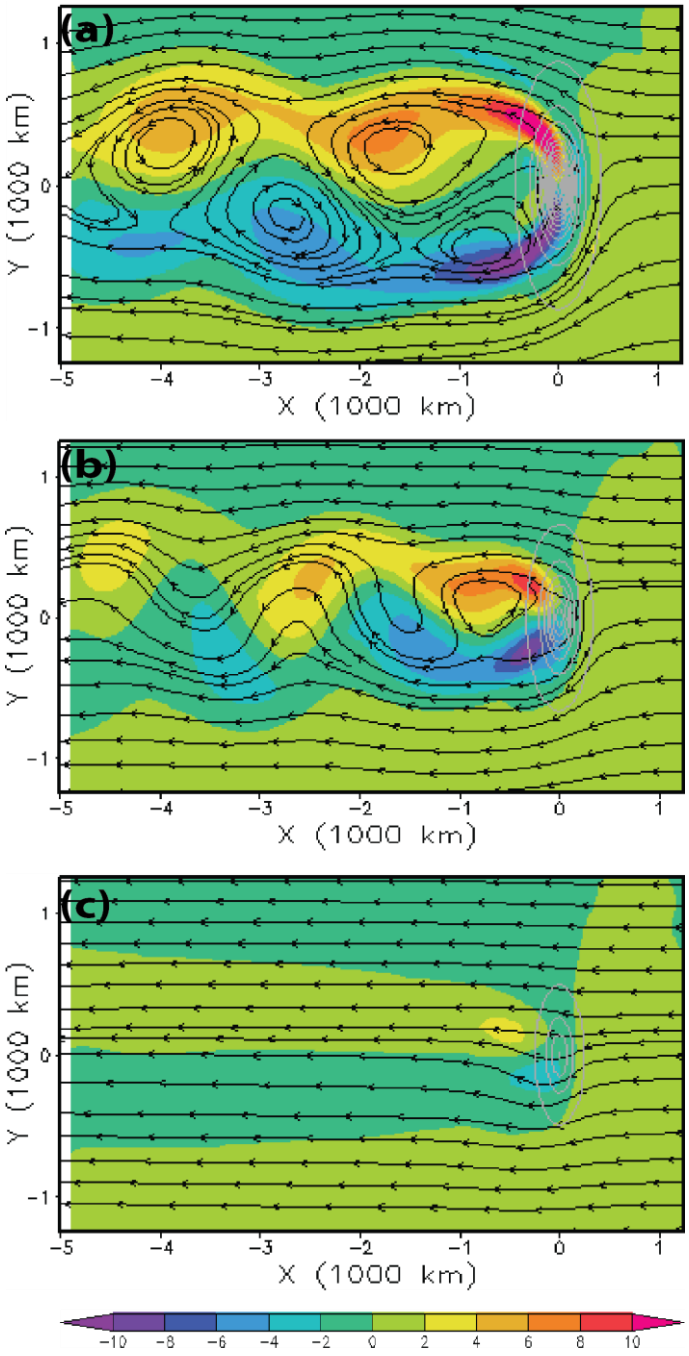

Figure 3.14. Simulated vorticity (10^{-5} s^{-1}) and streamlines on a β-plane centered at 10°N after simulation at nondimensional time $\hat{t}$ = 46.08 for (a) Case G1: h_0/a = 0.047 (h_0 = 7000 m, Fr = 0.14) (b) Case G2: h_0/a = 0.023 (h_0 = 3500 m, Fr = 0.29) (c) Case G3: h_0/a = 0.017 (h_0 = 1750 m, Fr = 0.57). U = -10 ms^{-1} and N = 0.01 s^{-1} as in the control case. The topography contour interval is 500 m.

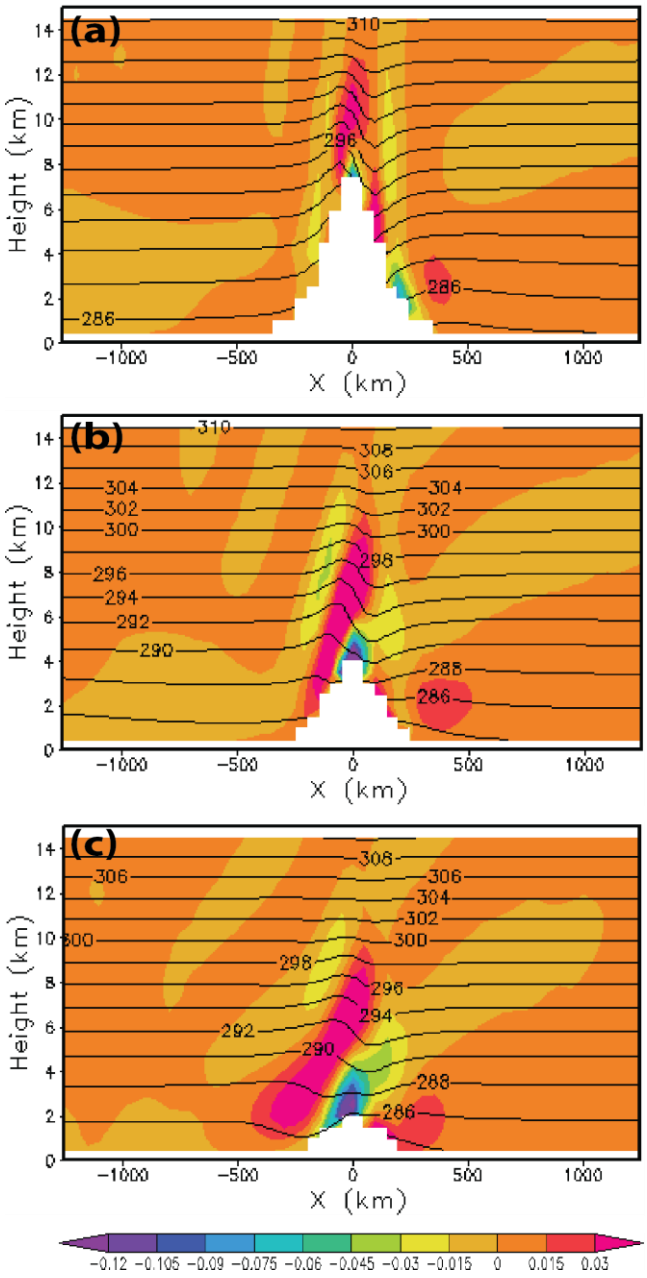

Figure 3.15. Same as Figure 3.14 (Cases G1-G3) except for the vertical cross sections of vertical velocity (ms^{-1}) and potential temperature (K) along 10°N latitude.

3.3.8. Effects of Mountain Width-Length Aspect Ratio. The effects of mountain width-length aspect ratio are measured by the parameter *b/a*; at the same time the nondimensional parameters such as h_0/a, *Fr*, *Ro*, and $\hat{\beta}$ are kept constant. Specifically, meridional half-width (*b*) is the only parameter to be changed; whereas mountain height (h_0) and zonal half-width (*a*)

remain 3500 m and 150 km, respectively. There are four cases under discussion: (1) Case H1: *b/a*=4 (*b*=600 km); (2) Case H2: *b/a*=2 (*b*=300 km); (3) Case H3: *b/a*=1 (*b*=150 km); (4) Case H4: *b/a*=0.5 (*b*=75 km). The topography with a larger *b/a* parameter has stronger blocking in the horizontal direction, and thus, creates larger vorticities and meandering streamlines. Figure 3.16 demonstrates the significance of the parameter *b/a* in the generation of vortex shedding at the lee side of the mountains.

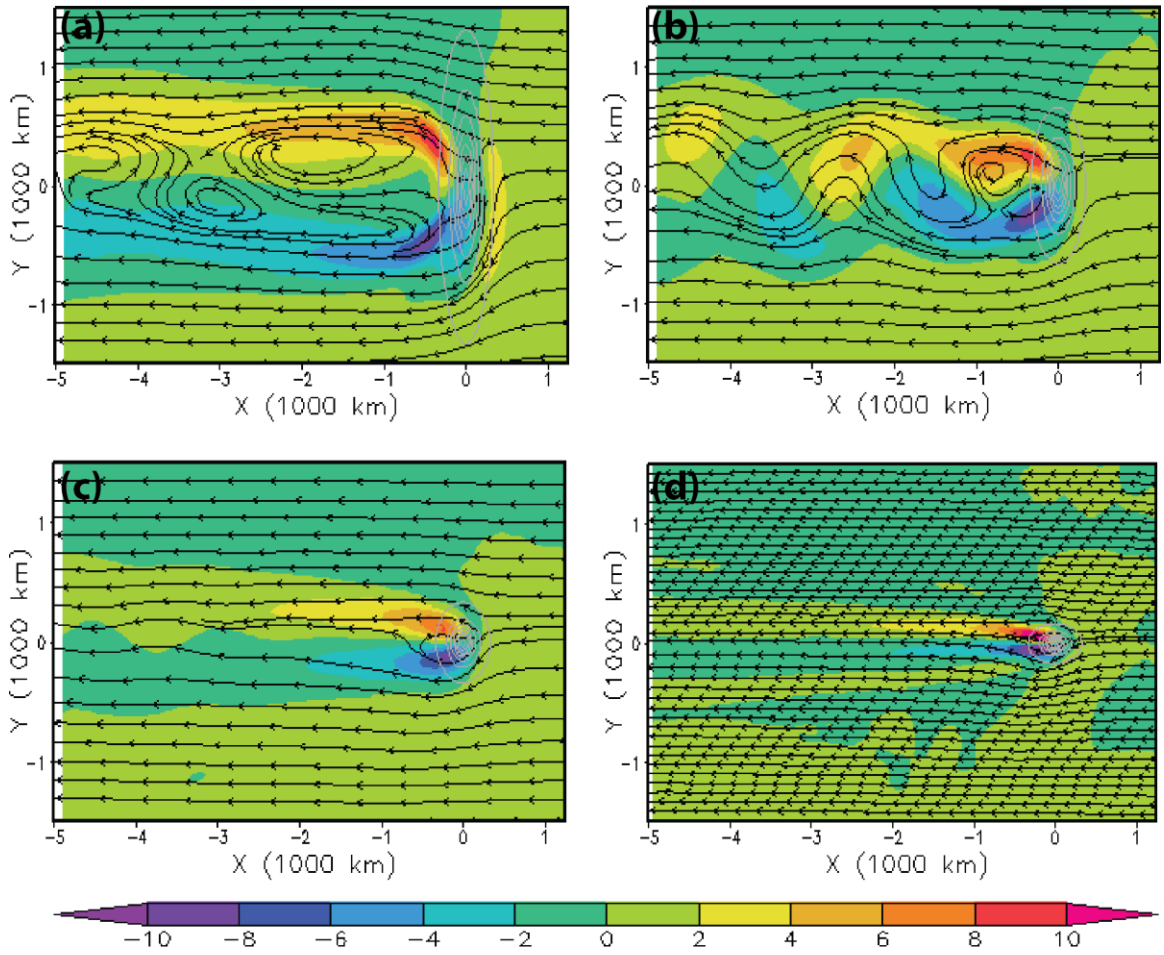

Figure 3.16. Simulated relative vorticity (10^{-5} s^{-1}) and streamlines on a β-plane centered at 10°N at nondimensional time $\hat{t}$ = 46.08 for (a) Case H1: *b/a*=4 (*b*=600 km), (b) Case H2: *b/a*=2 (*b*=300 km), (c) Case H3: *b/a*=1 (*b*=150 km), (d) Case H4: *b/a*=0.5 (*b*=75 km). In these cases *a* is 150 km as in the control case. The topography contour interval is 500 m.

The larger the parameter *b/a* is, the stronger the surface vortices, and the more wandering the streamlines become. The large blocking in the meridional direction results in large scale downslope adiabatic warming at the lee from the topography with a large b/a parameter. In contrast, small blocking in the meridional direction leads to limited downslope adiabatic warming at the lee. Therefore, surface pressure perturbation (not shown) indicates a similar tendency to that of surface vorticity and winding streamlines at the lee. In Cases H3 and H4, surface pressure perturbations are negligible, whereas Case H1 has significant negative pressure perturbations and barrier winds. Similar to the discussion on the effects of nonlinearity, in terms of surface pressure perturbations, the horizontal scale and the magnitude of downslope adiabatic warming at the lee are critical factors causing significant pressure perturbations at the lee due to the effects of the mountain width-length aspect ratio. The wind vectors (not shown) show that all four cases are subcritical flows owing to much larger wind speeds at the top of mountains than those of the incoming flows. Case H2 mimics some observed AEWs (e.g., Lin et al. 2005), which implies that these AEWs might be generated by African mountains with similar mountain steepness and relevant parameters. The orographic blocking of a mountain with a larger *b/a* parameter generates larger barrier winds, but it cannot prevent flows from going over the mountains. Actually, vertical propagating gravity waves come from flows going over mountains.

Hence, Figure 3.17 indicates that when *b/a* is larger, there are more vertical propagating mountain waves due to stronger blocking. Additionally, all four cases display characteristic tilting angle which shares a common quality with Cases F1~F3 in the effects of nonlinearity and is very different from Cases G1~G3 in the effects of mountain steepness. This implies that the tilting angle of vertically propagating gravity waves is closely related to mountain steepness.

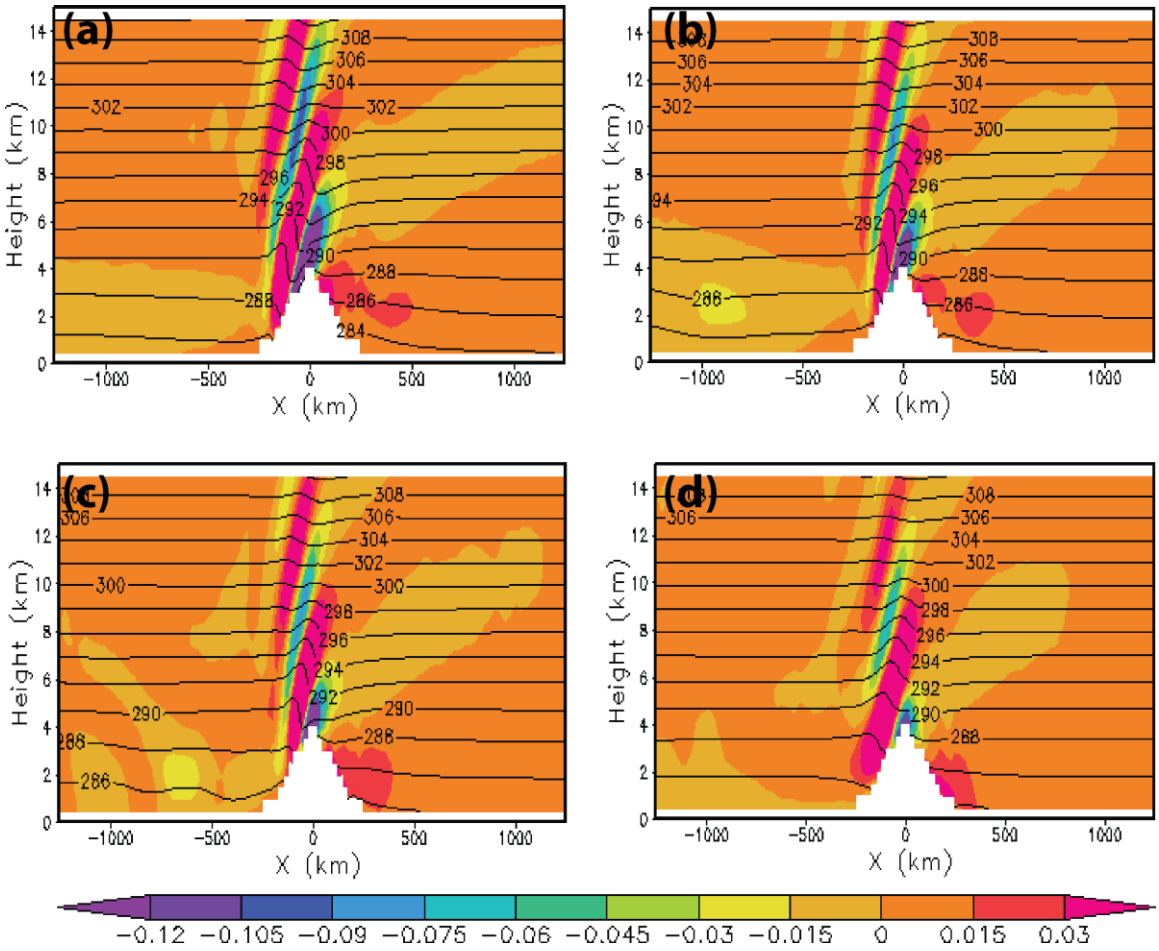

Figure 3.17. Same as Figure 3.16 (Cases H1-H3) except for the vertical cross sections of vertical velocity (ms^{-1}) and potential temperature (K) along 10°N latitude.

3.4. Conclusion

The generation of waves associated with an easterly flow over a large-scale mountain is studied with idealized simulations with dimensional parameters such as Coriolis parameter, planetary vorticity gradient (β), basic wind speed, vertical wind shear, and mountain height, length and width. Wave-like disturbances were generated at the lee side with wavelength of ~2000 km, a period of 2~3 days, and a propagating speed of ~9.6 ms^{-1}, which mimic an African easterly wave (AEW). Thus, it is proposed that AEWs may be generated by vortex shedding. The dispersion relationship of hydrostatic inertia-gravity waves on a β-plane is derived, which gives

an associating speed of about -10 ms^{-1} and which is comparable to that of 9.6 ms^{-1} in the idealized simulations and the observed speed 8 ms^{-1} in Reed et al. (1977).

Several forcings are essential in vortex shedding identified from sensitivity tests. Coriolis force is so critical that there is no lee vorticity propagating downstream without it. The β effects are important in the sustainability of lee vorticity. This infers that the waves at the lee side are Rossby waves. Both rotational effects and β effects are significant in the evolution of lee vorticity; however, the lee vorticity at 30°N is weaker than those at 10°N and 20°N. Among inertial force, flow nonlinearity, and β effects, in the first nondimensional time $\hat{t}$ = 28.8 (5 days) inertial force outweighs flow nonlinearity, and β effects in the progression of lee vorticity. However, simply with inertial force and with weak flow nonlinearity and β effects, the lee vorticity weakens after the nondimensional time $\hat{t}$ = 28.8 (5 days). Therefore, nonlinearity and/or β effects play a significant role in the sustainability of lee vorticity. Large vertical wind shear such as -2×10^{-3} s^{-1} would gradually suppress the developments of surface vorticity at the lee. As for vertical wind shears like -0.5×10^{-3} s^{-1} and -1×10^{-3} s^{-1}, the mountain-induced meridional temperature gradient and pressure gradient are not large enough to dominate streamlines and vorticities during nondimensional time $\hat{t}$ = 46.08 (8 days) and show larger lee vorticities than those in the control cases of uniform basic flow -10 ms^{-1}. The effects of vertical wind shear on lee vortices and vertical propagating gravity waves imply that the less the *Ri*, the less the lee vortices and the more vertically propagating waves are generated, because more wave energy is propagated upward instead of being advected downward. When considering mountain height, zonal half-width, and meridional half-width, large nonlinearity (small *Fr*), large mountain steepness (large h_0/a), or large mountain width-length aspect ratio (large b/a) create large

vortices; whereas the conditions of small nonlinearity (large *Fr*), small mountain steepness (small h_0/a), or small mountain width-length aspect ratio (small b/a) only generate very tiny vortices.

The flow regime of the vertically propagating disturbances is continuous and consists of both a vertically propagating mode and an evanescent mode. The vertically propagating disturbances approach a quasi-steady state in the vicinity of the mountain. Inertial force is influential in the amplitude of the vertically propagating gravity wave. But, the flow nonlinearity, and β effects are insignificant in the evolution of the vertically propagating gravity wave. In the conditions with strong uniform basic wind speed such as -20 ms^{-1} (Case D1), or large vertical wind shear such as -2×10^{-3} s^{-1} (Case E4), the vertically propagating disturbances are dominated by the vertically propagating gravity waves. In the conditions on an *f*-plane (Case B1) or without Coriolis force (Case B2), the vertically propagating disturbances are dominated by the evanescent waves. In the conditions with weak inertial force such as uniform zonal wind -5 ms^{-1} (Case D3), or large mountain steepness such as h_0/a = 0.047 (Case G1), the vertically propagating gravity waves degrade into the evanescent waves. From the vertically propagating gravity waves among the Cases F1~F3 in the effects of nonlinearity, the Cases G1~G3 in the effects of mountain steepness, and the Cases H1~H4 in the effects of mountain width-length aspect ratio, it implies that the tilting angle of vertically propagating gravity waves is closely related to mountain steepness.

CHAPTER 4

Orographic Effects on Typhoon Morakot (2009)

4.1. Statement of the Problem and Significance

Typhoon Morakot (2009) appeared as a tropical depression on August 3 2009. Then, it moved westward and made landfall in Taiwan on 23:50 LST 7 August 2009 according to Central Weather Bureau (CWB). Morakot generated record-breaking rainfall in southern Taiwan. Although there have been many observational and modeling studies of Morakot, the understanding of the structure of Morakot and orographic effects on the heavy rainfall is rather limited. Hence, there is a need to conduct further research of Morakot including storm track, sudden pressure rise, rainbands, and orographic effects on track, intensity, rainfall magnitude and distribution.

4.2. Model Description, Experiment Design, and Data

The ARW is employed to simulate Morakot in the study. It was found that numerical results are sensitive to model domains, mainly due to imperfect lateral boundary conditions. After some tests, the two-way triple-nested grid (27, 9, 3 km) is applied in the study as shown in Figure 4.1. Vertically there are 28 stretched σ levels for all the nested domains with the top at about 50 hPa and a higher resolution in the planetary boundary layer. The time intervals are 150, 50, 16.7 seconds respectively. The simulations of triple-nested grid in the study start with 00 UTC 3 August 2009 and end at 00 UTC 10 August 2009.

The physics options used in the simulations include Goddard microphysics scheme (Tao et al. 1989), Kain-Fritsch cumulus scheme (Kain 2004), Rapid Radiative Transfer Model longwave radiation physics scheme (Mlawer et al. 1997), Dudhia shortwave radiation scheme (Dudhia 1989), and Yonsei University scheme of planetary boundary layer (Hong et al. 2006).

When grid interval is less than 10 km, whether the cumulus parameterization scheme should be included in physics options is still debating in the literature. In the study, the cumulus parameterization scheme is activated in all nested domains. NCEP High Resolution Global Forecast System (GFS) 1 degree data are used as initial and boundary conditions. The NCEP daily, high-resolution, real-time, global, sea surface temperature (SST) analysis on a 0.5-degree grid (ftp://polar.ncep.noaa.gov/pub/history/sst/) is employed to update the SST during simulations. Since the intensity of tropical disturbances in GFS data is strong enough in the beginning, there is no tropical cyclone vortex initialization processes applied to the GFS data.

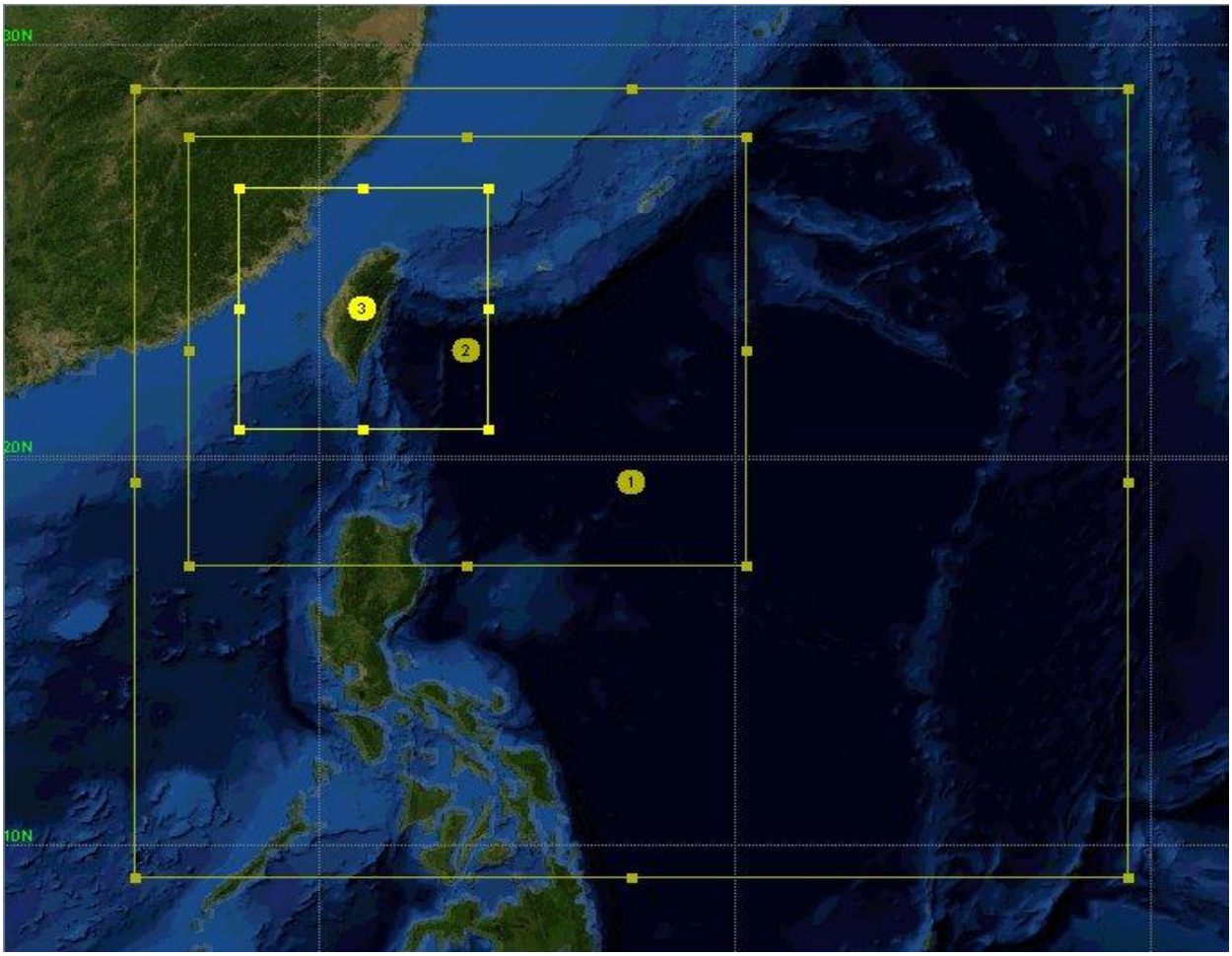

Figure 4.1. The nested domain in the simulations.

In the study we plan to explore the impacts of terrain elevation on the structure of Morakot and the precipitation associated with the passage of Morakot under large-scale circulations which are dominant. In the sensitivity experiments all the parameters are held the same as the control case (CTL) except the changes in the terrain elevation or land to ocean. The experiment of ocean replaces land over Taiwan with ocean (see Table 4.1).

Table 4.1

The control case, the experiments and the Froude numbers on 8 August on average

Experiments	**Conditions**	***U (m/s)**	***H (m)**	**Fr**
CTL	The control case	28	2715	1.0
T0.8	Terrain height is set to 0.8 original elevation	28	2171	1.3
T0.6	Terrain height is set to 0.6 original elevation	31	1629	1.9
T0.5	Terrain height is set to 0.5 original elevation	32	1357	2.3
T0.4	Terrain height is set to 0.4 original elevation	32	1086	2.9
T0.2	Terrain height is set to 0.2 original elevation	35	543	6.4
NT	Terrain elevation is set to 0	34	0	∞
OCN	Terrain is replaced by ocean	41	0	∞

* The wind speed is the mean upstream wind speed on 8 August. The terrain elevation is from CTL with 9 km resolution

The radar maximum reflectivity data are originally from the Central Weather Bureau of Taiwan. The total precipitable water imaginary data are combined by a mixing algorithm (Kidder and Jones, 2007) from three Advanced Microwave Sounding Units (AMSU) on NOAA satellites and five Special Sensor Microwave Imagers (SSMI) on the Department of Defense satellites (http://rammb.cira.colostate.edu/products/tc_realtime). The best track data from the web site http://agora.ex.nii.ac.jp/digital-typhoon/index.html.en are employed in verification and the discussion about the factors resulting in extremely heavy precipitation in Section 5b.

4.3. Verification of Simulations in the Control Case

The verification of the CTL simulation includes track, intensity, vertical maximum radar reflectivity, and accumulated precipitation. There are four radars in Taiwan which provide vertical maximum reflectivity within the ranges. Also, totally there are 404 surface weather observational and automatic stations in Taiwan, which include meteorological stations and automatically observed rainfall stations. The coverage of these stations is pretty complete in Taiwan except in the eastern mountainous regions. Hence, vertical maximum radar reflectivity and the accumulated precipitation in the analysis of observational data are the objective standards to evaluate the performance of simulations in the control case. Note that the best tracks and intensity estimated by meteorological centers such as the Joint Typhoon Warning Center (JTWC), Japan Meteorological Agency (JMA), and Central Weather Bureau (CWB) are subjective products, mainly due to limited observational data over the ocean, which raised some concerns in best track and intensity inconsistencies in the past.

In CTL, there are not many differences in the patterns physical fields between the results in different resolutions. Quantitatively, the simulation of 9 km resolution (CTL – 9 km) is the best in almost every aspect of track, intensity, maximum reflectivity, and accumulated precipitation except the maximum accumulated precipitation during 00 LST 7 August - 00 LST 8 August with 897.1 mm (9 km resolution) and 1068.6 mm (3 km resolution) compared with the observation 1003.5 mm. The simulation of CTL – 3 km is not the best could stem from high SST data and strong intensity in simulation. However, when GFS data are weak and dry on 8 August (see Figure 4.2), strong intensity in CTL in order to have a good simulation on Morakot seems to be inevitable. The intensity with two-nested grid (27, 9 km) is slightly stronger than that in

CTL – 9 km. Hence, we will discuss the results in CTL – 9 km instead of those in the two-nested grid (27, 9 km).

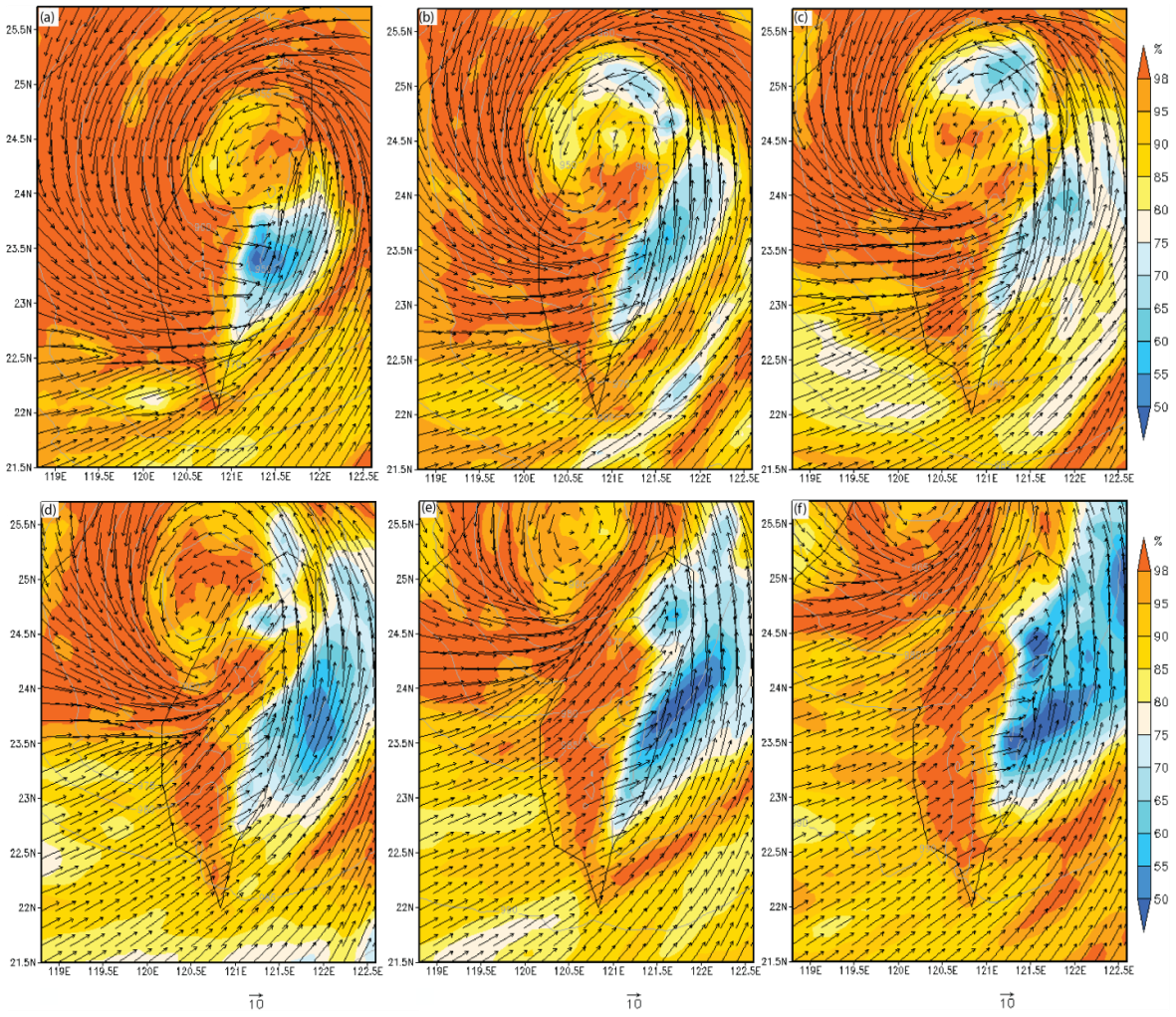

Figure 4.2. Relative humidity (shaded), and horizontal wind vector at (a) 00 UTC 8 August, (b) 06 UTC 8 August, (c) 12 UTC 8 August, (d) 18 UTC 8 August, (e) 00 UTC 9 August, and (f) 06 UTC 9 August from the CTL-9 km.

4.3.1. Track and Intensity. Environmental steering flow is a good measure for typhoon direction (Chan and Gray 1982). In the study, we calculate the steering flow by averaging the mass-weighted mean wind within a radius of 378 km between 850 and 300 hPa from the CTL. The simulated track is close to the JMA best track after 12 UTC 6 August. Thus, the

environmental steering flow since 12 UTC 6 August would be reliable. Morakot has slowed down since 12 UTC 6 August because of terrain blocking from the CMR. The steering flow decelerates and turns from southeasterly to southerly, then to southwesterly (Figure 4.3a). Note the southerly environmental steering flow before 00 UTC 8 August is consistent with the merging large-scale circulations moving northward (Hong et al. 2010). After Morakot crosses CMR, both the environmental steering flow and the propagation speed of Morakot is less than 2 m s^{-1} because of the hindrance of the steep CMR (Fig. 4.3a). Then, the environmental steering changed from southerly to southwesterly, finally resulting in Morakot's moving to northeastward (Figure 4.3a). It is suggested that the environmental steering flow indicates the change of Morakot translation.

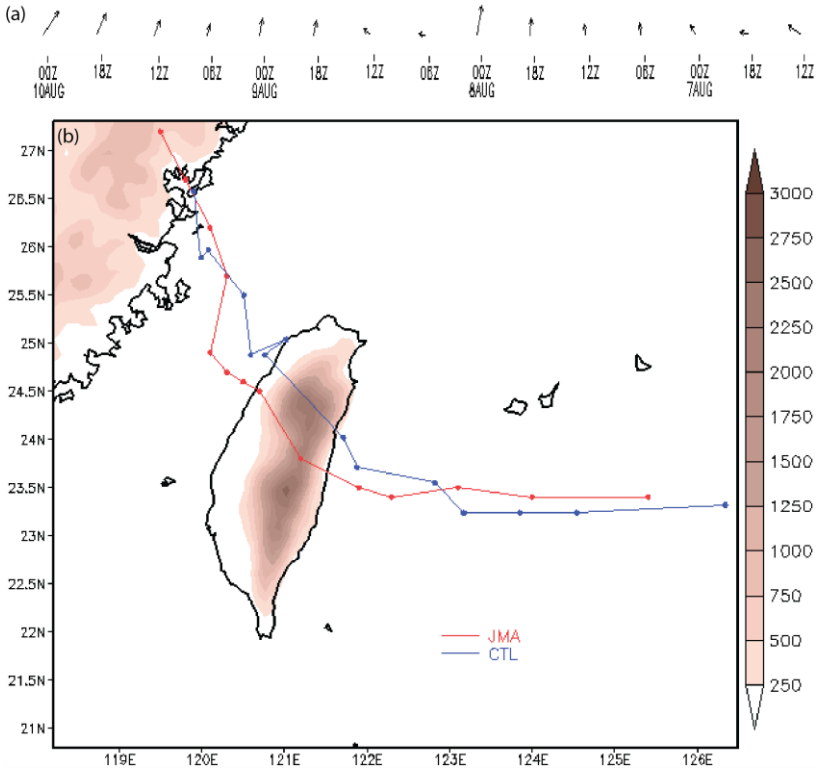

Figure 4.3. (a) The environmental steering flow from the CTL with 27 km resolution. (b) The JMA best track and the CTL track with 9 km resolution every three hours from 12 UTC 6 August to 18 UTC 9 August. The shaded colors are terrain elevations (meter).

The minimum sea level pressure from JTWC is much higher than those from JMA and CWB. We were unable to obtain maximum wind speed data online from CWB. Hence, we will compare the track and intensity in the simulation with those from JMA. Figure 4.3b displays the JMA best track and the CTL-9 km during 00 UTC 7 August - 18 UTC 9 August 2009. The average deviation is 74.64 km and the root mean square of deviation is 80.58 km. The simulated movements fall behind JMA best track before 06 UTC 8 August 2009 and are pretty close to JMA best track since then until 12 UTC 9 August 2009 (Figure 4.3b). Comparing with the JMA maximum wind speed, in general the intensity in the CTL-9 km shows a slow spinup during the first four days and larger intensity than that of JMA data in the last three days (Figures 4.4a and 4.4b). The largest simulated maximum wind speed (41 m s^{-1}) before the landfall is stronger than that of JMA (39 m s^{-1}). After the landfall, the trends of weakening intensity in JMA and the simulation are not much different from each other, and thus, the intensity in simulation is larger than that in JMA data on 8 and 9 August (Figure 4.4). Simulated minimum sea level pressure demonstrates apparently stronger intensity than JMA data since 00 UTC 7 August (Figure 4.4b). However, when the initial data are weak after Morakot develops and dry (see Figure 4.2), a strong intensity, which stems from both high SST (see Figure 4.5) and numerical schemes as well as compensates the shortcoming of the initial data in order to obtain good simulations, is inevitable.

In summary, the simulation is able to capture the right track especially on 8 and 9 August 2009, a critical period for producing extremely heavy rainfall. This, in turn, produces the right rainfall patterns on subsection accumulated precipitation, albeit the drawbacks in over-prediction of the intensity.

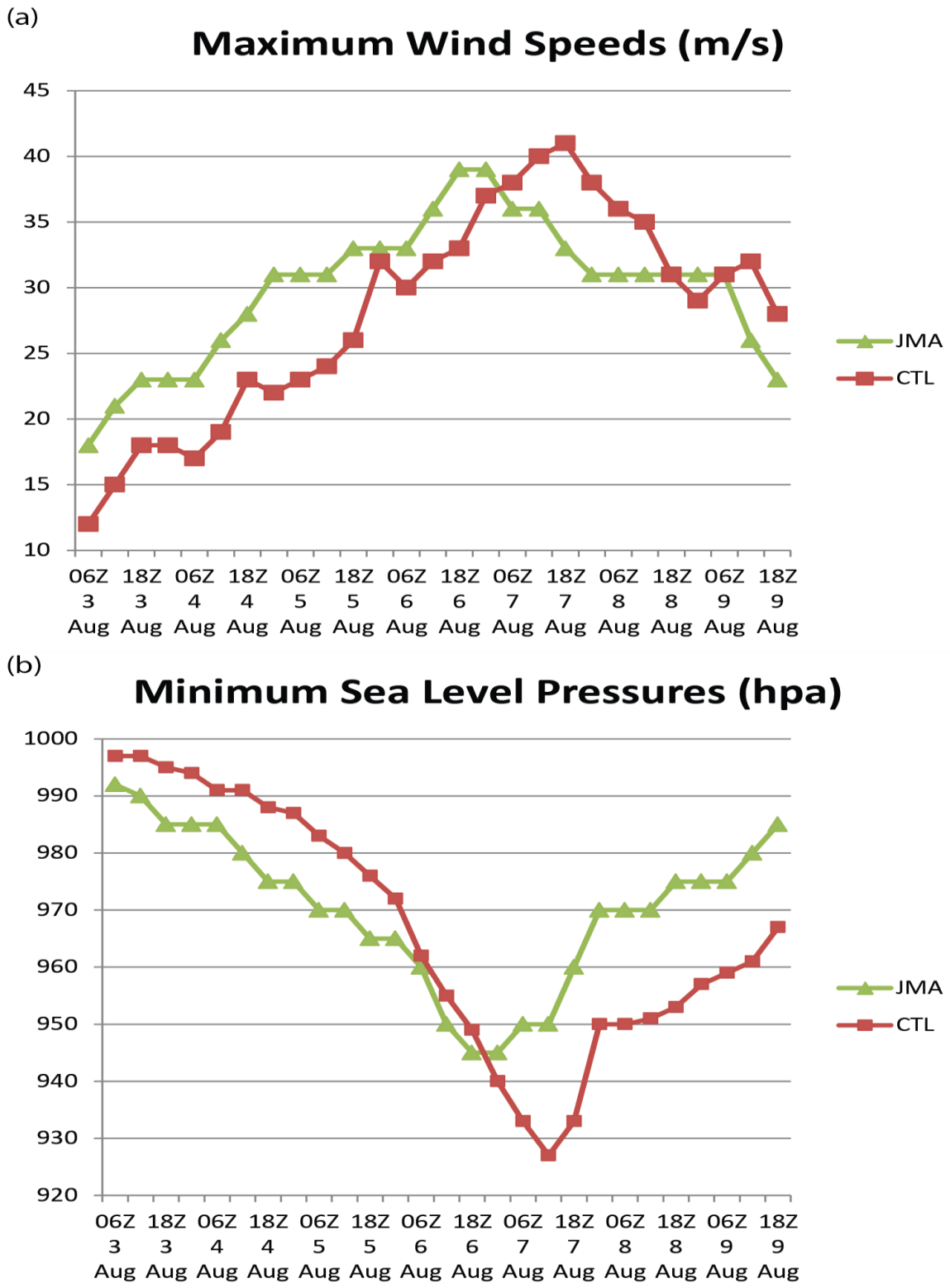

Figure 4.4. (a) Maximum surface wind speed and (b) minimum sea level pressure from JMA analysis and the CTL-9 km case. The time of landfall in simulation is at about 21 UTC 7 August.

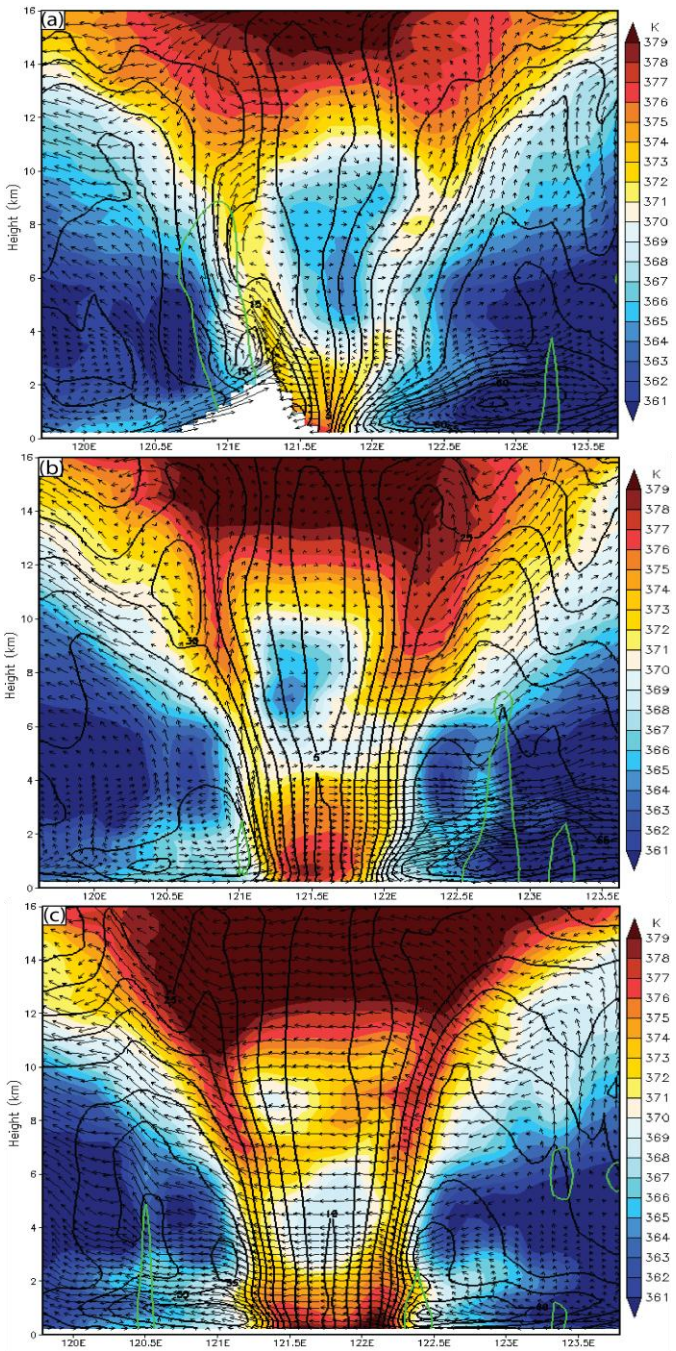

Figure 4.5. The longitude-height cross section of the wind vectors and wind speed contours (black) with interval 5 ms^{-1}, the equivalent potential temperature (shaded), and maximum reflectivity (40 dBZ) (green) of Morakot on (a) 22 UTC 7 August at 23.94°N in the CTL-9 km case, and 21 UTC 7 August in the experiments of (b) case NT at 23.94°N and (c) case OCN at 24.26°N.

4.3.2. Maximum Vertical Reflectivity and Accumulated Precipitation. The comparison of the simulated maximum vertical reflectivity and observed radar reflectivity composite is shown in Figure 4.6. The former includes rain, snow, and graupel, only accounts for the Rayleigh scattering range of drop sizes, and assumes particles to be spheres of constant density and exponential distribution of size distribution. The intercept parameters for rain are constant (Reisner et al. 1998); whereas the intercept parameter for snow is a temperature-dependent value as described in Thompson et al. (2004). At 00 UTC 8 August the center of Morakot is over the island of Taiwan. The major reflectivity pattern in observed radar reflectivity composite is located to the south of Morakot and extends toward east and northeast. Qualitatively pattern of the simulated maximum reflectivity is similar to that of the observed radar reflectivity composite which has the strongest rain band to the south of Morakot center.

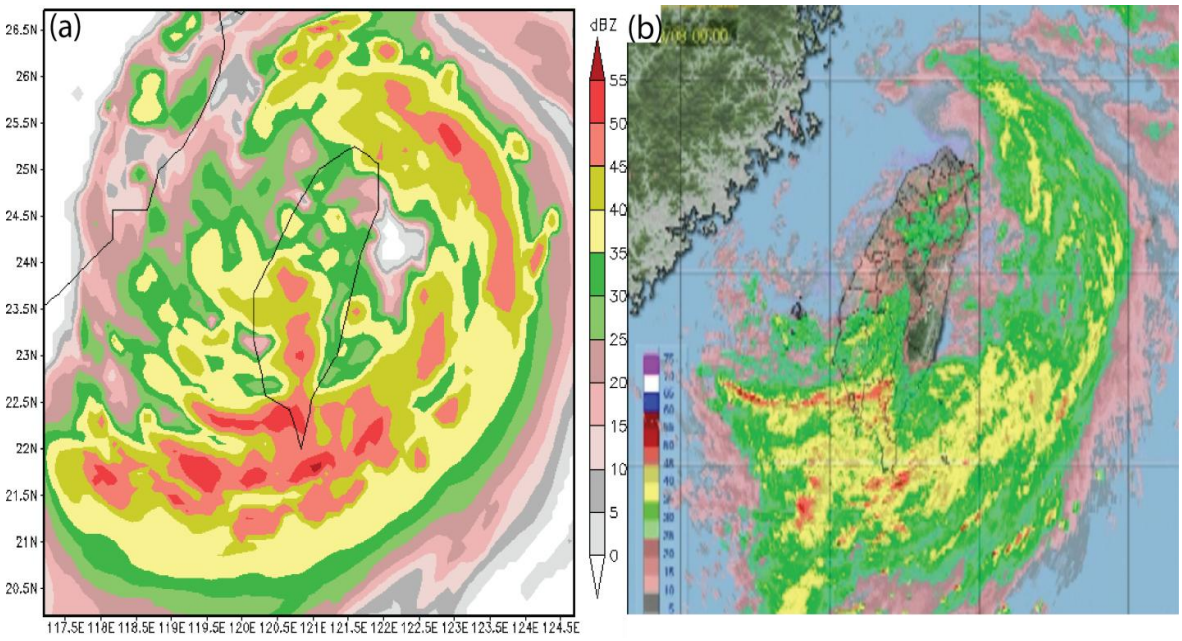

Figure 4.6. (a) Maximum reflectivity from the case CTL-9 km at 02 UTC 8 August and (b) maximum radar reflectivity at 00 UTC 8 August.

Furthermore, the observed rainfall data is analyzed based on Cressman objective analysis technique in order to compare the patterns and rainfall of the CTL case in model simulation with the observational precipitation analysis. Figure 4.7 compares the simulated rainfall during 00 LST 3 August – 00 LST 10 August 2009 where the LST (= UTC + 8 hours) stands for local standard time. The simulated accumulated precipitation captures the rainfall patterns of the analysis of rain gauge data. In particular, the location of simulated maximum accumulated rainfall of the inner domain with grid resolution of 9 km is only less than 6.6 km away from the station with rainfall maximum in the observational data. Overall the simulated rainfall catches the patterns in observational rainfall data and is higher than observed rainfall. The maximum simulated rainfall is 3208 mm, which is about 12.5 % higher than the observed value due to strong intensity. Due to strong variation with time, comparison of daily rainfall is more rigorous compared to the comparison of the entire simulated period.

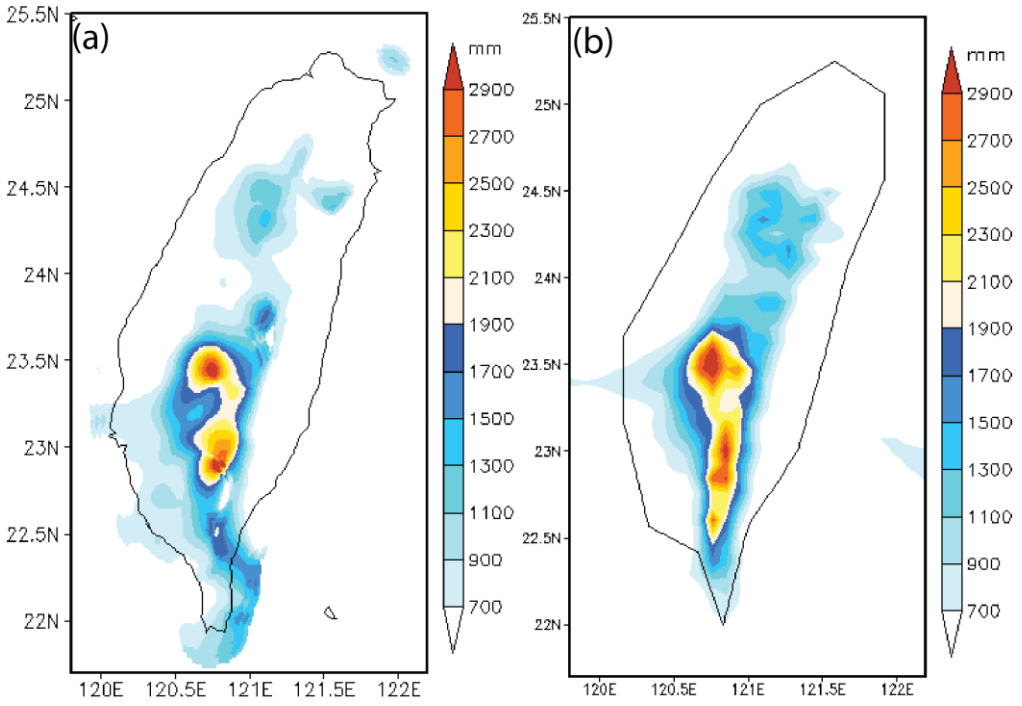

Figure 4.7. The accumulated rainfall over Taiwan during 00 LST (local standard time) 3 August - 00 8 August from (a) observation and (b) the CTL-9 km.

Figure 4.8 is the comparison of daily rainfall on 7, 8, and 9 August 2009 in local time. Basically, the daily rainfall patterns in observational data are well simulated. The elongated pattern of the simulated extremely heavy precipitation in southern Taiwan is orographically induced and originated from the strong wind associated with the simulated strong intensity of the typhoon. The simulated maximum accumulated rainfalls in these three days are 897.1 mm, 1779.7 mm, and 1236.5 mm, respectively, which are overpredicted about -10.6%, 26.9%, and 6.1% more than the values in observational data, respectively.

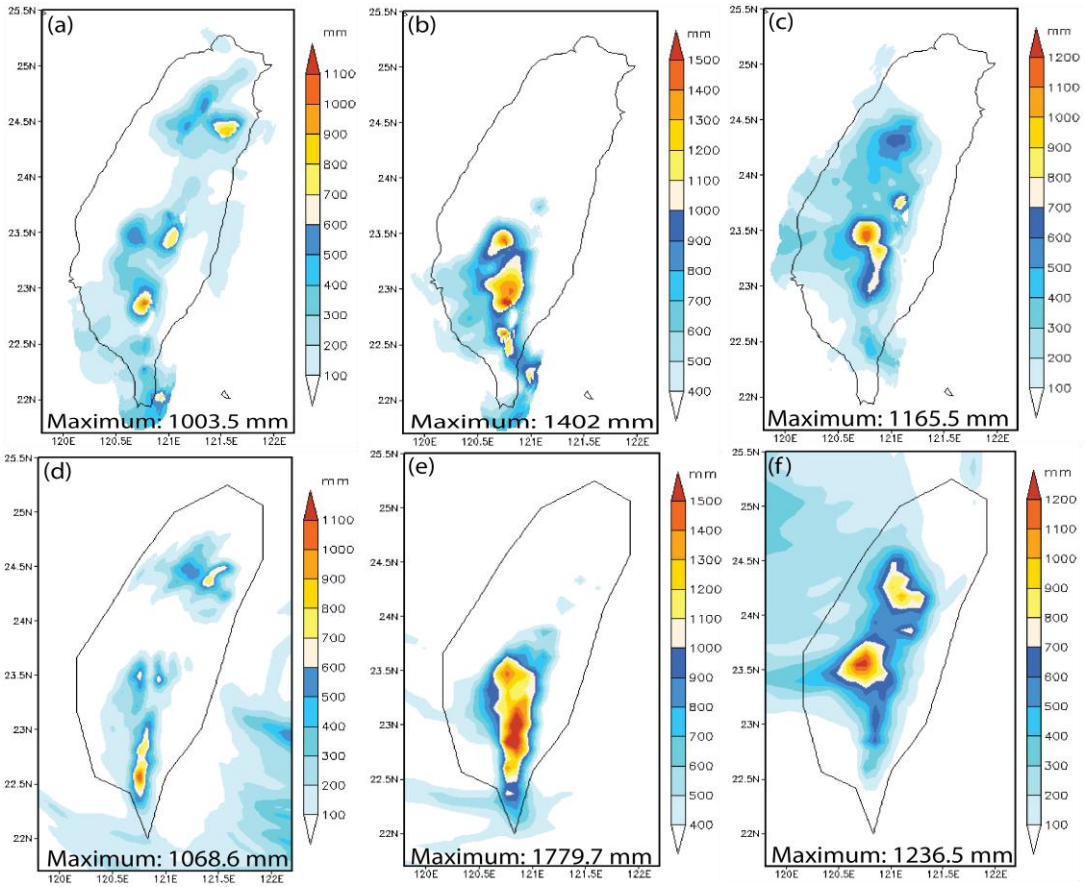

Figure 4.8. The accumulated rainfall over Taiwan from (upper) observation and (lower) the CTL-9 km during 00 LST 7 August - 00 LST 8 August (a)(d), 00 LST 8 August - 00 LST 9 August (b)(e), 00 LST 9 August - 00 LST 10 August (c)(f), with resolutions of (d) 3 km, (e) 9 km, and (f) 9 km.

The simulated total and daily rainfall patterns demonstrate excellent performance of the simulation in spite of the minor drawback in the overprediction of quantitative precipitation. The track in the simulation is then justified in illustrating the reasons resulting in extremely heavy precipitation during the passage of Morakot over Taiwan.

4.4. Orographic and Land Effects on the 3D Structure of Morakot (2009)

One major object of this study is to investigate the orographic and land effects on the time evolution of the three-dimensional structure of Morakot. Especially, we would like to focus on the reflectivity, wind, and equivalent potential temperature (θ_e) fields in three stages: over the ocean, during landfall, and after landfall but moved to northern Taiwan. The largest reflectivity of Morakot over the ocean is to the south of the eye; while the minimum is to the north of the eye. The reflectivity to the east roughly is equal to that to the west (Figure 4.9). These reflectivity patterns do not change much until the Morakot circulation is affected by the CMR (Figure 4.10a). Because the CMR is so high and steep, the Morakot circulation are strongly influenced and the transportation of water vapor are blocked; and thus, the reflectivity to the west of the eye (lee side of the CMR) is no longer equal to that to the east (Figure 4.10a) as well as orographically induced rain is pronounced since then. The diameter of the eye near the low boundary is about 0.7 degree width in longitude at 23.55°N (Figure 4.9). In fact, the eye is gradually smaller and smaller since 00 UTC 7 August, then less visible after landfall (Figures 4.9 and 4.10a). Within two hours after landfall the cloud-free eye disappeared.

The longitude-height cross section of Morakot on 12 UTC 7 August demonstrates some typical characteristics of a tropical cyclone as shown in Figure 4.8. The largest wind speed is near the height of 1 km, the top of the marine boundary layer (MBL) (Figure 4.11a). The radius of maximum wind (RMW) increases with height (Figure 4.11a). The secondary circulation at the

eye wall is only inward in low levels, and then upward within the eye, but, the outward flow in high levels is not very clear (Figure 4.11a). The maximum upward velocity is larger than 1.5 m s^{-1} located at about 1.5 km height; and the maximum downward velocity is larger than 0.5 m s^{-1} around the upward velocity (Figure 4.11b). There is a wide region with low θ_e (θ_e<365 K) within the eye (Figure 4.11b). This implies that the upward motion is not strong enough everywhere in the eye wall to prevent low θ_e air from going into the region within the eye wall. The minimum wind speed is at about 10.5 km height around the center of the eye (Figure 4.11a). In the longitudinal direction rain bands don't extend to the distance (Figure 4.11b). In the eye wall there is a large upward motion associated with deep convection; the upward motion elsewhere are rather weak (Figure 4.11b). The large equivalent potential temperature (θ_e >376 K) is within the eye wall; whereas the lowest θ_e (θ_e <352 K) is at the sides about 1-4 km height (Figure 4.11b).

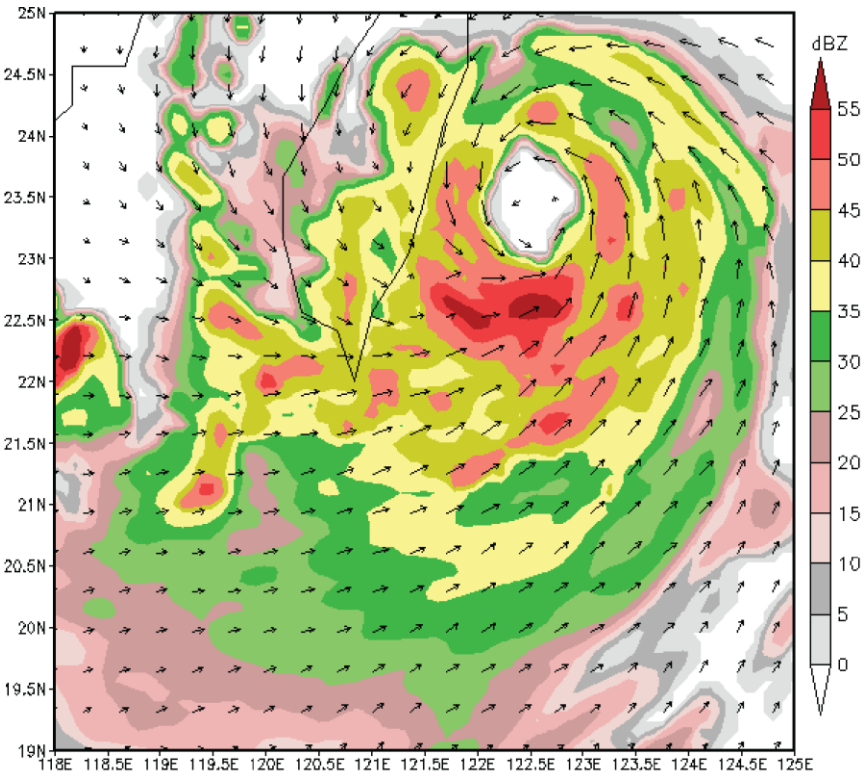

Figure 4.9. The maximum reflectivity and wind vectors on 12 UTC 7 August in the CTL-9 km case.

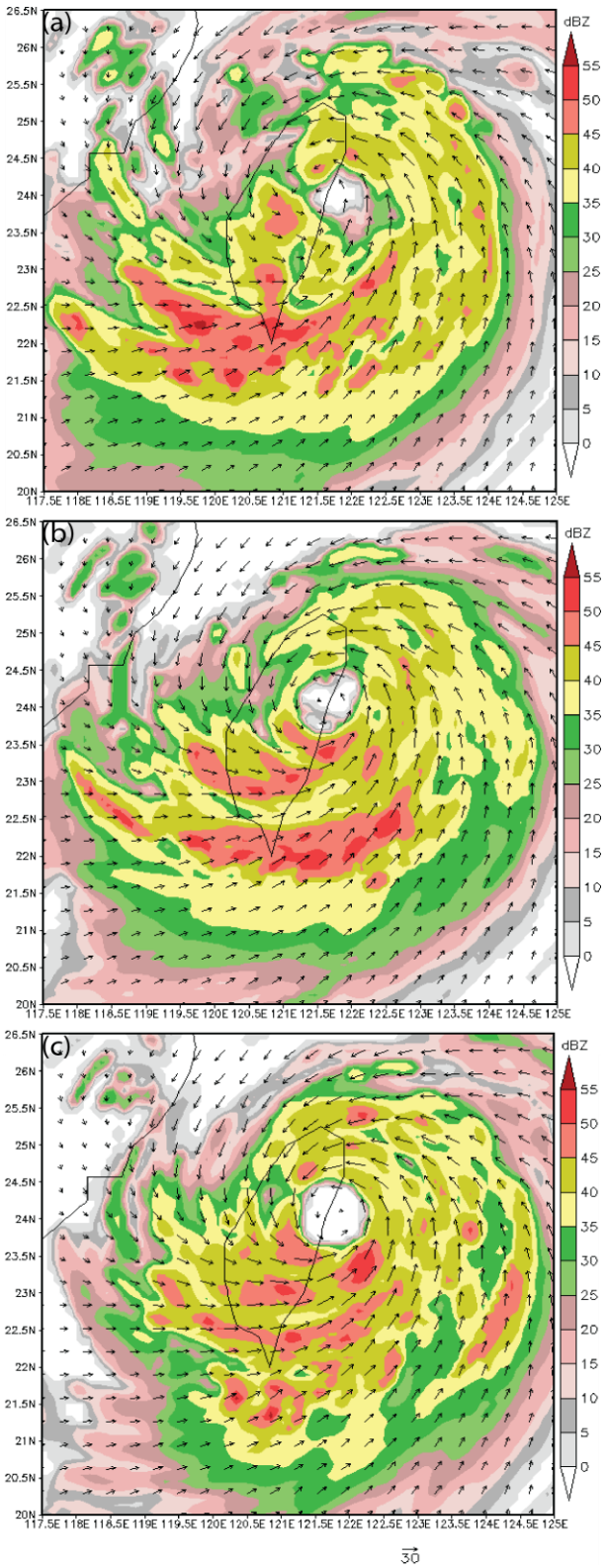

Figure 4.10. The maximum reflectivity on (a) 22 UTC 7 August in the CTL-9 km case, and 21 UTC 7 August in the experiments of (b) no terrain (NT) case and (c) ocean (OCN) case.

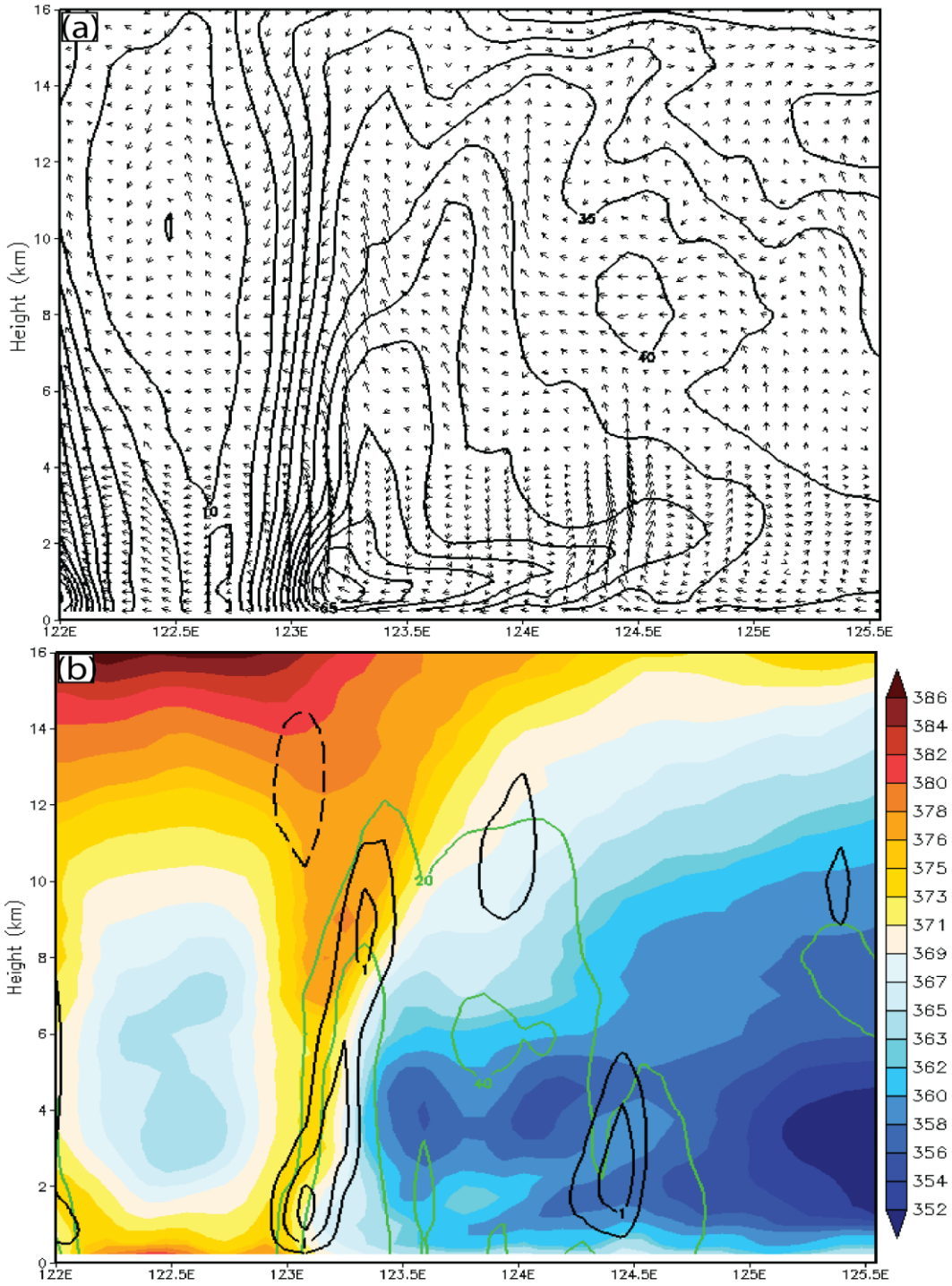

Figure 4.11. The longitude-height cross section at 23.55°N of (a) the wind vectors and wind speed contours with interval 5 ms^{-1} and (b) the equivalent potential temperature (K) (shaded), maximum reflectivity (green), and vertical velocity (black) with interval 0.5 ms^{-1} of Morakot on 12 UTC 7 August in the CTL-9 km case.

In the stage of landfalling, Figure 4.9 shows the differences in the wind and the maximum reflectivity fields between the CTL case and the experiments of no terrain (NT) and ocean (OCN) when the storm just made landfall. The difference in timing between the CTL case and the cases of NT and OCN is because the storm slows down in the CTL case due to orographic blocking. The distributions of large reflectivity (>25 dBZ) in the cases of NT and OCN are different from those in the CTL case. Again, the orographic blocking effects in the CTL case are so significant that there is no maximum reflectivity around the eye wall. Instead, the maxima are in the mountainous regions extending southward. Therefore, orographically induced rainfall and its associated reflectivity are very important in the CTL case. The reflectivity maxima in the cases of NT and OCN remain around the southern part of the eye wall extending southward. In addition, the eye in the OCN is much larger than that in the other two cases which indicates the significant of ocean on the development of a typhoon.

In the longitude-height cross section of Morakot simulated in the CTL case, the second circulation close to the shore is much more distinct than that above the ocean with the help of deep convection in the windward (west) side of the CMR. The maximum wind speed above the ocean is still near the MBL; and the one close to the shore is not very clear over the Taiwan Strait. The high-θ_e (>372 K) area in the eye wall close to the ocean is separated by medium-value θ_e (369 K) air. The transport of medium-value θ_e by the anticyclonic flow on x-z coordinate tends to separate low-θ_e air about 2 km height above the ocean (Figure 2a). In case NT, close to the shore the secondary circulation of inward in low levels, then upward within the eye, and the outward flow in high levels is rather lucid; whereas, there is no distinct secondary circulation above the ocean, and thus, the high-θ_e area in the eye wall at that side is separated by medium-valueθ_e (371K) air (Figure 2b). The convections on land close to the eye wall help form the secondary

circulation; but the deep convections above ocean deflect inflow at lower levels. Also, in this stage the storm has not yet developed very well in case OCN. Hence, the secondary circulation is not clear because of either the detracking deep convections close to the west or weak convections to the east (Figure 4.2c). The RMW lifted to a higher level is rather apparent. The high-θ_e area close to low boundary within the eye shows the impacts of high SST (Figure 4.2c).

In the stage of being in northern Taiwan, a comparison of the vertical structure between the CTL, NT, and OCN cases on 03 UTC 8 August is shown in Figure 4.12. In the CTL case, the secondary circulation at the eye wall of inward in low levels, then upward within the eye wall, and outward flow in high levels no longer exists. The maximum wind speeds are still at about 1 km height. But the outward tilting RMW with height also no longer exist. The high-θ_e region (>371 K) is only limit to above 7 km; whereas the low-θ_e air (<364 K) is connected from one side to the other at about 5 km height (Figure 4.12a). The above indicates that the eye wall has collapsed which can be attributed to the effects of the steep and high CMR on Morakot circulation. In case NT, the secondary circulation and outward tilting RMW with height are not as clear as previous stages. The high-θ_e region (>371 K) extend to low levels in an irregular pattern (Figure 4.12b). All the above indicate that the eye wall is decaying in both cases CTL and NT, and that ocean is of importance on sustaining the typhoon. In contrast, in case OCN, the secondary circulation and outward tilting RMW with height to the west are obvious (Figure 4.12c) because the storm is still developing due to the additional water vapor, latent heat and sensible heat from the lower boundary of ocean.

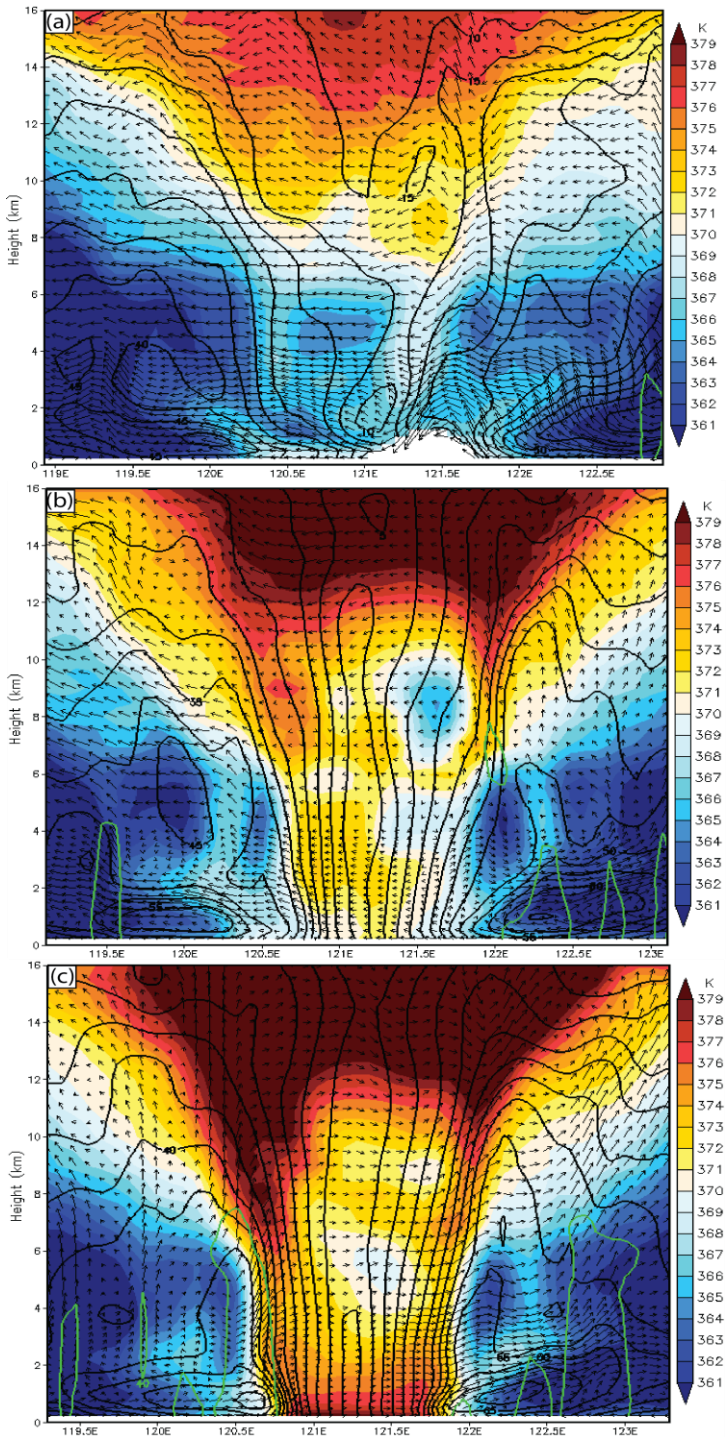

Figure 4.12. The longitude-height cross section of the wind vectors and wind speed contours (black) with interval 5 ms^{-1}, the equivalent potential temperature (shaded), and maximum reflectivity (40 dBZ) (green) of Morakot on 03 UTC 8 August in (a) case CTL-9 km at 24.73°N, and the experiments of (b) case NT at 24.41°N and (c) case OCN at 24.18°N.

In this section we demonstrated that the eye, eye wall, high-θ_e region within the eye wall, secondary circulation, and tilting RMW of Morakot are closely associated with the development of the storm, especially the deep convections around the eye wall. Over ocean the storm can develop continuously as in case OCN. Hence, the second circulation is more obvious than that in the CTL case (Figs. 4.11a and 4.12c). Over land the eye, eye wall, high-θ_e region in the eye wall, secondary circulation, and tilting RMW of Morakot are decaying (Figures 4.5 and Figures 4.9–4.12), particularly those in the CTL case with high and steep terrain. Based on these experiments, the presence of land is much more substantial than terrain elevation for the development of Morakot. How do sensible heat, latent heat, and water vapor make impacts on the developments of Morakot is an important issue to be further investigated.

4.5. Factors Leading to Extremely Heavy Precipitation

4.5.1. Major Mechanisms Leading to Strong Upward Motion. Several mechanisms can generate strong upward motion such as orographic lifting, convergence, and instabilities. Instability here includes moist absolute instability, conditional instability, and potential instability. When Morakot slowly moved northward after crossing CMR, accordingly the regions of convergence and/or orographically induced rainfall moved northward, and thus, brought about apparently heavy precipitation in Northern Taiwan on August 9. In the study we would like to identify the major mechanisms led to strong upward motion, especially for 00-24 UTC 8 August during which there is 1503.5 mm rainfall observed at the station located at (23.51°N, 120.81°E). Therefore, we inspect the nearest vertical cross sections at (23.55°N, 120.76°E) which has a maximum precipitation of 1835.9 mm in the CTL-9 km case and at (23.55°N, 120.67°E) which has precipitation of 740.2 mm in the case NT during the period. The major mechanism will be inferred by analyzing the simulated data causing extremely heavy rainfall in cases CTL and NT.

The extremely heavy precipitation was mainly resulted from the convergence produced by Morakot's outer circulation and southwesterly, orographic lifting, and instabilities. Special attention is paid to a region with a diameter at least 0.5 degree in the vicinity of the Morakot center, where the wind speed, convergence, and upward motion are much weaker, and less humid than those to the south of Morakot center where orographic lifting and convergence between Morakot circulation and southwesterly monsoonal flow occurred and led to heavy rainfall (Figures 12a and 2a-2d). Close to Morakot center it is relatively dry because of the blocking of the CMR on water vapor transportation (Figure 4.10a) and the advection of very dry air to the east of the CMR due to adiabatic warming (Figures 4.2a, 4.2b, and 4.2c). The weak wind speed, convergence, and upward motion as well as low relative humidity close to Morakot center are consistent with the lack of deep convection in Figure 4.12a. Away from Morakot center to the south the strong wind, high humidity and convergence of Morakot outer circulation and southwesterly monsoonal flow help lead to orographic lifting to produce extremely heavy precipitation (Figure 4.2 and Figure 13). This is the main reason why the rainfall distribution was quite asymmetric and heavy precipitation mostly happened in southern Taiwan when Morakot passed northern Taiwan. The regions with strong flow convergence and orographic lifting moved northward accordingly as Morakot moved northward, and thus, led to heavy precipitation in northern Taiwan on 9 August (Figures 2e and 2f). The much drier southwesterly in GFS data could be the reason why the accumulated precipitation in the CTL case underpredicts the precipitation as Morakot moved away from Taiwan during 00 UTC 9 August – 00 UTC 10 August (Figures 2a-f). Of interesting is the very dry regions to the east of the CMR caused by adiabatic warming associated with strong downslope wind (Figures 2a-f).

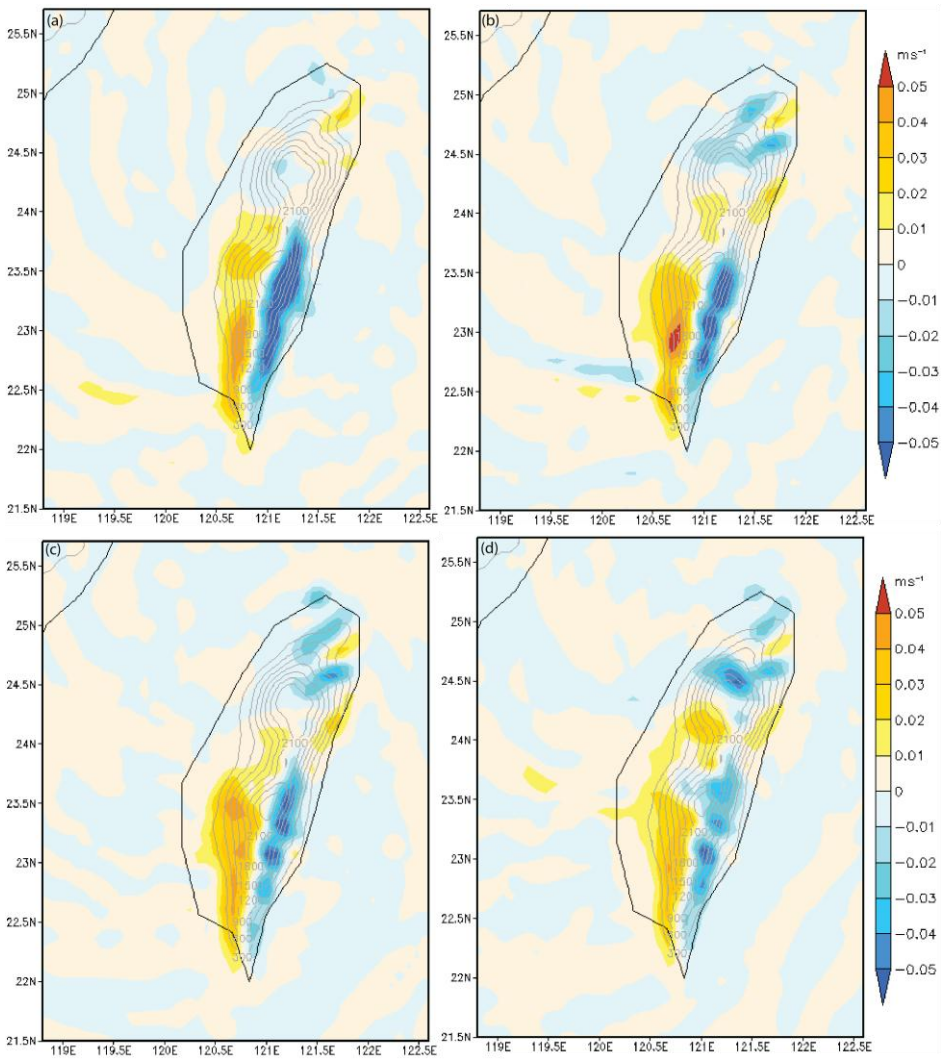

Figure 4.13. The orographically induced vertical specific humidity flux at (a) 00, (b) 06, (c) 12, and (d) 18 UTC 8 August from the CTL-9 km. Grey lines are topography contours.

Concerning the orographic lifting, the low-level upward motion associated with flow over mountain may come from orography or environment, thus the vertical velocity can be divided and expressed as in Eq. (1), similar to that proposed in the ingredient approach of orographic rain (Lin et al. 2001, Lin 2007). However, frequently w_{oro} and w_{env} cannot be separate completely due to nonlinear interactions. In order to separate them completely, w_{oro} is calculated by subtracting the vertical velocity in the case NT from that of case CTL as shown below in Eq. (2).

$$w = w_{oro} + w_{env} = V_H \cdot \nabla h + w_{env} \quad (1)$$

$$w_{oro} = w - w_{env} = w_{CTL} - w_{NT} \quad (2)$$

Because the vertical velocity in the case NT is so much smaller than that in case CTL, the orographically induced vertical velocity fields (Figure 4.13) are reasonable despite the fact that the tracks in the CTL and NT cases are not exactly the same. The elongated region of strong upward motion is overpredicted, as discussed in the model verification in Section 3. Nevertheless, still the orographically induced vertical motion plays an important role in leading to extremely heavy precipitation on 8 August.

The positive values (shaded regions in orange or yellow colors) of environmental lapse rate minus moist adiabatic lapse rate and the very high relative humidity (>98%, the region within contours) (Figure 4.14a) (Lin 2007) along with the skew T plots (Figure 4.15a) during 09 UTC 6 August – 03 UTC 8 August indicate that there are plenty of opportunities to have moist absolute instability occurred during the period. In fact, the moist absolute instability could occur in 9 August although the convective available potential energy (CAPE) is much smaller than that during the previous period. The vertical gradient of saturated equivalent potential temperature ($\partial\theta_e^*/\partial z$) was negative (below shaded regions in dark blue colors above surface) every day between 00 UTC 3 August and 00 UTC 10 August (Figure 4.16a). The lifting condensation levels (LCLs) are generally low except during the period of 03 - 12 UTC 8 August. When the strong wind associated with the approaching Morakot occurred during 7 – 9 August, conditional instability might be triggered. In addition, the vertical gradients of equivalent potential temperature ($\partial\theta_e/\partial z$) are negative (below shaded regions in dark blue colors above surface) almost every day between 00 UTC 3 August and 00 UTC 10 August (Figure 4.17a). The strong

wind during 7 – 9 August might be able to lift the full layer of atmosphere ahead of the mountain thus triggered the potential instability. Hence, instabilities, including moist absolute instability, conditional instability, and potential instability, appeared to be able to generate strong upward motion which may help lead to extremely heavy precipitation at (23.55°N, 120.76°E).

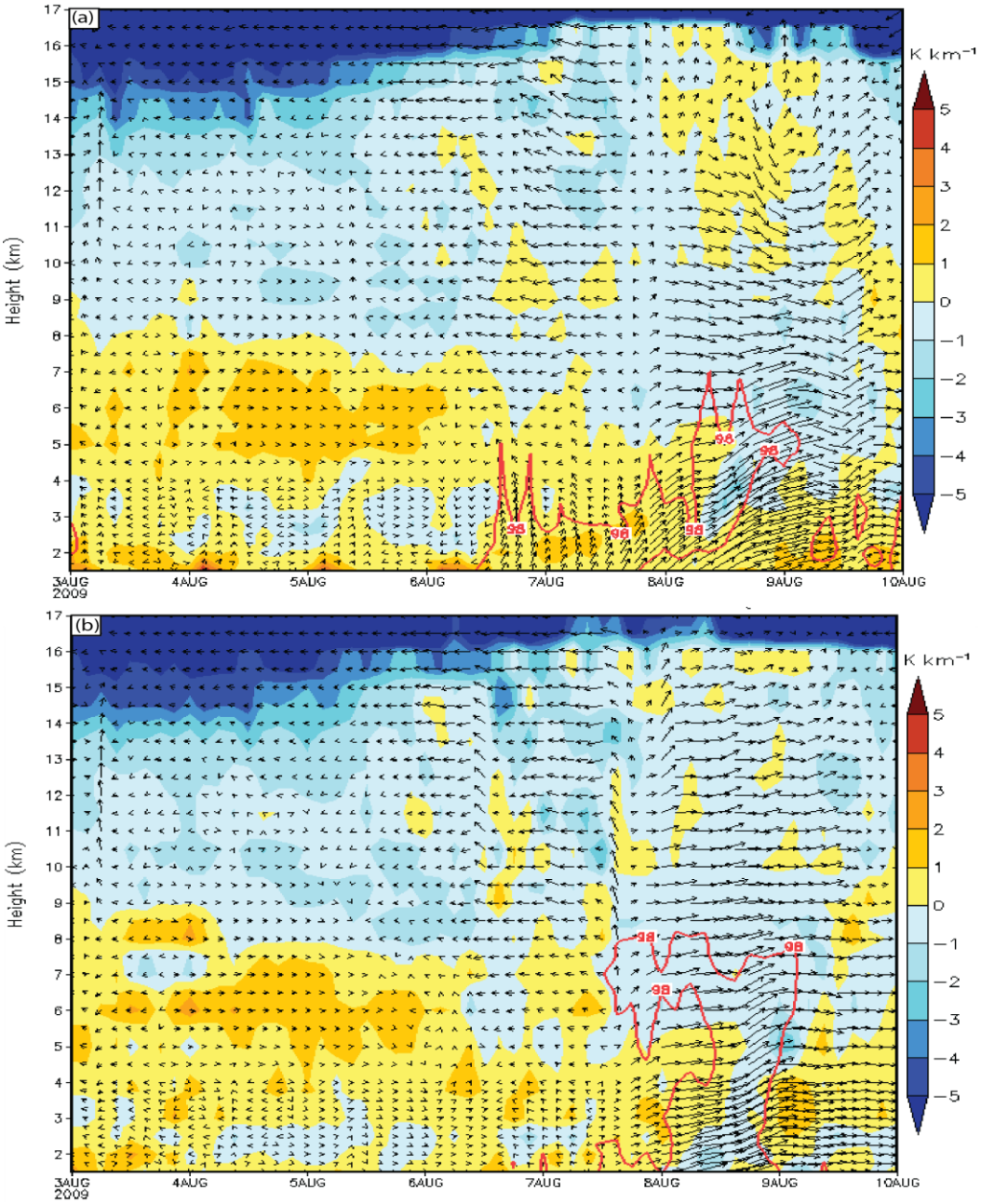

Figure 4.14. The time-height cross section of the environmental lapse rate minus moist adiabatic lapse rate for (a) case CTL-9 km and (b) case NT. Red lines are 98% relative humidity.

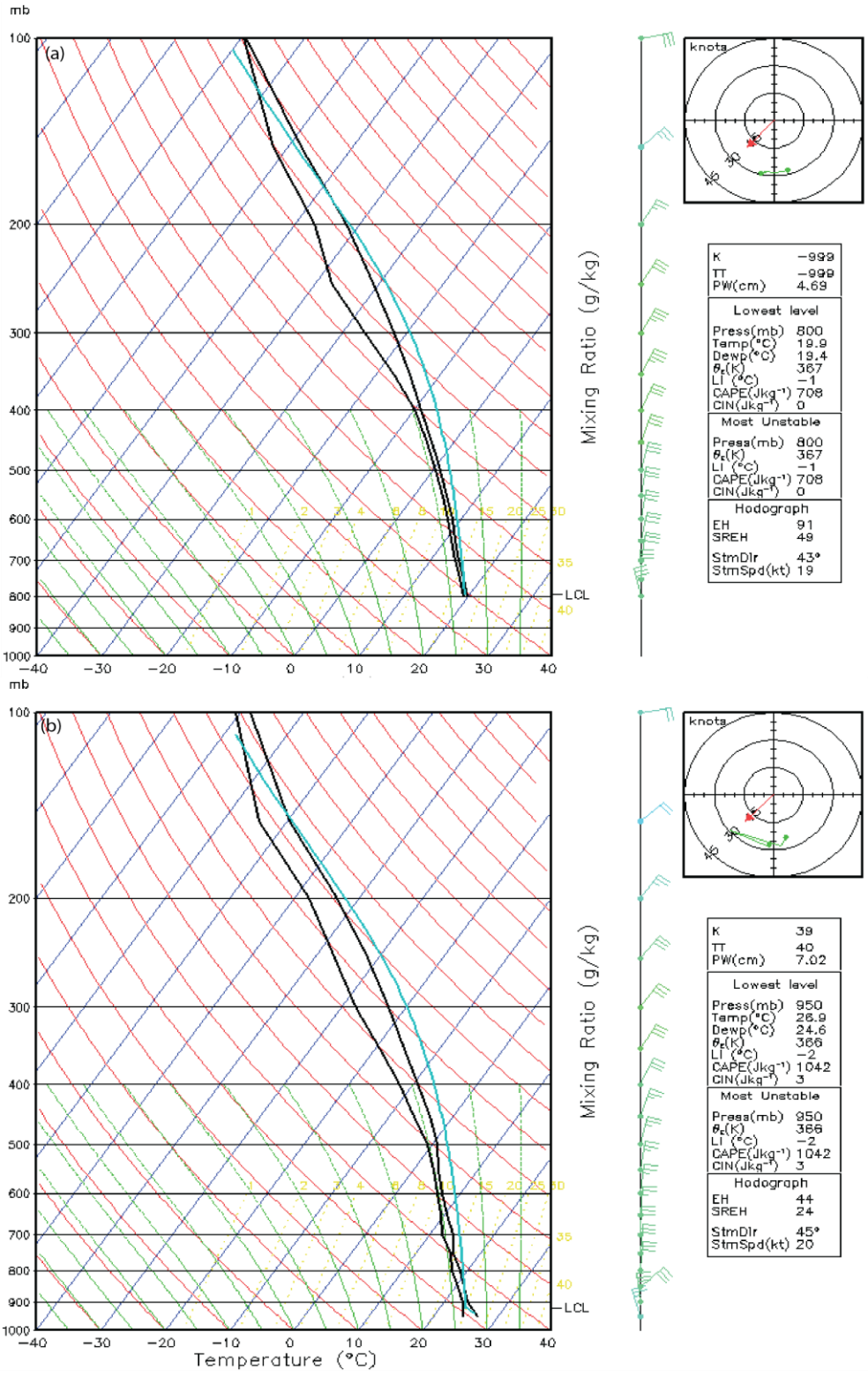

Figure 4.15. Skew T diagrams for (a) 06 UTC 7 August in the CTL-9 km case and (b) 03 UTC 7 August in the NT case.

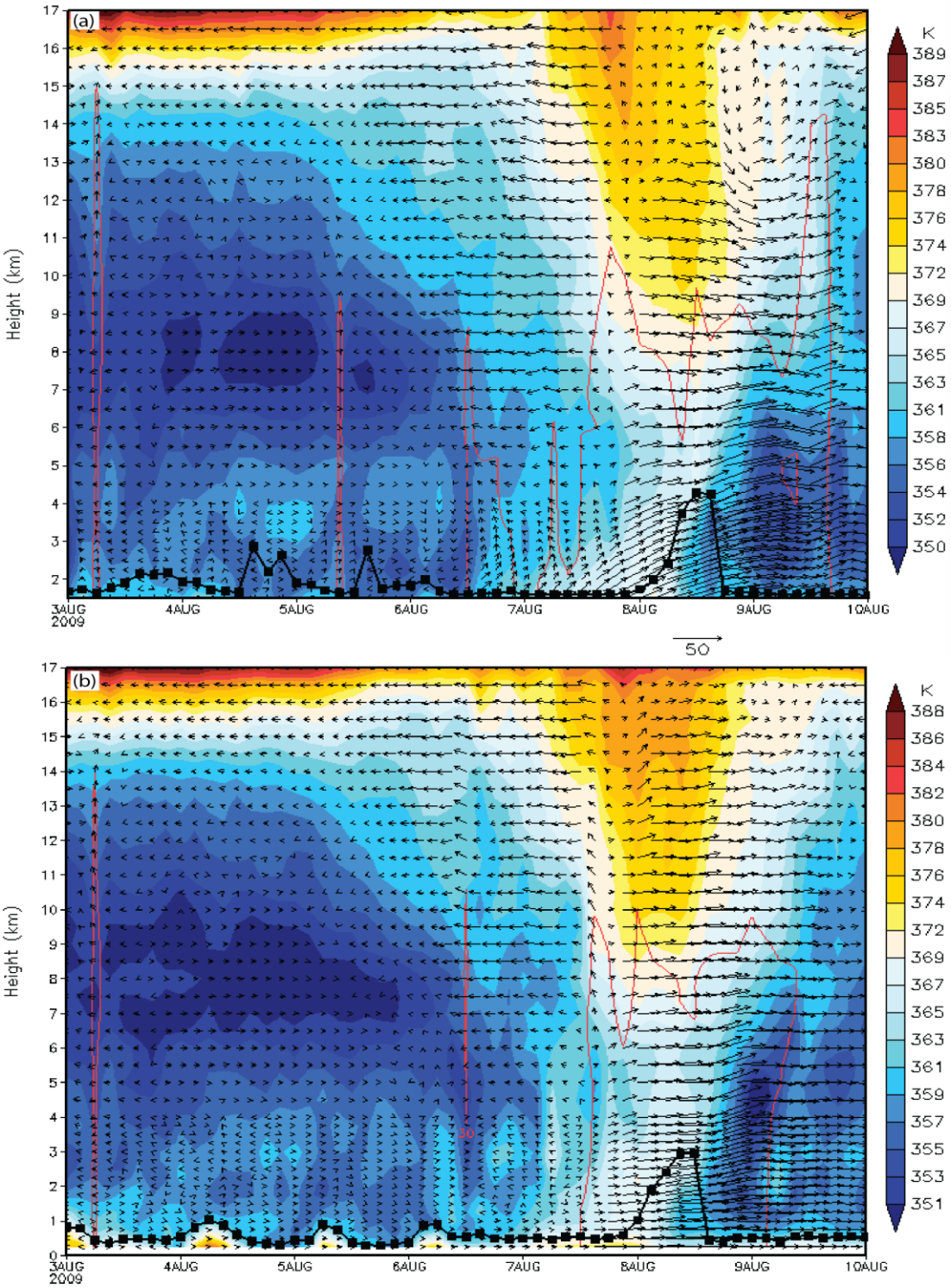

Figure 4.16. The time-height cross section of saturated equivalent potential temperature (shaded), the maximum reflectivity larger than 20 dBZ (red), wind vector, and LCL (bold) for the cases of (a) CTL-9 km and (b) NT.

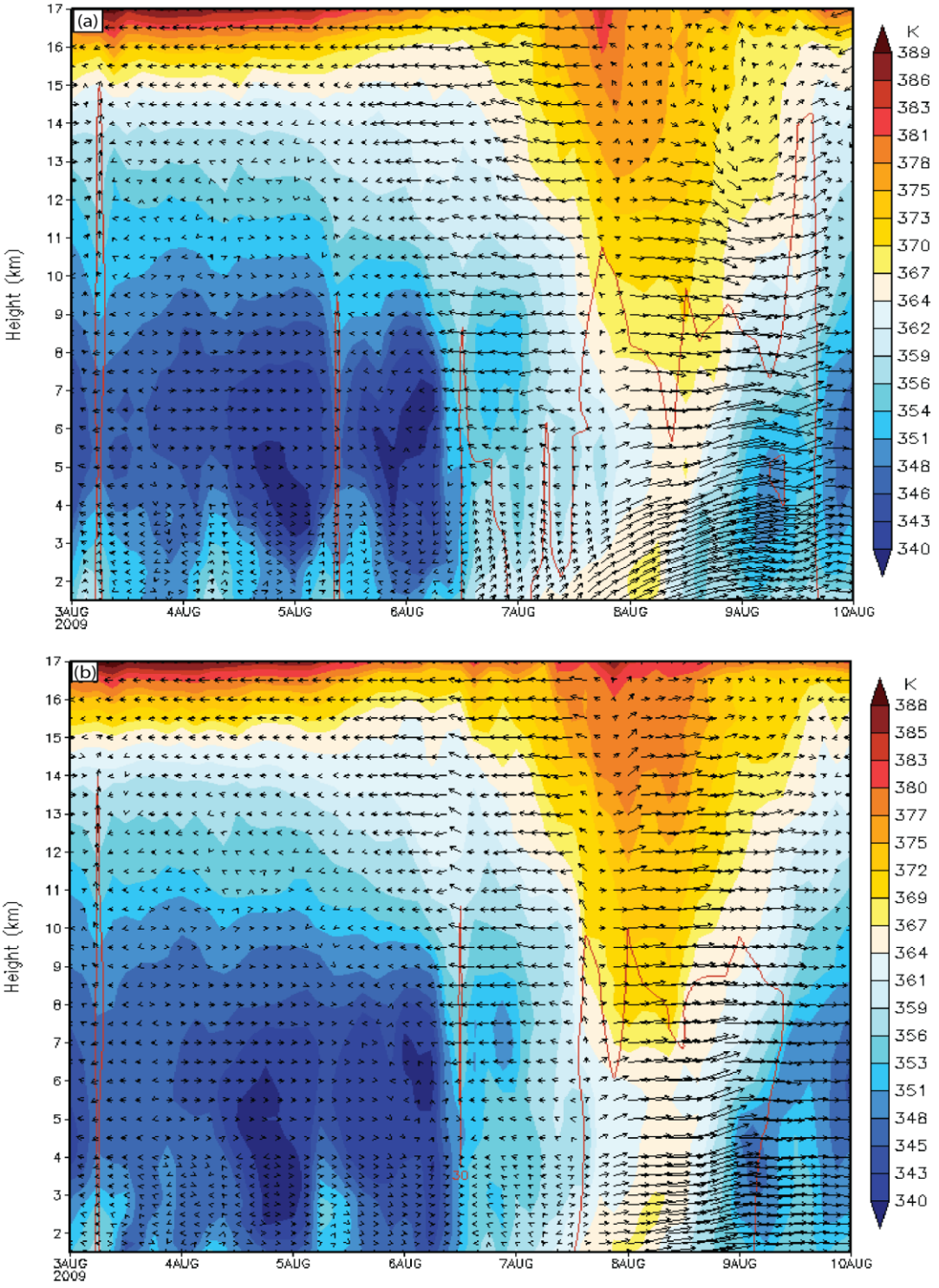

Figure 4.17. The time-height cross section of equivalent potential temperature (shaded), the maximum reflectivity 20 dBZ (red), and wind vector from the cases of (a) CTL-9 km and (b) NT.

Likewise, the mechanisms leading to the strong upward motion in producing the maximum precipitation 740.2 mm at (23.55°N, 120.67°E) in case NT include convergence and instabilities. In this study we would like to take a further investigation on instabilities on 8 August on both cases CTL and NT. As shown in Figure 4.14, it is not very humid near the surface on 8 August in case CTL and the environmental lapse rate minus moist adiabatic lapse rate is negative most time on 8 August in the case NT. Because of strong vertical motion the negative vertical gradients of θ_e and θ_e^* are much smaller, if any, than any other days during 00 UTC 3 August and 00 UTC 10 August. Also, LCL on 8 August is much higher (Figures 16-17). In fact, the vertical gradients of θ_e and θ_e^* are either neutral or stable near surface most of time on 8 August (Figures 4.16-17). The CAPE is only 224, 147, 0, and 8 J kg^{-1} in the CTL case, as well as 210, 105, 82, and 41 J kg^{-1} in the case NT at 00, 06, 12, and 18 UTC 8 August, respectively (Figure 4.15). The above indicates that all these three instabilities are negligible mechanisms responsible for the upward motion in producing the extremely heavy rainfall during 00 UTC 8 – 00 UTC 9 August in both cases CTL and NT. Therefore, the maximum precipitation 740.2 mm in the case NT appear to be attributed to horizontal convergence; the maximum precipitation 1835.9 mm in the CTL can be attributed to horizontal convergence and orographic lifting. The estimated precipitation caused by orographic lifting has a difference between 1835.9 mm and 740.2 mm without large error. And thus, orographic lifting is the most important mechanism for the upward motion bringing about the observed 1503.5 mm rainfall at the station at (23.51°N 120.81°E) during 00 UTC 8 August – 00 UTC 9 August among other mechanisms such as convergence between Morakot circulation and southwesterly, and instabilities although the exact simulated rainfall does not match well with the observed rainfall. Convergence appears to be the second dominant mechanism leading to the strong upward motion in the extremely

heavy precipitation; while on the contrary the role played by instabilities is negligible. However, before 8 August the three instabilities cannot be ignored for generating the upward motion which help produced the precipitation because of very humid air in the low levels, much larger environmental lapse rate minus moist adiabatic lapse rate, θ_e and θ_e^*, much lower LCL, and much larger CAPE than those on 8 August (Figures 4.14-4.17). The orographic lifting and/or convergence might not be able to outweigh instabilities for the upward motion producing the rainfall before 8 August. Hence, before 8 August it is uncertain about the most dominant mechanism for generating strong upward motion to produce precipitation.

4.5.2. The Factors of Upward Motion, Water Vapor, and Translation Speed. The total precipitation associated with the passage of a storm can be expressed as (3) (Lin et al., 2001; Lin 2007),

$$P = EwqL_s/c_s \tag{3}$$

where E is precipitation efficiency, w is vertical velocity, q is specific humidity, L_s is the horizontal scale of the convective system, and c_s is the propagation speed of the convective system (Lin et al., 2001). This study will assume the precipitation efficiency and the horizontal scale of the convective system are constant in the following discussion due to the difficulty in determining them. It is clear from Eq. (3) that all of the upward motion, water vapor and translation speed of a storm directly contribute to the total rainfall. The major mechanism leading to strong upward motion in producing heavy precipitation associated with the passage of Morakot on 8 August is orographic lifting as discussed in the last subsection. In order to understand the relative importance of orographic lifting, water vapor and the translation speed of a typhoon on the extremely heavy precipitation when Morakot passed by, five typhoons, Sinlaku (2008), Parma (2009), Jangmi (2008), Fanapi (2010), and Nanmadol (2011), were chosen to

compare with Morakot based on the availability of the storm-relative 16 km microwave-based total precipitable water imagery data and large maximum accumulated precipitation in a station in Taiwan.

Figure 4.18 compares the storm relative total precipitable water of Morakot with that of the five typhoons having the maximum accumulated rainfall of 1611, 1500, 1135, 1127, and 1104 mm, respectively. The case of Morakot has much more total precipitable water in the region around Taiwan than that of other cases. In fact, the abundant water vapor around Taiwan has been at least from 6 to 12 August 2009. The prevailing southwesterly transported abundant water vapor in the vicinity of Taiwan toward CMR when Morakot passed by. Therefore, the excessive water vapor in the case of Morakot produces excessive precipitation than that in other cases given that the other conditions in (3) are comparable such as precipitation efficiency, the horizontal scale of the convective system, upward motion, and translation speed. Hence, the large total precipitable water in a very large region around Taiwan makes water vapor play a significant role in the record-breaking accumulated precipitation.

In addition, the best-track data from the web site http://agora.ex.nii.ac.jp/digital-typhoon/index.html.en are used in the translation speeds and maximum wind speed when these six typhoons were near Taiwan. Because the track data of the six typhoons are from the same data source, the differences in tracks between simulation and different data sources are then not an issue. Figure 4.19 displays the translation speeds when these typhoons were near Taiwan. Among the chosen five typhoons, Jangmi (2008) and Fanapi (2010) moved no slower than 2.8 m s^{-1}. Sinlaku (2008) remained slower than 2.5 m s^{-1} from 06 UTC 12 September to 12 UTC 14 September except at 12 UTC 13 September and 00 UTC 14 September.

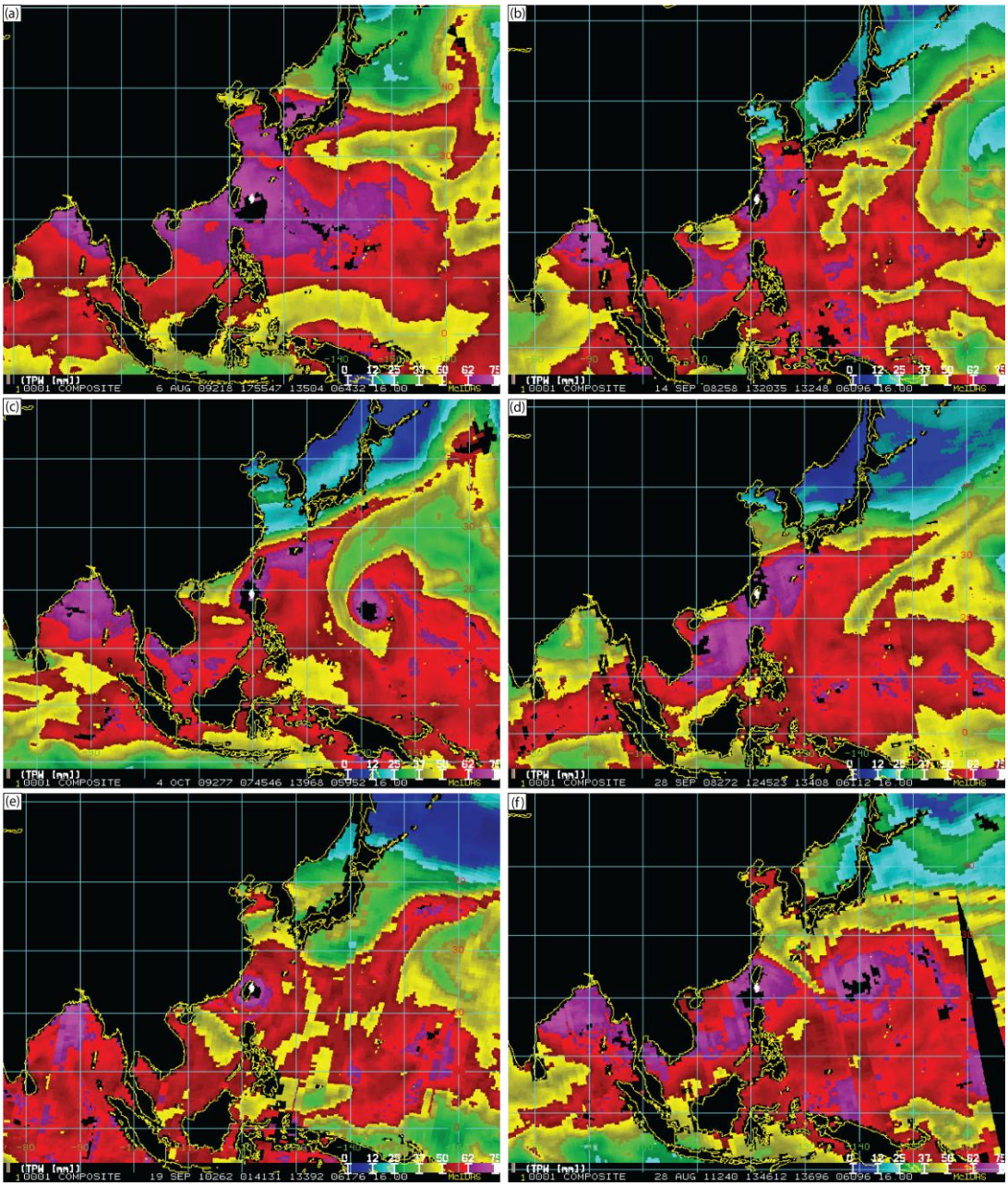

Figure 4.18. The storm relative 16 km microwave-based total precipitable water imagery on (a) 1755 UTC 6 August 2009 around Typhoon Morakot (2009), (b) 1320 UTC 14 September 2008 around Typhoon Sinlaku (2008), (c) 0745 UTC 4 October 2009 around Typhoon Parma (2009), (d) 1245 UTC 28 September 2008 around Typhoon Jangmi (2008), (e) 0141 UTC 19 September 2010 around Typhoon Fanapi (2010), and (f) 1346 UTC 28 August 2011 around Typhoon Nanmadol (2011).

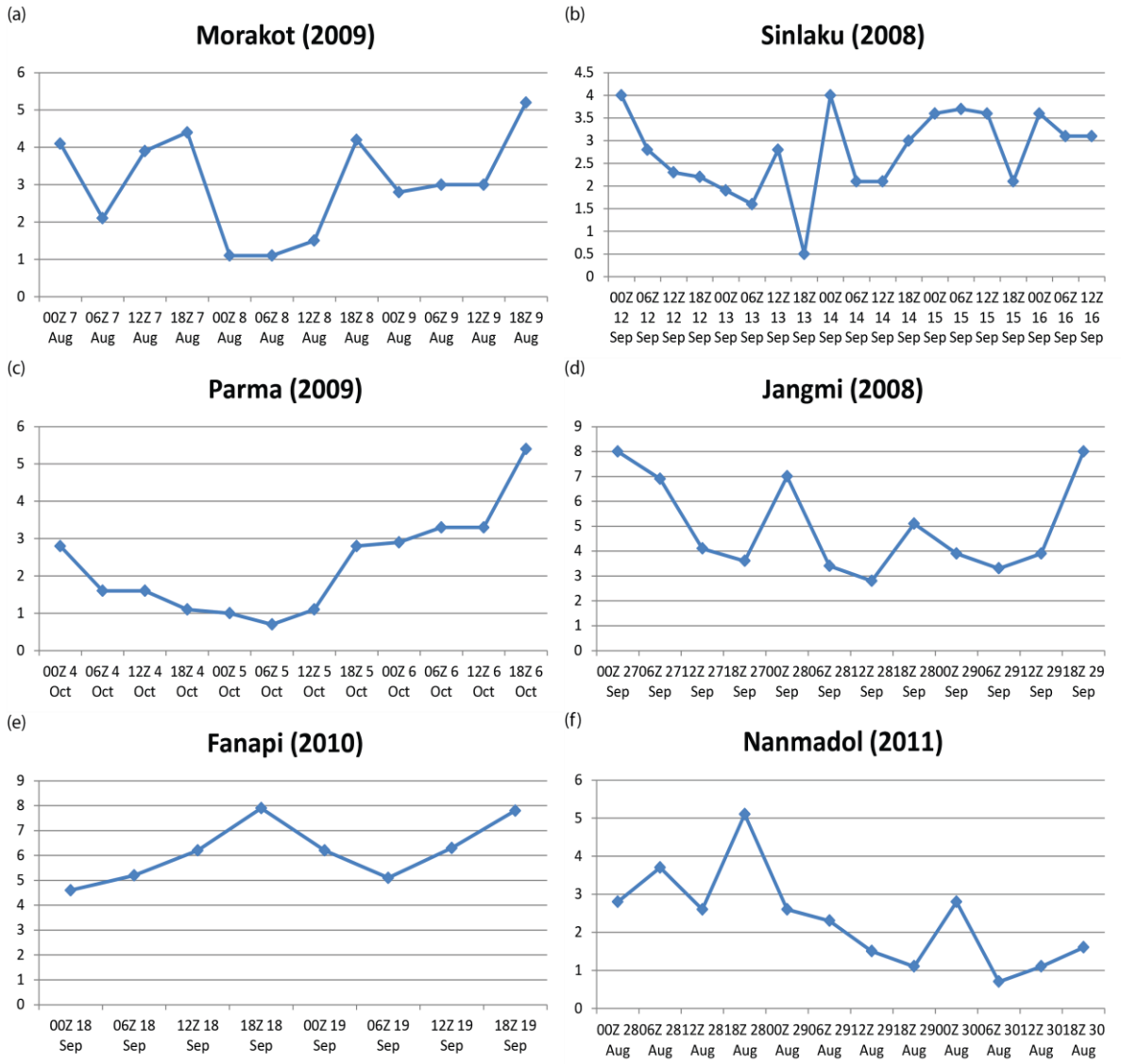

Figure 4.19. The translation speeds (m s^{-1}) every 6 hours for Typhoon (a) Morakot (2009), (b) Sinlaku (2008), (c) Parma (2009), (d) Jangmi (2008), (e) Fanapi (2010), and (f) Nanmadol (2011).

Parma (2009) moved slower than 2 m s^{-1} during 06 UTC 4 October – 12 UTC 5 October. Except 00 UTC 30 August Nanmadol (2011) propagated slower than 2.8 m s^{-1} from 00 UTC 29 August to 18 UTC 30 August. The slow moving of Morakot during 00 UTC 8 August – 12 UTC 8 August did cause more precipitation than a fast moving typhoon does according to (3). But the slow translation speeds 1.1 - 1.5 m s^{-1} during 00 UTC 8 August – 12 UTC 8 August are not

slower than 0.5 m s^{-1} in Sinlaku (2008), 0.7 m s^{-1} in Parma (2009), and Nanmadol (2011). The duration of slow translation speeds in Morakot is much short than that in Sinlaku (2008), Parma (2009), and Nanmadol (2011). Thus, the slow translation speed of Morakot during 00 UTC 8 August – 12 UTC 8 August does not outrank that in Sinlaku (2008), Parma (2009), and Nanmadol (2011). Hence, the slow translation speed is not the most important process bringing about the extremely heavy precipitation which is much larger than that in these five typhoons; but rather only a factor helping result in the extremely heavy rainfall.

Orographic induced vertical velocity can be calculated by the following (Lin et al. 2001, Witchcraft et al. 2005, and Lin 2007):

$$w_{oro} = U\frac{\partial h}{\partial x} \tag{4}$$

The maximum wind speeds in these six typhoons are illustrated in Figure 4.20. The maximum wind speed of Morakot when it generated extremely heavy precipitation was about 31 m s^{-1}, which is much smaller than 34.8 m s^{-1} in in Sinlaku (2008), 43.2 m s^{-1} in Jangmi (2008), and 39.6 m s^{-1} in Fanapi (2010). The locations with maximum accumulated precipitations of Sinlaku (2008), Jangmi (2008), and Fanapi (2010) are in the mountainous regions of Taichung County, Yilan County, and Pitung County, respectively. Actually the slope of terrain depends on the direction. In the study, the slope of terrain is calculated by the slope from the closest city in plain to the station. The slopes of the terrains and orographic liftings in Morakot (2009), Sinlaku (2008), Jangmi (2008), and Fanapi (2010) are calculated as Table 4.2. The orographic lifting of Morakot is the smallest one in the typhoons on Table 4.2. Hence, the orographic lifting of Morakot is not the most important process to generate much more precipitation than that in Sinlaku (2008), Jangmi (2008), and Fanapi (2010); but rather only a factor helping result in the extremely heavy rainfall.

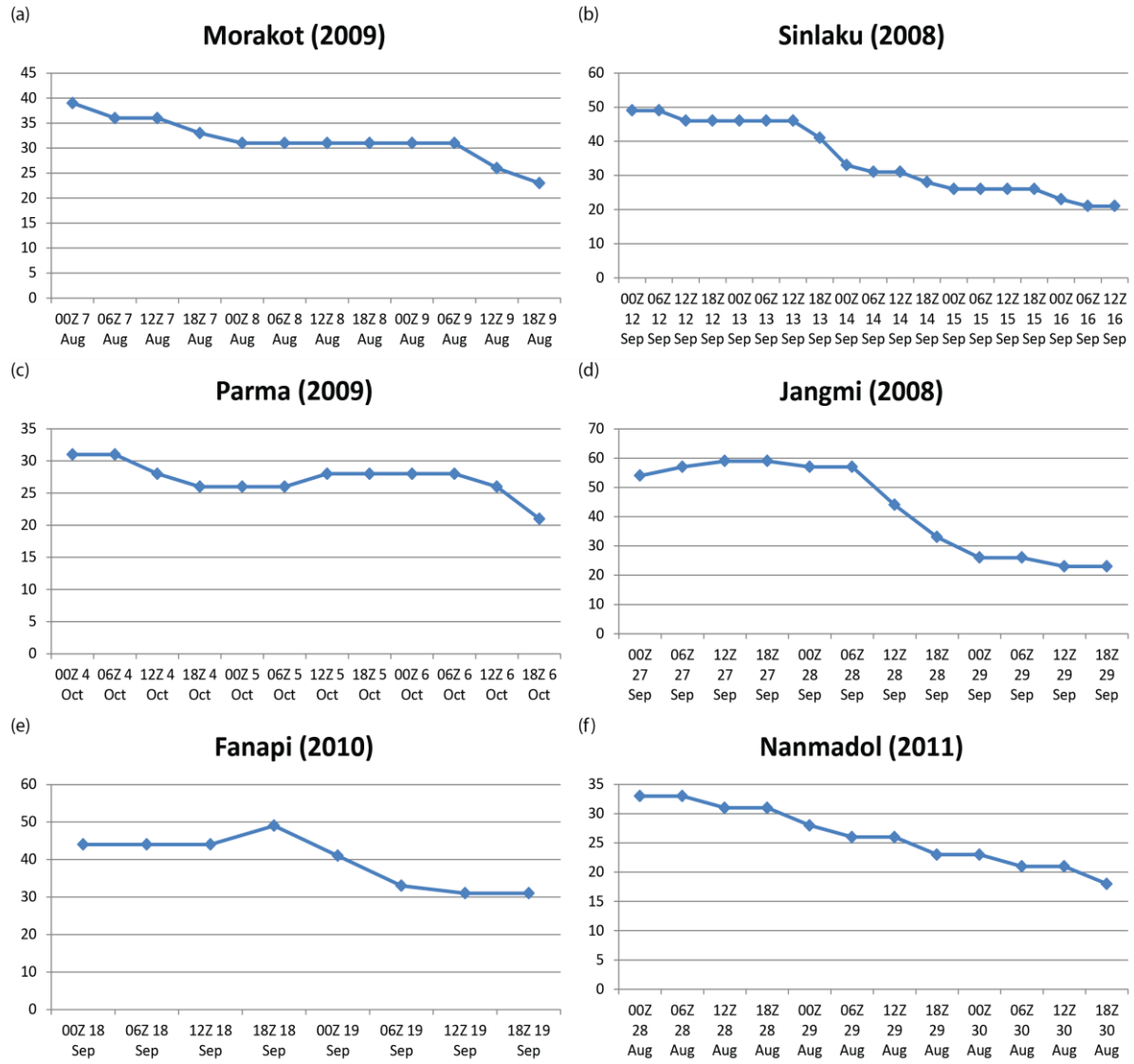

Figure 20. The maximum wind speeds (m s^{-1}) every 6 hours for Typhoon (a) Morakot (2009), (b) Sinlaku (2008), (c) Parma (2009), (d) Jangmi (2008), (e) Fanapi (2010), and (f) Nanmadol (2011).

After the comparison of total precipitable water vapor, translation speed, and orographic lifting between Morakot and these five typhoons, the translation speed and orographic lifting of Morakot don't outrank those of these five typhoons in generating precipitation. And thus, the translation speed and orographic lifting cannot shed light on much more maximum accumulated rainfall in Morakot than that in these five typhoons. In contrast, the total precipitable water vapor

around Taiwan in Morakot case is much more than that in these five typhoons. In fact, the abundant water vapor last at least from 6 to 12 August 2009. Therefore, in terms of the much larger maximum accumulated precipitation associated with the passage of Morakot than that in Sinlaku (2008), Parma (2009), Jangmi (2008), Fanapi (2010), and Nanmadol (2011), the abundant water vapor around Taiwan overshadows the slow translation and orographic lifting after the comparisons of Morakot and these five typhoons.

Table 4.2

The orographic lifting of Morakot (2009), Sinlaku (2008), Jangmi (2008), and Fanapi (2010)

Typhoon	Station height (m)	City height (m)	Distance (m)	Slope*	U* (ms^{-1})	Orographic lifting (ms^{-1})
Morakot	2413	150	34921	0.0648	31	2.01
Sinlaku	2605	234	25577	0.0927	34.8	3.23
Jangmi	1950	8	32937	0.0589	43.2	2.54
Fanapi	1166	50	19841	0.0562	39.6	2.23

*The terrain slope is calculated by the slope from the closest city in plain to the station. The wind speed is the mean wind speed when the typhoon is around Taiwan.

4.6. Precipitations in the Sensitivity Experiments to Terrain Elevation

4.6.1. Track and Intensity. Figure 4.21a demonstrates that all the tracks in these experiments, i.e. 0.8, 0.6, 0.5, 0.4, 0.2, and no terrain, and ocean, are similar to that of the case CTL. Under the impacts of dominating large-scale circulation, the changes in terrain elevation and the presence of land play a minor role in the track of Morakot. With regards to intensity, all these experiments have lower minimum sea level pressure and larger maximum wind speed than those in the CTL case due to weaker orographic blocking (Figs. 4.21b and 4.21c). But the responses to the change of terrain elevation are not linear (Figs. 4.21b and 4.21c).

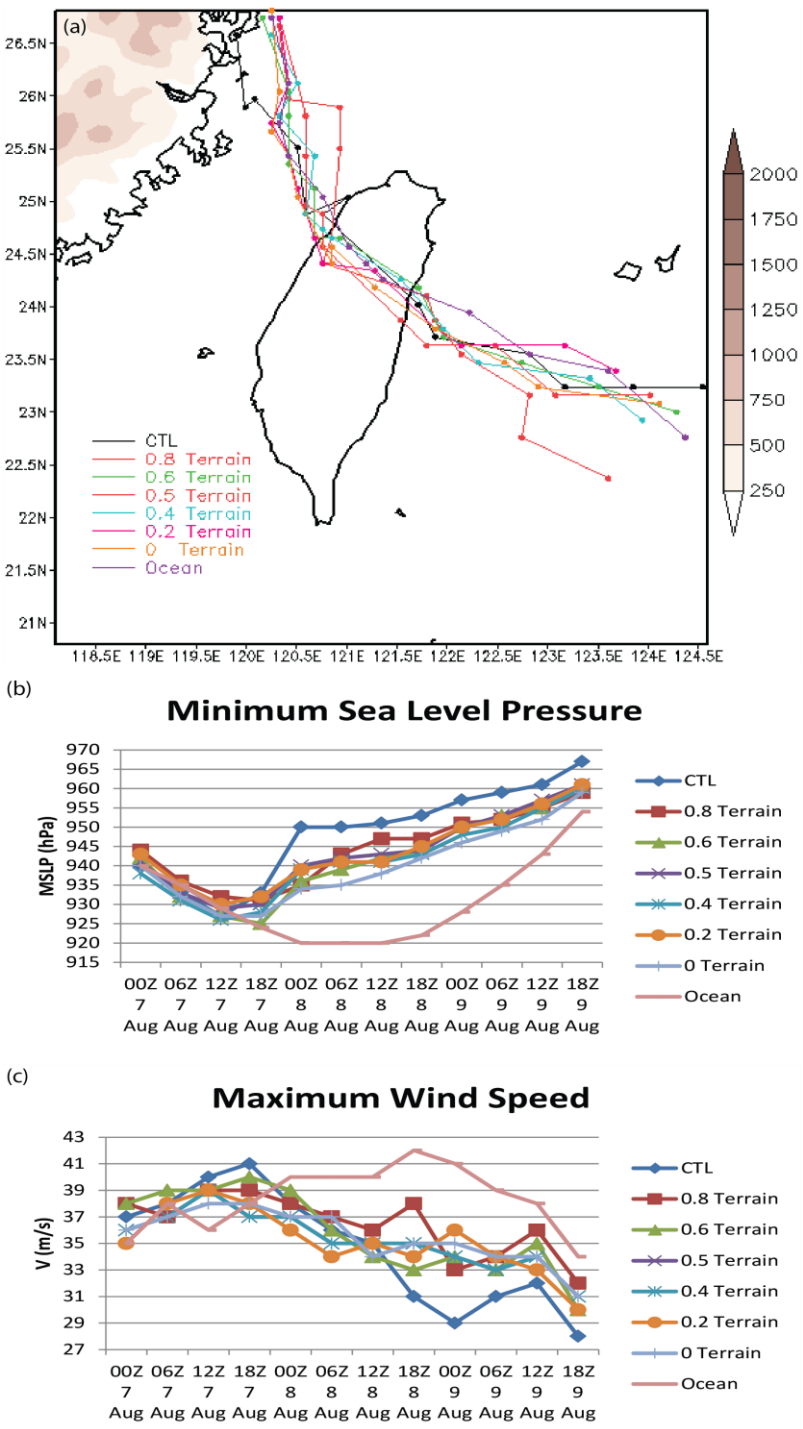

Figure 4.21. (a) The track, (b) minimum sea level pressure, and (c) maximum surface wind speed from the CTL-9 km case, the experiments of 0.8, 0.6, 0.5, 0.4, 0.2, and no terrain, and ocean every three hours from 00 UTC 7 August to 18 UTC 9 August. The shaded colors are terrain elevations (meter).

The minimum sea level pressure and maximum wind speed in case OCN are able to develop after Morakot passes over Taiwan, and thus, are much stronger than those in the other experiments with land because of the extra water vapor, latent heat and sensible heat from the ocean (Figures 4.21b and 4.21c). The minimum sea level pressure in the NT is less impacted by the mountain than that with higher elevation, and thus, is the second strongest (Figures 4.20b). Among all the cases in the experiment the effects in intensity of the presence of land are apparently much larger than those of terrain elevation (Figures 4.21b and 4.21c).

4.6.2. Accumulated Precipitation. The impacts of terrain elevation on accumulated precipitation of 8 August are shown in Figure 4.22. The vertical velocities of cases NT and OCN are only caused by instabilities and the convergence of Morakot circulation and southwesterly, and thus, the precipitation patterns are totally different from those in the CTL and the experiments with terrain, in which the major precipitation patterns are in the mountainous regions. Without orographic blocking, there is no orographic lifting, and thus, the precipitations in NT and OCN cases distribute much more evenly than that in the CTL case. Therefore the maximum accumulated rainfalls in NT and OCN cases are much less than those in the CTL case and the experiments with terrain. As the elevation of terrain decreases, the maximum accumulated rainfall maximum decreases. The above implies the importance of the orographically induced rain Morakot brings about. On 8 August Morakot moves northward very slowly and the prevalent wind in southern Taiwan is westerly. All the Froude numbers in the experiments with terrains are larger than 1 (Table 1), so the locations of maximum accumulated precipitations should be at the top of terrains when the orographically induced rainfall is much more important than any other processes. However, only in the experiments of 0.5T and 0.4T have maximum accumulated rainfall located around the top of the CMR.

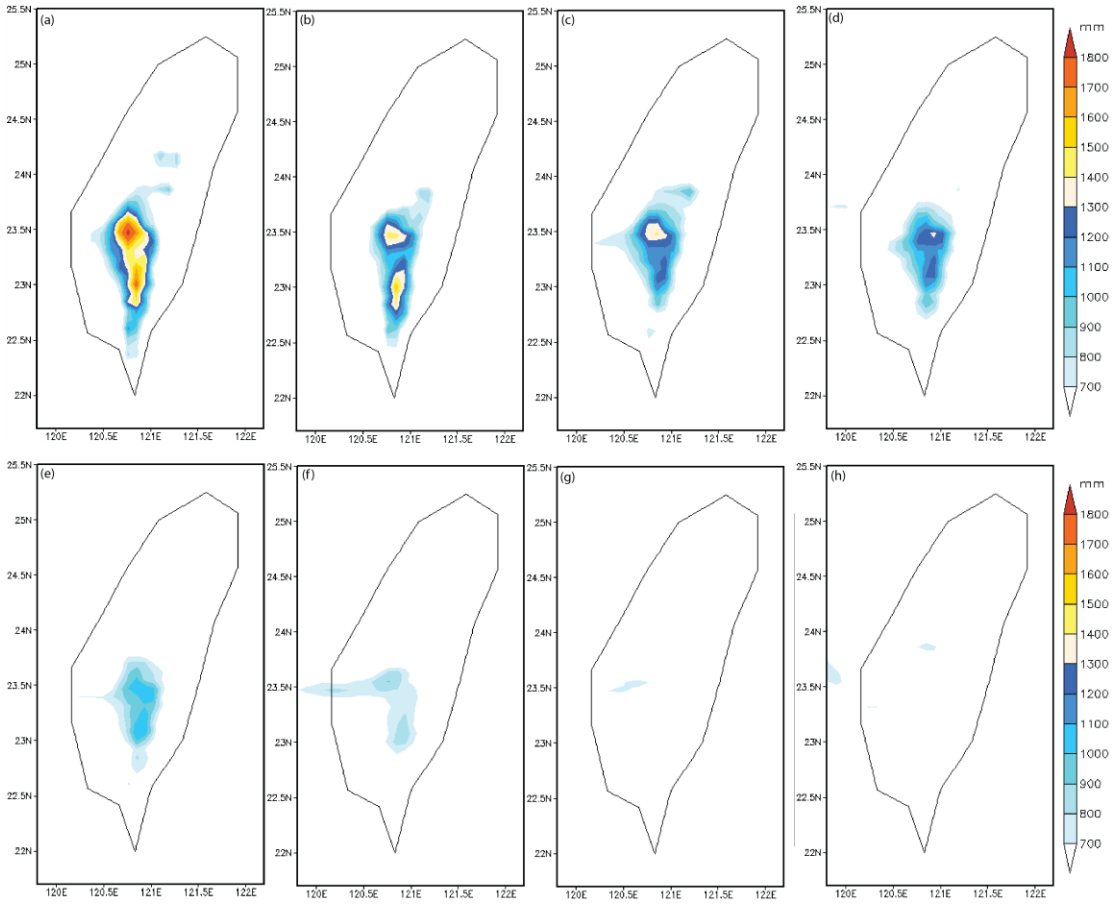

Figure 4.22. The accumulated precipitations during 00 UTC August 8 – 00 UTC 9 August from (a) the CTL with 9 km grid interval, the experiments of (b) 0.8, (c) 0.6, (d) 0.5, (e) 0.4, (f) 0.2, (g) no terrain, and (h) ocean.

Actually, the locations of maximum accumulated rainfall cannot be completely explained simply by the classic theory of flow over mountain (Smith 1979) although they shift to the top of CMR as the elevation of terrain reduces except 0.2T. This indicates that some other mechanism(s) play a significant role in producing the precipitation. In fact, the locations where convergences happen are not much different in the experiments of 0.5T, 0.4T, 0.2T, and NT because of similar tracks (see Figure 4.23).

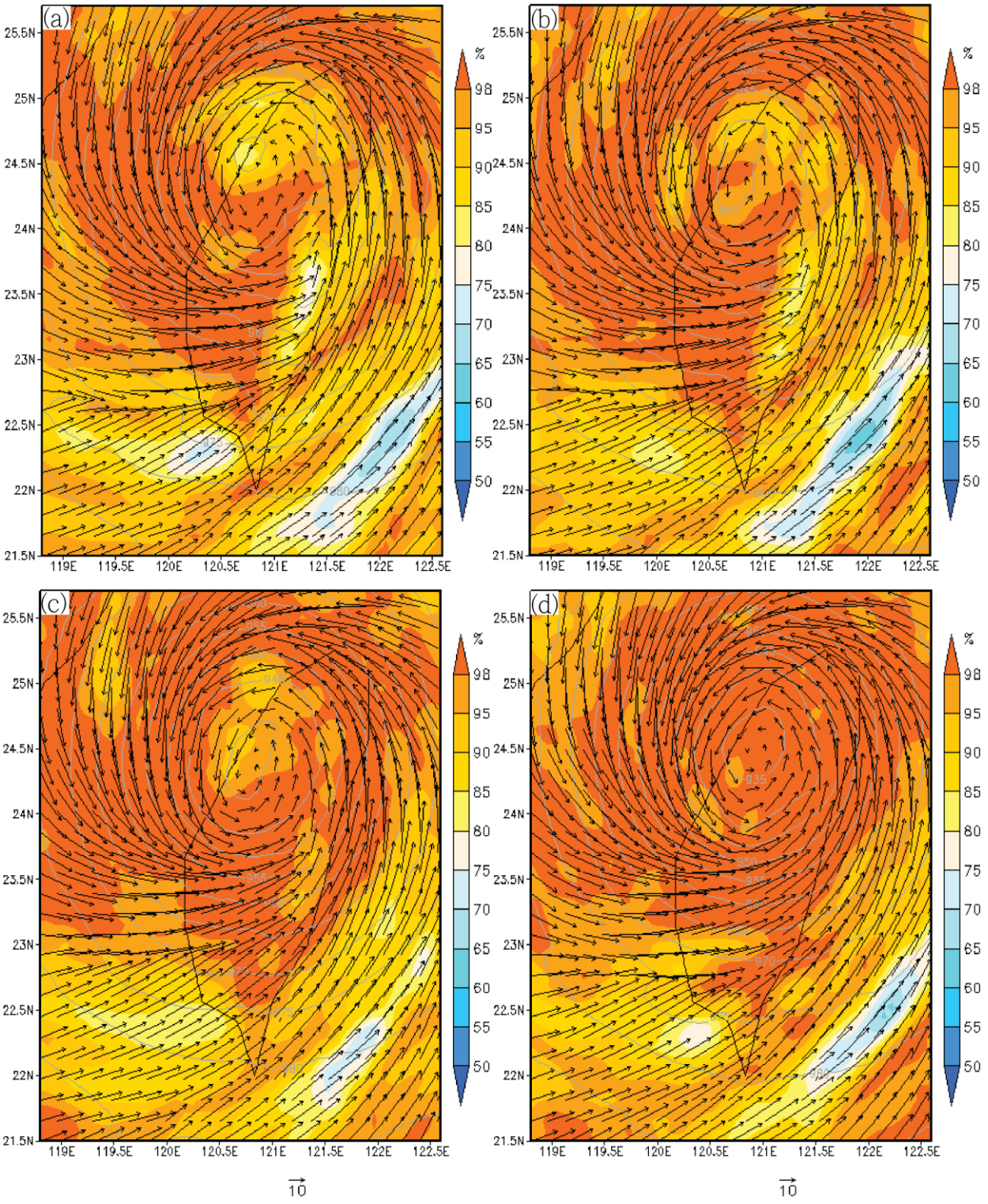

Figure 4.23. Relative humidity (shaded), wind vector, and sea level pressure (grey contours) at 06 UTC 8 August from the experiments of (a) 0.5, (b) 0.4, (c) 0.2, and (d) no terrain.

The locations with maximum accumulated precipitations in the experiments of 0.2T and NT are consistent with those with convergences of Morakot circulation and southwesterly, namely, located before the top of CMR (Figs. 4.22f, 4.22g, 4.23c and 4.23d). Hence, the location of maximum accumulated precipitations is an issue of competition of water vapor between orographic lifting and convergences. Furthermore, Figure 4.24a demonstrates close to a linear relationship between the maximum accumulated rainfall and the terrain elevation during both 00 UTC 3 August - 00 UTC 10 August and 00 UTC 8 August - 00 UTC 9 August. The maximum accumulated precipitation during 00 UTC 8 August - 00 UTC 9 August is much more than those in any other day during 00 UTC 3 August - 00 UTC 10 August (Figure 4.24b). Therefore, there still is nearly a linear relationship between the maximum accumulated rainfall and the terrain elevation during 00 UTC 3 August - 00 UTC 10 August, although it is not that prevailing wind is westerly every day during the period. The quasi-linear relationship between the maximum accumulated rainfall and the terrain elevation demonstrates that the maximum accumulated precipitation is associated with the strength of orographic lifting. In view of the linear flow regime (Fr>1) in all the CTL and experiment cases, quasi-linear relationship is reasonable. In addition, similar results in terms of max surface winds and minimum sea level pressure, but different accumulated precipitations in the experiments implies that the heavy precipitation to the south of typhoon center has little feedback to max surface winds and minimum sea level pressure although the heavy precipitation happens to the south of storm center in both CTL and experiments since the ocean stage. In fact, the storm does not move southward.

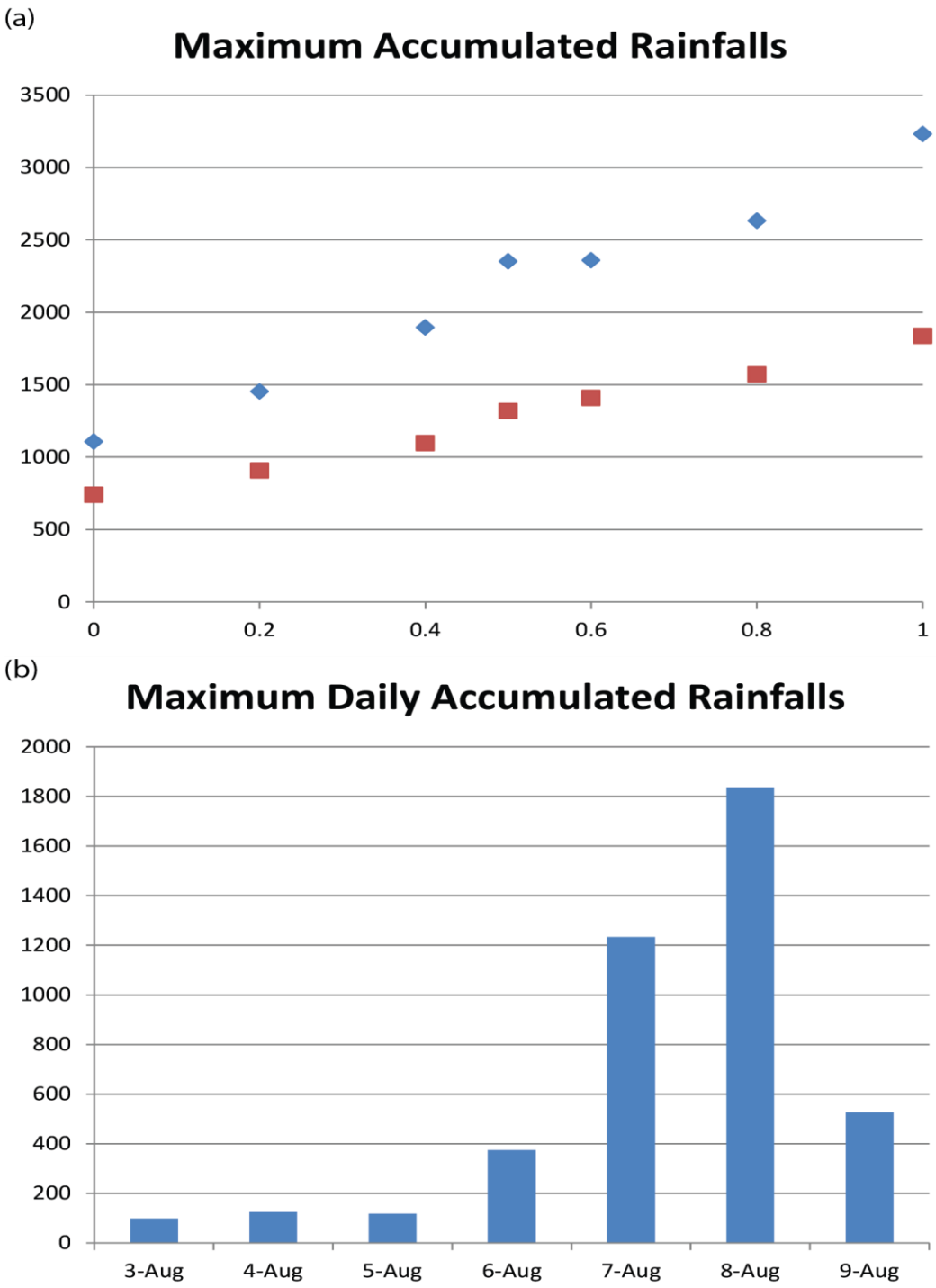

Figure 4.24. (a) The accumulated rainfall from the CTL-9 km and the experiments during (blue) 00 UTC 3 August - 00 UTC 10 August and (red) 00 UTC 8 August - 00 UTC 9 August. (b) The maximum daily accumulated rainfall from 3 August to 9 August in UTC.

4.7. Conclusion

In this study the storm relative 16 km microwave-based total precipitable water imagery is used to examine the abundance of water vapor. The WRF-ARW model is employed to conducted simulations in order to investigate the time evolution of three-dimensional structure, the factors causing the extremely heavy precipitation, and the impacts of terrain elevation on the precipitation connected to Typhoon Morakot (2009) by numerical experiments. The control case is able to successfully reproduce the track, the change of movement, characteristic rainbands, and precipitation patterns and maxima after verification against observational data such as best track analysis, maximum radar reflectivity, and rain gauge. Especially the location with maximum rainfall in the CTL with grid interval 9 km is only less than 6.6 km away from that in the observational data.

We found that the diameter of eye is larger than 0.7 degree width in latitude at 23.24°N at 00 UTC 7 August. The eye has contracted gradually to be smaller since then, much smaller after landfall, and then disappeared within two hours afterward. The outward flow at high levels of the secondary circulation in the eye wall is not very clear in the ocean stage. In the stage of just landfall, the deep convection at the windward side of the CMR in the CTL helps strengthen the second circulation at the side close to the coast. Similarly, the deep convection on land helps form the second circulation in the experiment of no terrain. The cloud-free eye in the CTL disappears within two hours after landfall. The deep convection, secondary circulation and tilting maximum wind speeds disappear, and the eye wall collapsed within five hours after landfall in the CTL. Without the impacts of the high and steep CMR, the decaying eye wall in the case NT is much weaker and slower than that in the CTL case. With the extra water vapor, latent heat, and sensible heat in the case of OCN, the storm develops continuously after the passage of Taiwan,

and thus, the secondary circulation is much clearer than that when the storm well develops in the ocean stage in the CTL case.

It is shown in the CTL case that the wind speed, convergence, upward motion, and relative humidity close to the Morakot center are limited when it crossed northern Taiwan; whereas large wind speed, convergence, upward motion, and humid regions are away from the Morakot center to the south. Due to the interactions between Morakot circulation, the high and steep CMR, and the prevailing southwesterly, the major precipitation associated with the passage of Morakot is located to the south and away from the Morakot center. Hence, there is no deep convection in the vertical cross section figure close to Morakot center when it crossed northern Taiwan, and thus, the precipitation is limited. Therefore, the asymmetric precipitation pattern is pretty pronounced. In the analysis of major mechanisms resulting in strong upward motion in the extremely heavy precipitation during 00 UTC 8 August – 00 UTC 9 August, orographic lifting dominates the upward motion. The convergence of Morakot circulation and southwesterly appears to be the second significant mechanism leading to the upward motion in the extremely heavy precipitation; whereas the role played by instabilities, including moist absolute instability, conditional instability, and convective instability, is negligible. Nevertheless, these instabilities cannot be ignored to be responsible for the precipitation before 00 UTC 8 August.

In the comparison of total precipitable water, translation speed, and orographic lifting with those of five typhoons in recent years bringing large accumulated precipitation to Taiwan, the case of Morakot possesses much more abundant water vapor around Taiwan than that in these five typhoons. Morakot does not move more slowly than the three slow typhoons do. The duration of slow translation in the Morakot case is much shorter than that in the three slow-moving typhoons. The maximum wind speed of Morakot is much smaller than that in three

typhoons with large wind speed. The calculated orographic lifting in Morakot is smaller than that in the three typhoons with large wind speed. Therefore, considering the factors leading to the extremely heavy rainfall, the abundant water vapor outweighs slow translation speed and orographic lifting. The slow translation speed and orographic lifting are two minor factors helping generate the extremely heavy rainfall.

The tracks in numerical experiments of terrain elevation and the presence of land do not change much under the dominant large-scale circulations. Because of less strong blocking of CMR, the intensities in all the cases in the experiments do not weaken as quickly as that in the CTL case. The response in intensity to the change of terrain elevation is not linear. Particularly, the ocean experiment continuously develops after passing Taiwan with the contribution of extra sensible heat, latent heat and water vapor. In terms of Morakot intensity, the presence of land is much more important than terrain elevation. As the terrain elevation reduces, the maximum accumulated precipitation reduces. There is a quasi-linear relationship between terrain elevation and maximum accumulated precipitation for both periods, 00 UTC 8 August – 00 UTC 9 August and 00 UTC 3 August – 00 UTC 10 August which indicates that the maximum accumulated precipitation is related to the strength of orographic lifting. Due to the lack of the effects of orographic lifting the precipitation patterns in the experiments of no-terrain and ocean are completely different from those in the cases with terrain in which the precipitation patterns are located in the mountainous regions. Considering the linear flow regime (Fr>1) in all the CTL and experiment cases, quasi-linear relationship is reasonable.

CHAPTER 5

Conclusion and Discussion

Data analysis could reveal the specialties of phenomena in atmospheric sciences. When data are sparse, analysis cannot display much meaningful information. In numerical experiments conditions can be changed to systematically discuss a research topic. Hence, numerical studies are very powerful in research. In this dissertation numerical studies are applied to understanding the orographic effects on tropical weather systems such as AEWs and Typhoon Morakot (2009).

An AEW may be generated by vortex shedding. In order to justify the hypothesis, we conduct numerical modeling to simulate an easterly flow over a idealized large-scale mountain, mimicking the Ethiopian Highlands. In addition, to systematically understand the impacts of Coriolis parameter, planetary vorticity gradient (β), basic wind speed, vertical wind shear, and mountain height, length and width on vortex shedding, we change the dimensional parameters associating with the above variables. Some preliminary results indicate that wave-like disturbances were generated on the lee side by vortex shedding for an easterly flow over an idealized mountain, with a wavelength of 2000 km, a period of 2-3 days, and a propagating speed of 9.6 ms^{-1} which mimic an AEW. Furthermore, these orographically generated hydrostatic, continuously stratified inertia-gravity waves on a β-plane are characterized as mixed Rossby-gravity waves based on the dispersion relationship. The dispersion relationship gives a phase speed of about -10 ms^{-1}, which is comparable to numerically simulated 9.6 ms^{-1} and the observed 8 ms^{-1}. Several critical forcings of AEWs formation are found in sensitivity tests. Without the Coriolis force, AEW-like disturbances cannot be generated. The β effects are essential in maintaining the lee vorticity. Hence, it is proposed that the AEW-like disturbances are associated with orographically forced Rossby waves. At an earlier stage of the development

of an AEW-like disturbance, the inertial force is more dominant than nonlinearity and β effects. At later stage the AEW-like disturbances wanes with weak flow nonlinearity, and β effects. Thus, the nonlinearity and/or β effects are important in sustainability of lee vorticity. It is found that the larger the wind shear, the less the lee vortices and the more vertically propagating waves are generated. In addition, stronger and larger AEW-like waves are produced by stronger nonlinearity, a steeper mountain, or a larger mountain width-length aspect ratio.

With regard to Morakot, the study conducts numerical experiments and uses total precipitable water data to explore the three-dimensional structure, the asymmetric rainfall patterns, the factors leading to extremely heavy precipitation, and the impacts of terrain elevation on the precipitation associated with the passage of Typhoon Morakot (2009) over the Central Mountain Range (CMR) of Taiwan. The numerical study successfully reproduces the track, the track change, rain band characteristics, and precipitation patterns after verification against observational data and best track analysis. It is found that in the ocean stage the upper outflow of the secondary circulation is not very clear. In the early stage of landfall, the deep convection on the windward (west) side of the CMR helps strengthen the second circulation in the vicinity of the coast. The eye disappears within two hours after landfall. The deep convection, secondary circulation and tilting maximum wind speeds disappear, and the eye wall corrupts within five hours after landfall. The wind speed, convergence, upward motion, and relative humidity close to the Morakot center are limited when it crossed northern Taiwan; whereas large wind speed, convergence, upward motion, and humid regions with heavy precipitation are away from the Morakot center to the south because of the interactions between Morakot circulation, the high and steep CMR, and the prevailing southwesterly wind. After the comparison of total precipitable water, translation speed, and maximum wind speed with those in five typhoons in

recent years causing large accumulated rainfall in Taiwan, it is shown that the abundant water vapor around Taiwan outweighs translation speed and orographic lifting in resulting in the record-breaking precipitation. In the analysis of major mechanisms leading to strong upward motion in the extremely heavy precipitation during 00 UTC 8 August - 00 UTC 9 August, orographic lifting dominates the upward motion; while on the contrary the role played by instabilities is negligible. Based on sensitivity experiments, it was found that Morakot's track was not sensitive to the terrain elevation and the presence of land. In terms of Morakot intensity, the presence of land is more significant than terrain elevation. There is a quasi-linear relationship between the terrain elevation and maximum accumulated precipitation for both periods in the numerical experiments of terrain elevation indicating the precipitation is more or less related to the strength of orographic lifting.

References

Batchelor, G. K., 1957: On steady laminar flow with closed streamlines at large Reynolds numbers. *J. Fluid Mech.,* **1,** 177–190.

Bender, M. A., R. E. Tuleya, and Y. Kurihara (1987), A numerical study of the effect of island terrain on tropical cyclones, *Mon. Wea. Rev.*, **115**, 130–155,

Beyer, W. H., ed., 1987: CRC Handbook of Mathematical Sciences, CRC Press, pp860.

Berry, G. J. and C. D. Thorncroft, 2005: Case study of an intense African easterly wave. *Mon. Wea. Rev.*, **133,** 752-766.

Bolin, B. 1950: On the influence of the earth's orography on the general character of the westerlies. *Tellus,* **2**, 184-195.

Burpee, R. W., 1972: The origin and structure of easterly waves in the lower troposphere of North Africa. *J. Amos. Sci.,* **29,** 77-90.

Carlson, T. N., 1969: Synoptic histories of three African disturbances that developed into Atlantic hurricanes. *Mon. Wea. Rev.*, **97**, 256–276.

Chan, J. and W. Gray, 1982: Tropical cyclone movement and surrounding flow relationships. *Mon. Wea. Rev.*, **110**, 1354-1374.

Chang, C.-B., 1993: Impact of desert environment on the genesis of African wave disturbances. *J. Amos. Sci.,* **14,** 2137-2145.

Charney, J. G., and A. Eliassen, 1949: A numerical method for predicting the perturbations of the middle latitude westerlies. Tellus, 1, 38-54.Clark, T. L., 1977: A small scale dynamic model using a terrain-following coordinate transformation. *J. Comput. Phys.*, **24**, 186–215.

Chen, Y., and M. K. Yau (2003), Asymmetric structures in a simulated landfalling hurricane, *J. Atmos. Sci.*, **60**, 2294–2312, doi:10.1175/1520-0469(2003)060<2294:ASIASL>2.0.CO;2.

Chien, F.-C., and H.-C. Kuo (2011), On the extreme rainfall of Typhoon Morakot (2009), *J. Geophys. Res.*, **116**, D05104, doi:10.1029/2010JD015092.

Cressman, G. P., 1959: An Operational Objective Analysis System. *Mon. Wea. Rev.*, **87,** 367-374.

Doswell, C. A., III, H. Brooks, and R. Maddox, 1996: Flash flood forecasting: An ingredient-based methodology. *Wea. Forecasting*,**11,** 560–581.

Doyle, J. D., and M. A. Shapiro (1999), Flow response to large-scale topography: The Greenland tip jet, *Tellus*, Ser. A, **51**, 728 – 748.

Dudhia, J., 1989: Numerical Study of Convection Observed during the Winter Monsoon Experiment Using a Mesoscale Two-Dimensional Model. *J. Atmos. Sci.* **46**, 3077-3107

Gal-Chen, T., and R. C. J. Sommerville, 1975: On the use of a co-ordinate transformation for the solution of the Navier–Stokes equations. *J. Comput. Phys.*, **17**, 209–228.

Ge, X., T. Li, S. Zhang, and M. Peng, 2010: What causes the extremely heavy rainfall in Taiwan during Typhoon Morakot (2009)? *Atmos. Sci. Lett.*, **11**, 46–50, doi:10.1002/asl.255.

Gray, W. M., 1968: Global view of the origin of tropical disturbances and storms. *Mon. Wea. Rev.,* **96,** 669–700.

Grose, W. L., and B. J. Hoskins, 1979: On the influence of orography on large-scale atmospheric flow. *J. Atmos. Sci*., **36**, 223-234.

Hong, S.-Y., Y. Noh, and J. Dudhia, 2006: A new vertical diffusion package with an explicit treatment of entrainment processes. *Mon. Wea. Rev.,* **134,** 2318–2341.

Hong, C. C., M. Y. Lee, H. H. Hsu, and J. L. Kuo, 2010: Role of submonthly disturbance and 40–50 day ISO on the extreme rainfall event associated with Typhoon Morakot (2009) in Southern Taiwan. *Geophysical Research Letters*, **37**, L08805, doi:10.1029/2010GL042761, 2010.

Hsu, H.-H., 1987: Propagation of low-level circulation features in the vicinity of mountain ranges. *Mon. Wea. Rev.*, **115**, 1864–1892.

Hunt, J. C. R., and W. H. Snyder, 1980: Experiments on stably stratified flow over a model three-dimensional hill. *J. Fluid. Mech.*, **7,** 671–704.

Kain, J. S., 2004: The Kain–Fritsch convective parameterization: an update. *J Appl. Meteor.*, **43**, 170–181.

Klemp, J. B., and D. R. Durran, 1983: An upper boundary condition permitting internal gravity wave radiation in numerical meso-scale models. *Mon. Wea. Rev.*, **111**, 430–444.

Lee, W.-C., B. J.-D. Jou, P.-L. Chang, and F.D. Marks. 2000 "Tropical cyclone kinematic structure retrieved from single-Doppler radar observations. Part III: Evolution and structures of Typhoon Alex (1987)." *Mon. Wea. Rev.*, **128**(**12**), 3982-4001.

Liang, J., L. Wu, X. Ge, and C.-C. Wu, 2011: Monsoonal Influence on Typhoon Morakot (2009). Part II: Numerical Study. *J. of Atmos. Sci.*, **68**, 2222-2235.

Lin, C.-Y., Hsu, H.-M., Sheng, Y.-F., Kuo, C.-H., Liou, Y.-A., 2011: Mesoscale processes for super heavy rainfall of Typhoon Morakot (2009) over Southern Taiwan. *Atmospheric Chemistry and Physics*, **11**, 345-361, 10.5194/acp-11-345-2011.

Lin, Y.-L., 2007: *Mesoscale Dynamics*, Cambridge University Press, 630pp.

Lin, Y.-L., 2009: Formation of African easterly waves and mesoscale convective systems in eastern North Africa and its impacts on the tropical cyclogenesis over eastern Atlantic Ocean. NSBP Proceedings.

Lin, Y.-L., S. Chiao, T. A. Wang, M. L. Kaplan, and R. P. Weglarz, 2001: Some Common Ingredients for Heavy Orographic Rainfall. *Wea. For.*, **16**, 633-660.

Lin, Y.-L., J. Han, D. W. Hamilton, and C.-Y. Huang, 1999: Orographic influence on a drifting cyclone. *J. Atmos. Sci.*, **56**, 534-562.

Lin, Y.-L., N.-H. Lin, and R. P. Weglarz, 1992: Numerical modeling studies of lee mesolows, mesovortices, and mesocyclones. *Meteor. Atmos. Phys.*, **49**, 43-67.

Lin, Y.-L., K. E. Robertson and C. M. Hill, 2005: Origin and propagation of a disturbance associated with an African easterly wave as a precursor of Hurricane Alberto (2000). *Mon. Wea. Rev.*, **133,** 3276-3298.

Lin, Y.-L., and Wang, T.-A., 1996: Flow regimes and transient dynamics of two-dimensional stratified flow over an isolated mountain ridge. *J. Atmos. Sci.,* **53**, 139-158.

Janowitz, G. S., 1975: The effect of bottom topography on a stratified flow in the Beta plane. *J. Geophys. Res.* **80,** 4163–4168.

Manabe, S., and T. B. Terpstra (1974), The effects of mountains on the general circulation of the atmosphere as identified by numerical experiments, *J. Atmos. Sci.*, **31**, 3 – 42.

Mekonnen, A., C. D. Thorncroft, and A. Aiyyer, 2006: Analysis of convection and its association with African easterly waves. *J. Climate,* **19,** 5405–5421.

Mlawer, E. J., S. J. Taubman, P. D. Brown, M. J. Iacono, and S. A. Clough, 1997: Radiative transfer for inhomogeneous atmospheres: RRTM, a validated correlated-k model for the longwave. *J. Geophys. Res.*, **102**, 16,663-16,682.

Mozer, J. B., and J. A. Zehnder, 1996: Lee vorticity production by large-scale tropical mountain ranges. Part II: A mechanism for the production of African easterly waves. *J. Atmos. Sci.*, **53**, 539–549.

Orlanski, I., 1976: A simple boundary condition for unbounded hy-perbolic flows. *J. Comput. Phys.*, **21**, 251–269.

Parish, T. R., 1982: Barrier winds along the Sierra Nevada mountains. *J. Appl. Meteor.*, **21**, 925-930.

Payne, S. W., and M. M. McGarry, 1977: The relationship of satellite inferred convective activity to easterly waves over West Africa and the adjacent ocean during phase III of GATE. *Mon. Wea. Rev.,* **105,** 413–420.

Piersig, W., 1936: Variations of pressure and winds, a treatise on the weather of trade wind region of eastern North Atlantic (in German). *Archiv Deut. Seewarte,* **54** (6). (English translation of Parts 2 and 3, *Bull. Amer. Meteor. Soc.*, **25**, 2–16).

Redelsperger, J-L., D. B. Parsons, and F. Guichard, 2002: Recovery processes and factors limiting cloud-top height following the arrival of a dry intrusion observed during TOGA COARE. *J. Atmos. Sci.*, **59**:2438–2457.

Reed, R. J., D. C. Norquist, and E. E. Recker 1977: The structure and properties of African wave disturbances as observed during phase III of GATE. *Mon. Wea. Rev.,* **105,** 317-333.

Riehl, H., 1945: Waves in the easterlies and the polar front in the tropics. Miscellaneous Rep. 17, Dept. of Meteorology, University of Chicago, 79 pp.

Rooney, D. M., G. S. Janowitz, 1979: Flow over the Rocky and Andes Mountains: Application of an Analytical Model. *J. Atmos. Sci.*, **36**, 549–558.

Shapiro, R., 1970: Smoothing, filtering, and boundary effects. *Rev. Geophys. Space Phys.*, **8**, 359–387.

Shen, B.-W., W.-K. Tao, and M.-L. C. Wu (2010), African easterly waves in 30-day high-resolution global simulations: A case study during the 2006 NAMMA period, *Geophys. Res. Lett.*, **37**, L18803, doi: 10.1029/2010GL044355.

Simmons, A. J., 1977: A note on the instability of the African easterly jet. *J. Atmos. Sci.*, **34,** 1670–1674.

Simpson, R. H., 1974: The hurricane disaster-potential scale. *Weatherwise*, **27,** 169.

Skamarock, W. C., J. B. Klemp, J. Dudhia, D. O. Gill, D. M. Barker, M. Duda, X.-Y. Huang, W. Wang and J. G. Powers, 2008. A Description of the Advanced Research WRF Version 3. NCAR Technical Note, NCAR/TN-475+STR.

Smith, R. B., 1989a: Comments on ‘‘Low Froude number flow past three-dimensional obstacles. Part I: Baroclinically generated lee vortices.’’ *J. Atmos. Sci.*, **46,** 3611–3613.

Tao, W.-K., J. Simpson and M. McCumber, 1989: An ice-water saturation adjustment. *Mon. Wea. Rev*., **117**, 231-235.

Teixeira, M. A. C., and B. Grisogono, 2008: Internal wave drag in stratified flow over mountains on a beta plane. *Quart. J. Roy. Meteor. Soc*., **134**, 11–19.

Thompson, G., R.M., Rasmussen, K.W. Manning, 2004: Explicit forecasts of winter precipitation using an improved bulk microphysics scheme. Part I: Description and sensitivity analysis. *Monthly Weather Review***, 132**, 519-542.

Thorncroft, C. D. and B. J. Hoskins, 1994a: An idealized study of African easterly waves. I: A linear view. *Q. J. R. Meteorol. SOC.*, **120,** 953-982.

Thorncroft, C. D. and B. J. Hoskins, 1994b: An idealized study of African easterly waves. II: A nonlinear view. *Q. J. R. Meteorol. SOC.,* **120,** 983-1015.

Thorncroft, C. D. et al., 2008: Three-Dimensional Structure and Dynamics of African Easterly Waves. Part III: Genesis. *J. of Atmos. Sci.,* **65**, 3596-3607.

Tuleya, R. E. (1994), Tropical storm development and decay: Sensitivity to surface boundary conditions, *Mon. Wea. Rev.,* **122**, 291–304, doi:10.1175/1520-0493(1994)122<0291:TSDADS>2.0.CO;2.

Witchcraft, N. C., Y.-L. Lin, and Y.-H. Kuo, 2005: Dynamics of orographic rain associated with the passage of a tropical cyclone over a mesoscale mountain. *Terr. Atmos. Ocean*, **16**, 1133-1161.

Wu, C.-C.**,** C.-Y. Huang, M.-J. Yang, F.-C. Chien, J.-S. Hong, and T.-H. Yen 2010: Typhoon Morakot (2009) and a special review on the current status and future challenge of tropical cyclone simulation. *Atmos. Sci.,* (in Chinese with an English abstract), **38**, 99-134.

Wu, L., J. Liang, and C.-C. Wu, 2011: Monsoonal Influence on Typhoon Morakot (2009). Part I: Observational Analysis. *J. of Atmos. Sci.*, **68**, 2208-2221.

Xu, X., C. Lu, H. Xu, and L. Chen, 2011: A possible mechanism responsible for exceptional rainfall over Taiwan from Typhoon Morakot. *Atmos. Sci. Let.* **12**: 294–299.

Yang, M.-J., D.-L. Zhang, X.-D. Tang, and Y. Zhang (2011), A modeling study of Typhoon Nari (2001) at landfall:2. Structural changes and terrain-induced asymmetries, *J. Geophys. Res.*, **116**, D09112, doi:10.1029/2010JD015445.

Yen, T. H., C. C. Wu, and G. Y. Lien, 2011: Rainfall simulations of Typhoon Morakot with controlled translation speed based on EnKF data assimilation. *Terr. Atmos. Ocean. Sci.,* **22**, 647-660, doi:10.3319/TAO.2011.07.05.01(TM).

Appendix

I. The derivation of the dispersion relationship

The derivation of the dispersion relationship for linear, hydrostatic, continuously stratified inertia-gravity waves on a β plane is as follows.

$$u_t' + Uu_x' - (f_0 + \beta y)v' + \frac{1}{\rho_0} p_x' = 0 \qquad (1)$$

$$v_t' + Uv_x' + (f_0 + \beta y)u' + \frac{1}{\rho_0} p_y' = 0 \qquad (2)$$

$$\frac{1}{\rho_0} p_z' - g\frac{\theta'}{\theta_0} = 0 \qquad (3)$$

$$u_x' + v_y' + w_z' = 0 \qquad (4)$$

$$\theta_t' + U\theta_x' + \frac{N^2\theta_0}{g} w' = 0 \qquad (5)$$

Let $(u', v', w', p'/\rho_0, \theta') = \mathrm{Re}[\hat{u}(y), \hat{v}(y), \hat{w}(y), \hat{p}(y), \hat{\theta}(y)] \exp[i(kx+ly+mz-\omega t)]$, we have

$$i(kU-\omega)\hat{u} - (f_0+\beta y)\hat{v} + ik\hat{p} = 0 \qquad (6)$$

$$i(kU-\omega)\hat{v} + (f_0+\beta y)\hat{u} + \hat{p}_y = 0 \qquad (7)$$

$$im\hat{p} - g\frac{\hat{\theta}}{\theta_0} = 0 \qquad (8)$$

$$ik\hat{u} + \hat{v}_y + im\hat{w} = 0 \qquad (9)$$

$$i(kU-\omega)\hat{\theta} + \frac{N^2\theta_0}{g}\hat{w} = 0 \qquad (10)$$

$$i(kU-\omega)(8) + \frac{g}{\theta_0}(10): \quad \mathrm{N}^2\hat{w} - m(kU-\omega)\hat{p} = 0 \qquad (11)$$

$$N^2(9) - im(11): \quad ik\,\mathrm{N}^2\hat{u} + N^2\hat{v}_y + im^2(kU-\omega)\hat{p} = 0 \qquad (12)$$

(6): $$\hat{u} = -i\frac{f_0 + \beta y}{kU - \omega}\hat{v} - \frac{k}{kU - \omega}\hat{p} \tag{13}$$

Equation (13) is substituted into (7) and (12):

(7): $$i\frac{(kU-\omega)^2 - (f_0 + \beta y)^2}{kU - \omega}\hat{v} - \frac{k(f_0 + \beta y)}{kU - \omega}\hat{p} + \hat{p}_y = 0 \tag{14}$$

(12): $$i\frac{k^2N^2 - m^2(kU-\omega)^2}{kU - \omega}\hat{p} = \frac{kN^2(f_0 + \beta y)}{kU - \omega}\hat{v} + N^2\hat{v}_y$$

$$\hat{p} = -i\frac{kN^2(f_0 + \beta y)}{k^2N^2 - m^2(kU-\omega)^2}\hat{v} - i\frac{N^2(kU-\omega)}{k^2N^2 - m^2(kU-\omega)^2}\hat{v}_y \tag{15}$$

Equation (15) is substituted into (14):

$$\begin{aligned} &i\frac{(kU-\omega)^2 - (f_0 + \beta y)^2}{kU - \omega}\hat{v} + i\frac{k^2N^2(f_0 + \beta y)^2}{[k^2N^2 - m^2(kU-\omega)^2](kU-\omega)}\hat{v} \\ &+ i\frac{kN^2(f_0 + \beta y)}{k^2N^2 - m^2(kU-\omega)^2}\hat{v}_y - i\frac{kN^2\beta}{k^2N^2 - m^2(kU-\omega)^2}\hat{v} \\ &- i\frac{kN^2(f_0 + \beta y)}{k^2N^2 - m^2(kU-\omega)^2}\hat{v}_y - i\frac{N^2(kU-\omega)}{k^2N^2 - m^2(kU-\omega)^2}\hat{v}_{yy} = 0 \end{aligned}$$

$$\hat{v}_{yy} + \left\{\begin{aligned} &\left[\frac{k\beta}{kU-\omega} - \frac{k^2N^2 - m^2(kU-\omega)^2}{N^2}\right] \\ &-\left[\frac{k^2}{(kU-\omega)^2} - \frac{k^2N^2 - m^2(kU-\omega)^2}{N^2(kU-\omega)^2}\right](f_0 + \beta y)^2 \end{aligned}\right\}\hat{v} = 0$$

Let $\hat{y} = f_0 + \beta y$, $\frac{\partial}{\partial \hat{y}} = \frac{1}{\beta}\frac{\partial}{\partial y}$

$$\hat{v}_{\hat{y}\hat{y}} + \left\{\left[\frac{k}{\beta(kU-\omega)} - \frac{k^2}{\beta^2} + \frac{m^2(kU-\omega)^2}{\beta^2N^2}\right] - \frac{m^2\hat{y}^2}{\beta^2N^2}\right\}\hat{v} = 0$$

b.c. when y approaches infinite, v is close to 0.

When (16) is satisfied, solution is $\hat{v}(\tilde{y}) = v_0 H_n(\tilde{y})\exp(-\tilde{y}^2/2)$,

$\tilde{y} = \left(\frac{m}{\beta N}\right)^{1/2} \hat{y} = \left(\frac{m}{\beta N}\right)^{1/2} (f_0 + \beta y)$, H_n designates nth Hermite polynomials,

$$\left\{\frac{k}{\beta(kU-\omega)} - \frac{k^2}{\beta^2} + \frac{m^2(kU-\omega)^2}{\beta^2 N^2}\right\}\frac{\beta N}{m} = 2n+1, \qquad n = 0,1,2,..... \qquad (16)$$

$$m^2\Omega^3 - [k^2N^2 + (2n+1)m\beta N]\Omega - \beta k N^2 = 0, \qquad \Omega = \omega - kU \qquad (17)$$

The above equation is the dispersion relationship for linear, hydrostatic, inertia-gravity waves on a β-plane.

After rearranging the trigonometric identity, we have equation (18).

$$4\cos^3\theta - 3\cos\theta - \cos 3\theta = 0 \qquad (18)$$

Equation (17) is a specific example of equation (19).

$$\Omega^3 + a\Omega + b = 0 \qquad (19)$$

In case of $\Delta = \frac{b^2}{4} + \frac{a^3}{27} < 0,$ there are three real and unequal roots in (19) (Beyer, 1987).

Let $\Omega = m\cos\theta$ and combine with (18), we have

$$\Omega^3 + a\Omega + b = m^3\cos^3\theta + am\cos\theta + b = 4\cos^3\theta - 3\cos\theta - \cos 3\theta = 0$$

$$\Rightarrow \qquad \frac{4}{m^3} = -\frac{3}{am} = \frac{-\cos 3\theta}{b}.$$

From the above equations, we get $m = 2\left(-\frac{a}{3}\right)^{1/2}$, $\theta = \frac{1}{3}\cos^{-1}\frac{3b}{2a}\left(-\frac{3}{a}\right)^{1/2}$.

Hence, the solutions of equation (19) (Beyer, 1987) are

$$2\left(-\frac{a}{3}\right)^{1/2}\cos\left\{\frac{1}{3}\cos^{-1}\left[\frac{3b}{2a}\left(-\frac{3}{a}\right)^{1/2}\right] - n\frac{2\pi}{3}\right\}, \qquad n = 0,1,2 \qquad (20)$$

Applying the values in the control case A*, equation (17) for n = 0 becomes

$$\Omega^3 - 1.119\times10^{-8}\Omega - 2.36\times10^{-14} = 0. \qquad (21)$$

$$\Delta = \frac{b^2}{4} + \frac{a^3}{27} = -5.176 \times 10^{-26} < 0$$

Thus, there are three real and unequal roots in (21). Using the solutions of (20), we obtained three roots for the intrinsic frequency $\Omega = \omega - kU$: 1.068×10^{-4} s^{-1}, -2.110×10^{-6} s^{-1}, and -1.047×10^{-4} s^{-1}. The intrinsic phase speeds corresponding to these three roots are 10.20 ms^{-1}, -0.2015 ms^{-1}, and -10 ms^{-1}, respectively. Accordingly the wave frequency ω can be solved with the help of uniform basic wind -10 ms^{-1} and wavenumber 1.047×10^{-5} m^{-1} in the control case A*, and are 2.1×10^{-6} s^{-1}, -1.068×10^{-4} s^{-1}, and -2.094×10^{-4} s^{-1}. The associated phase speeds of the roots are obtained with the wave frequency ω divided by the wavenumber in the control case A* 1.047×10^{-5} m^{-1}, and are 0.201 ms^{-1}(eastward propagating gravity wave), -10.20 ms^{-1} (westward propagating mixed Rossby-gravity wave), and -20 ms^{-1} (westward propagating gravity wave), respectively.

For n = 1, equation (17) becomes

$$\Omega^3 - 1.164 \times 10^{-8} \Omega - 2.36 \times 10^{-14} = 0. \qquad (22)$$

$$\Delta = \frac{b^2}{4} + \frac{a^3}{27} = -5.827 \times 10^{-26} < 0$$

Thus, there are three real and unequal roots in (22). The three roots for the intrinsic frequency $\Omega = \omega - kU$ are 1.089×10^{-4} s^{-1}, -2.028×10^{-6} s^{-1}, and -1.069×10^{-4} s^{-1}. Accordingly the wave frequency ω can be solved with the help of uniform basic wind -10 ms^{-1} and wavenumber 1.047×10^{-5} m^{-1} in the control case A*, and are 4.2×10^{-6} s^{-1}, -1.067×10^{-4} s^{-1}, and -2.116×10^{-4} s^{-1}. The intrinsic phase speeds corresponding to these three roots are 10.40 ms^{-1}, -0.1937 ms^{-1}, and -10.21 ms^{-1}, respectively. The associated phase speeds of the roots are obtained with the wave frequency ω divided by the wavenumber in the control case A* 1.047×10^{-5} m^{-1}, and are 0.4011 ms^{-1} (eastward propagating gravity wave), -10.19 ms^{-1} (westward propagating mixed Rossby-gravity wave), and -20.21 ms^{-1} (westward propagating gravity wave), respectively. Because Eqs. (1)-(5)

don’t include the mountain, only part of the roots can be applied in the simulations. Based on the propagating speed estimates, a westward propagating mixed Rossby-gravity wave fits better with the observed AEW and the propagating speed 9.6 ms^{-1} in the idealized simulation.